Improving Barotropic Tide Modeling in MPAS-Ocean and Estimating Changes in Future Tides

by

Kristin Nicole Barton

A dissertation submitted in partial fulfillment
of the requirements for the degree of
Doctor of Philosophy
(Physics and Scientific Computing)
in The University of Michigan
2023

Doctoral Committee:

Professor Brian Arbic, Co-Chair
Professor Vanessa Sih, Co-Chair
Professor Jeremy Bassis
Associate Professor Jordon Horowitz
Research Scientist Mark Petersen, Los Alamos National Laboratory
Associate Professor Marcelle Soares-Santos

Kristin Barton
knbarton@umich.edu

ORCID iD: 0000-0002-6964-2867

To everyone who has encouraged and supported my journey.

ACKNOWLEDGEMENTS

I would like to express my gratitude to everyone who has supported me throughout my PhD journey. First and foremost, I am deeply grateful to my advisor, Professor Brian Arbic. I am thankful for all the opportunities he helped provide and his guidance and patience throughout the process. I am also extremely thankful to Dr. Mark Petersen, who acted as my mentor at Los Alamos National Laboratory. His clear explanations and guides for working on the ocean model were invaluable throughout my time. I am deeply indebted to the members of my dissertation committee, Professor Vanessa Sih, Professor Jeremy Bassis, Professor Marcelle Soares-Santos, and Professor Jordon Horowitz. This dissertation is only possible through their support. I am also incredibly grateful to Dr. Darren Engwirda, Dr. Steven Brus, and Dr. Andrew Roberts for their helpful advice and additional mentorship at LANL. I would also like to acknowledge the PNNL contract DE-AC05-76RL01830, which provided funding, and the NERSC facilities whose HPC systems were used in this research.

I would not have made it to graduate school without help from my wonderful undergraduate advisor, Dr. Hanna Terletska, and my amazing physics friends from MTSU who have provided continued support over the years. I also appreciate the incredible community of students I met in Los Alamos. While our time together was short, you all helped bring much laughter to my time here.

Lastly, I am incredibly thankful for my family, whose love and support have helped me make it this far. Thank you to my mother who has always been there for me no matter what. Thank you to my partner who always pushes me to move forward.

Thank you to my brother and sister, who have helped ensure I spend some time having fun every once in a while. Thank you to my father, grandfather, and grandmother, whose values have made me who I am today. And finally, thank you to my beautiful dog who takes me out for walks and fresh air every day.

TABLE OF CONTENTS

CHAPTER

LIST OF FIGURES

Figure

LIST OF TABLES

Table

LIST OF ABBREVIATIONS

DOE Department of Energy

E3SM Energy Exascale Earth System Model

ISC Ice Shelf Cavities

JSL Jayne and St. Laurent (topographic wave drag scheme)

LGF Local Generation Formula (topographic wave drag scheme)

MPAS Model for Prediction Across Scales

RMSE Root-Mean-Squared Error

SAL Self-Attraction and Loading

SSH Sea Surface Height

SLC Sea Level Change

TWD Topographic Wave Drag

ZAE Zaron and Egbert (topographic wave drag scheme)

ABSTRACT

Modeling the ocean is critical for understanding both present and future risks posed by climate change on coastal communities. Ocean tides in these regions will continue to change over the following decades, yet tides are seldom resolved in climate models; historically, tides have been modeled separately from the oceanic general circulation. This work seeks to improve barotropic tidal modeling in the Department of Energy's Model for Prediction Across Scales, or MPAS-Ocean, and to use the resulting tide capabilities to examine potential future changes to tides. We first describe the implementation of an inline self-attraction and loading Self-Attraction and Loading (SAL) calculation into MPAS-Ocean. When the sea-surface height over a column of ocean moves up and down, this change in mass loading causes small deformations of the Earth's crust. This deformation, along with changes in the gravitational potential of the deformed Earth and ocean, are known as "self-attraction and loading." We implement an inline SAL calculation using the fast spherical-harmonic transform package SHTns and compare the resulting tidal errors to the more common (and computationally cheaper) scalar approximation. We also compare the model's performance on quasi-uniform meshes and a variable-resolution mesh. We examine the root-mean-square error of our modeled tides when compared to a benchmark tidal dataset called TPXO8 and show that the variable resolution mesh and inline SAL calculations reduce the errors. We also find that the computational cost of SAL can be reduced by updating the term as infrequently as 10-15 minutes without sacrificing tidal error. The next improvement to the tidal model is carefully selecting a parameterized topographic wave drag Topographic Wave Drag (TWD). TWD occurs as tides flow over the ocean floor, leading to energy dissipation into the baroclinic tide. This process cannot be resolved directly in our single-layer barotropic model and must be parameterized. We compare three methods of parameterization. Two are scalar methods, based upon papers by Jayne and St. Laurent Jayne and St. Laurent (topographic wave drag scheme) (JSL) and Zaron and Egbert Zaron and Egbert (topographic wave drag scheme) (ZAE); one is a tensor method: Local Generation Formula Local Generation Formula (topographic wave drag scheme) (LGF). The main difference between the first two schemes lies in how the floor roughness is incorporated: JSL uses the standard deviation of topography, while ZAE uses the gradients. The tensor scheme is a simplification of the Nycandar formulation, which has the most thorough physical justification of the three schemes. We find that the most significant improvements in tides came from the ZAE scheme, leading to an improvement of 1.6 cm over the JSL scheme, with LGF landing in the middle. Finally, using the results of this model development, we examine how tides might look in a future climate by running simulations in MPAS-Ocean with sea-level change, ice-shelf cavity geometry, and landfast ice. We adopt regionally varying sea-level and ice shelves from moderate and extreme future scenarios. The sea-level changes exert the most influence in near-shore regions, while the ice shelves have more impact on the global ocean. However, some near-shore areas see more or comparable impact from ice shelves than sea-level rise, indicating the importance of accounting for cavity geometry in future tide simulations.

CHAPTER I

Introduction

The Earth has experienced 1.1^{o}C warming since the pre-industrial age (*Lee et al.*, 2024) with future warming expected to rise above 2.0^{o}C by 2100 (*Raftery et al.*, 2017). The continuing impacts of increased temperatures are felt in many regions, particularly coastal and tropical areas with vulnerable populations. Modern-day climate simulations involve the statistical analysis of results from dozens of climate models run on massive supercomputers. Building models to predict global changes requires combining numerous processes occurring within the Earth System. To this end, climate models typically couple together atmosphere, land, sea ice, and ocean models into what are known as Earth System Models. The results of these models help guide policymakers and the public to implement various adaptations and mitigations to reduce the impact on society and the environment.

The study of how greenhouse gases impact global temperatures can be traced back to Jean-Baptiste Joseph Fourier, well known for his development of the heat equation and Fourier analysis. At the start of his 1827 paper, he asserts that understanding the Earth's temperature distribution is one of the most important subjects in the natural sciences (*Fourier*, 1827). Fourier went on to describe qualitatively how temperatures at the surface of the Earth depend on the energy balance between incoming solar radiation and outgoing infrared radiation. At the time, there was little understanding of the nature of infrared light, referred to as "dark heat" by Fourier, but it was known that the atmosphere was relatively opaque to this form of energy, thus trapping the heat near the surface of the Earth.

The 1800s saw experiments to better understand the absorption of heat by gases, including carbon dioxide. The first known experimental demonstration of the difference in heating of gases containing different amounts of water vapor and carbon dioxide was performed by Eunice Foote (*Foote*, 1856). In her paper, she placed gas and a thermometer inside a container and measured the different temperatures, discovering three primary results. First, warming increases with increased density. Second, warming increases with increased humidity. Finally, warming increases with increased carbonic acid, or CO_2. She further connected this work to climate impacts by suggesting that based on these results, increased carbon dioxide levels could explain warmer climates of past eras of the earth (*Ortiz and Jackson*, 2022). Three years after her discoveries, Tyndall (likely unaware of Foote's work) found similar results (*Tyndall*, 1861). His experimental setup used a heated cube to measure the impact of specifically longwave infrared radiation on gases. It is this longwave radiation which is primarily responsible for the greenhouse effect in the atmosphere.

Svante Arrhenius was the first in 1896 to attempt to calculate, from a simple quantitative model, the temperature change resulting from differing concentrations of CO_2 in the atmosphere (*Arrhenius*, 1896). In his model, he set up an energy budget for a column of the Earth, accounting for incoming light from the sun, outgoing infrared radiation from the Earth, and the absorption and emission of light by gases in the atmosphere. Using best estimates for the time of the absorption coefficients of atmospheric gases, Arrhenius calculated that doubling CO_2 would result in a temperature change of 6^oC. Despite issues in his calculations stemming from the poor data available at the time and the use of a simplified, globally averaged model, he managed to arrive at a value similar to modern estimates of 2.5-4^oC (*Masson-Delmotte et al.*, 2021).

The general viewpoint at the time was that doubling CO_2 would likely take centuries and that some warming would be a pleasant welcome. Thus, the next few decades saw more focus on forecasting weather (short-term fluctations over a few days) than climate (long-term, averaged conditions). Vilhelm Bjerknes was one of the first to suggest that, with enough observational data, the weather could be predicted by numerically integrating the correct equations. His paper laid out a potential atmospheric model comprised of seven equations based on fluid dynamics and thermodynamics (*Bjerknes*, 1904). To circumvent the difficulties of numerically solving these equations, which would have been done by hand at the time, he suggested a graphical method of determining the solutions. Bjerknes continued work on developing graphical calculus methods so that maps of current atmospheric conditions could be used to generate maps of future conditions. While his method was somewhat less accurate, it was still a more appealing forecasting method than tediously solving the equations numerically by hand.

Lewis Fry Richardson, inspired by Bjerknes, decided to pursue the daunting task of numerically integrating the atmospheric equations forward in time to produce a forecast of the weather. In his 1922 book "Weather Prediction by Numerical Process," he detailed the exact method required to predict atmospheric conditions 6 hours into the future on a global grid with 200 km resolution (*Richardson*, 1922). His sample calculation on just a couple of grid cells took six weeks to complete, resulting in a predicted pressure change that was wrong by a factor of roughly one hundred. Despite this failure, he believed better observational data would improve results and imagined a scenario in which real-time forecasts could be done by employing a factory of 64,000 (human) computers. While an incredibly ambitious suggestion for the predigital era, the practical result of his book was to convince meteorologists of the time that numerical weather prediction was utterly infeasible (*Nebeker*, 1995).

While meteorological work continued to develop over the following decades, the topic of numerically solving the atmospheric equations didn't return until after World War II. Efforts during the war led to improvements in technology and the development of computers while cementing the importance of meteorological forecasting and observational data for military interests. The result was a period of rapid progress in the field, helped by John von Neumann, one of the pioneers of modern computing, who identified weather forecasting as a problem particularly suited to solution with computers. He assembled a team to work on this problem, resulting in a successful numerical integration, in 1948, of the simplified quasigeostrophic vorticity equation using the early ENIAC computer (*Charney*, 1948). The door was open now for numerical integration to be practically implemented. The years following saw improvements in computational power, methods, and data collection, leading to increased model complexity, resolution, and accuracy. Additionally, interest began building to study not just the short-term weather but also longer-term climate trends.

While the fundamental equations for weather and climate simulations are the same, there are practical differences in the needs and limitations of the models. Weather simulations are incredibly sensitive to initial conditions, requiring excellent data to predict the exact conditions that will be seen over the course of days. Meanwhile, climate models are not expected to replicate exact future states at specific locations and times. Their accuracy depends more heavily on having the correct statistics about weather and are thus more sensitive to boundary conditions than initial conditions. To better predict long-term outcomes, climate models couple atmospheric models with ocean, land, and sea ice models. This improves the boundary forcing while allowing the other components to simultaneously evolve in time with the atmosphere. For example, the ocean stores and transports both heat and carbon, the land surface contains vegetation, ice, and other elements that impact albedo and carbon, and sea ice impacts albedo and the heat fluxes between the ocean and atmosphere.

A return to the question of climate sensitivity in the atmosphere was made by Syukuro Manabe's energy balance model in 1967 (*Manabe and Wetherald*, 1967), which estimated warming of 2^{o}C with doubled CO_2. The revolution in computational technology, combined with much more complete data on the absorption spectra of gases, meant it was now possible to fix several issues found in the energy budget analysis of Arrhenius, thus marking the first realistic and sound estimate of climate sensitivity. The model used up-to-date data on the absorption spectra of atmospheric gases but was still a globally averaged model that did not show how these temperature changes would vary spatially across the globe. The need to understand regional variations in climate, along with the help of computational improvements made in the domain of weather forecasting, resulted in the first fully three-dimensional atmospheric general circulation model (*Smagorinsky et al.*, 1965). Alongside this development, Kirk Bryan worked on an ocean general circulation model that could run alongside the atmospheric model, providing the necessary boundary forcing (*Bryan*, 1969b; *Manabe and Bryan*, 1969).

Recent decades have seen continued increases in the quality of observational data, model resolution, and computational power, resulting in more accurate and complex models. To account for model biases, simulations are performed using many different models following pre-determined emission scenarios. However, limitations in computational abilities, as well as historical precedent, still lead to many simplifications in the ocean component of climate models. For instance, ocean general circulation models used in climate studies generally do not explicitly represent tides. Instead, when they pay attention to tides at all, they often rely on pre-calculated maps of tidal amplitudes and phases. Part of the difficulty in representing tides is the difference in time scales between tides and climate. Most climate models perform decade-to-century simulations, while tides occur on daily time scales. However, tides can change along with climate. Many recent studies show how and why tides are changing, with near-term causes mainly due to changes in geometry around coastlines and ice shelf cavities (*Haigh et al.*, 2020). The largest changes in tides tend to occur around coastlines, where tides themselves are the largest. Already, there is observational data of statistically significant trends in tidal levels, sometimes of a similar order in magnitude to sea-level rise itself (*Mawdsley et al.*, 2015). Near the shore, changes in high tides can compound with storm surges and sea level rise to exacerbate coastal flooding. Understanding these interactions can help in predicting future tidal changes and the resulting implications for coastal communities. Tides also interact with other components of the Earth System, such as sea ice, ice shelves, and estuaries. For these reasons, there has been a recent push to find ways to include or improve tidal representation in global climate models.

The following work discusses efforts to implement and improve tides within the Department of Energy's Model for Prediction Across Scales Model for Prediction Across Scales (MPAS) ocean model. Chapter 2 will describe the equations necessary for ocean and tide modeling and some of the assumptions and simplifications commonly used in modern ocean models. Chapter 3 consists of a published paper on adding "inline" self-attraction and loading to the tidal calculations in the MPAS-Ocean model, where the terms "inline" and "self-attraction and loading" will be explained in that chapter. Chapter 3 includes an evaluation of the improvement in tidal errors with inline self-attraction and loading and contains an analysis of the computational costs involved. Chapter 4 presents a test of multiple parametrizations of topographic wave drag, and the further reductions in tidal errors accomplished with these parameterizations. With tides now adequately included in the model, Chapter 5 examines how those tides may change with future climate, through simulations of tides under different states of sea-level rise and ice melt. The work concludes with a summary in Chapter 6.

CHAPTER II

Ocean and Tide Modeling

2.1 Ocean Primitive Equations

The governing equations for ocean models are typically variations of the *primitive equations*, first described by Vilhelm Bjerknes (*Bjerknes*, 1904). These consist of two-dimensional horizontal momentum equations, a mass conservation equation, a thermodynamical equation of state, a hydrostatic equation, and advection-diffusion equations describing the evolution of tracers in the ocean (e.g., salinity and temperature). In the work presented here, the model is run in *barotropic* mode, which assumes that the ocean has a single layer of homogeneous density. In planned future work, our collaborators will build upon our work here with simulations of tides in the stratified ocean environment.

2.1.1 The Lagrangian Derivative

The Lagrangian (or material) derivative is a critical tool for continuum dynamics and can be explained in terms of its contrast with the more traditional Eulerian derivative. For the Eulerian time derivative d/dt, the focus is on how a given field changes in time at a fixed position in space. The Lagrangian derivative, D/Dt instead focuses on how the field changes from the perspective of a mass parcel that travels through the field. We can write out the definition for the Lagrangian derivative as follows. For some field, θ, we can express the changes in both space and time of the field.

$$\delta\theta = \frac{\partial\theta}{\partial t}\delta t + \frac{\partial\theta}{\partial x}\delta x + \frac{\partial\theta}{\partial y}\delta y + \frac{\partial\theta}{\partial z}\delta z \tag{2.1}$$

For velocity field $\vec{v} = (\frac{\partial x}{\partial t}, \frac{\partial y}{\partial t}, \frac{\partial z}{\partial t})$ the total Lagrangian derivative can be expressed as follows.

$$\frac{D\phi}{Dt} = \frac{\partial\theta}{\partial t} + \frac{\partial\theta}{\partial x}\frac{\partial x}{\partial t} + \frac{\partial\theta}{\partial y}\frac{\partial y}{\partial t} + \frac{\partial\theta}{\partial z}\frac{\partial x}{\partial t} = \frac{\partial\theta}{\partial t} + \vec{v}\cdot\nabla\theta \tag{2.2}$$

2.1.2 Momentum Equation in a Rotating Frame

A force acting on a fluid parcel will cause it to advect. For a parcel of density ρ and volume V, a force per unit volume F, then

$$\int\limits_V F dV = \frac{D}{Dt}\int\limits_V \rho\vec{u} dV. \tag{2.3}$$

Since the Lagrangian derivative on a volume can be expressed as $D_t \int \rho\vec{u}dV = \int \rho D_t\vec{u}dV$ (e.g., *Vallis* (2017)), then we can rewrite the advection term as the following.

$$\frac{1}{\rho}\vec{F} = \frac{D\vec{u}}{Dt} \tag{2.4}$$

Fluids experience pressure, p as a force acting inwardly on the surface, S, of the parcel. Expressing this as a force due to pressure and using the divergence theorem, we can find the following equation.

$$\vec{F}_p = \int\limits_v \vec{f}_p dV = -\int\limits_S p dV = -\int\limits_V \nabla p dV \tag{2.5}$$

Next, we can consider the impact of the Earth's rotation on the form of the momentum equation. Acceleration in a rotating frame (R) can be related to acceleration in an inertial frame (I) in terms of position $(\vec{r})$ and the angular velocity of the rotating frame ($\vec{\Omega}$)

$$\left.\frac{d}{dt}\right|_R u_R = \left.\frac{d}{dt}\right|_I u_I - 2\vec{\Omega} \times \vec{v}_R - \vec{\Omega} \times (\vec{\Omega} \times \vec{r}) \tag{2.6}$$

The centrifugal term, $-\vec{\Omega} \times (\vec{\Omega} \times \vec{r})$, is incorporated into an “effective gravity” and is often not discussed further; see *Durran* (1993) for a notable exception. However, the Coriolis term, $-\vec{\Omega} \times \vec{v}_R$, must be included in the momentum equation.

Additional forces can be included as needed, such as diffusive and friction terms. We can express these as $\vec{\mathcal{F}}$, resulting in the following momentum equation.

$$\frac{D\vec{u}}{Dt} + 2\vec{\Omega} \times \vec{u} = -\frac{1}{\rho}\nabla p + \vec{\mathcal{F}} \tag{2.7}$$

2.1.3 Hydrostatic Balance

The hydrostatic balance is a simplification often made to reduce the number of variables in the model by reducing the momentum equation from a 3-dimensional equation to a horizontal 2-dimensional equation within a single layer. A typical ocean model can feature multiple vertical layers described by the 2D equations to account for stratified layers within the ocean. The approximation assumes that in the vertical direction, the gravity is exactly balanced by the pressure gradient:

$$\frac{\partial p}{\partial z} = -\rho g \tag{2.8}$$

Here, p is the pressure, g is gravitational acceleration, ρ is density, and z is the vertical coordinate. The assumption behind this approximation is that accelerations in the vertical component, Dw/Dt, are negligible compared to gravity and pressure.

2.1.4 Mass Continuity

To derive the mass conservation equation, we can consider a volume V in which fluid can flow in and out. The amount of fluid passing through the surface S must balance the rate of mass change of the volume.

$$\int\limits_V \frac{\partial \rho}{\partial t} dV = \int\limits_S (\rho\vec{u}) \cdot d\vec{S} = \int\limits_V \nabla \cdot (\rho\vec{u}) dV \tag{2.9}$$

With the help of the divergence theorem in the last step, we can equate the terms inside the first and last integrals to get the continuity equation. Often, we can assume that the fluid is incompressible. This further simplifies the equation since the density will not change, thus $D\rho/Dt = 0$, and only the divergence of velocity remains.

$$\vec{\nabla} \cdot \vec{u} = 0 \tag{2.10}$$

This change turns the mass conserving term into a volume conserving term. While this is a decent approximation for most ocean modeling, it does have two important implications. First, an incompressible fluid does not transmit sound waves, which could be important for ocean applications such as sonar waves. Second, it does not allow for "steric" sea-level rise which occurs as ocean density changes with temperature.

2.1.5 Tracers and Thermodynamic Equation

Tracer equations describe the transport of tracers, which consist of either thermodynamic properties or substances that are conserved during advection and can be used to trace the flow of fluid. For ocean climate modeling, the two main tracers are potential temperature and salinity. Since these are also conservation equations, they are similar to the mass continuity equation, but with the addition that tracers can experience diffusion ($\mathcal{D}$) and external forcing ($\mathcal{F}$). The governing equation for a tracer φ is:

$$\frac{\partial \varphi}{\partial t} + \nabla(\varphi\vec{v}) = \mathcal{D} + \mathcal{F} \tag{2.11}$$

Along with the tracer equations we must have an equation of state relating the density, pressure, potential temperature (Θ), and salinity (S):

$$\rho = \rho(\Theta, S, p), \tag{2.12}$$

where potential temperature is a variable that has removed the effects of compressible heating. There are a number of versions of this equation of state which are generally determined through empirical data. A very simple example of an equation of state is the following linear equation:

$$\rho(\Theta, S, p) = \rho_0\big(1 - \alpha(\Theta - \Theta_0) + \beta(S - S_0) + \gamma(p - p_0)\big). \tag{2.13}$$

In this example, we can see how density will increase with increasing salinity and pressure while decreasing with increased potential temperature.

2.2 Tidal Equations

2.2.1 Tidal Forcing

Tidal forcing results from the action of gravity from the Moon (and Sun) across the finite size of the Earth. To derive the tidal equations used in simulating tides, we can start with the gravitational potential, Φ, at a point P relative to the Moon.

$$\Phi = -\frac{Gm_m}{R_p}. \tag{2.14}$$

Here, G is the gravitational constant, m_m is the mass of the moon, and R_p is the distance from the center of the moon to a location P on the surface of the Earth. For a lunar angle φ, distance from center of moon to the center of the Earth R_m, and

Earth radius R_e, then we can rewrite the distance to point P:

$$\Phi = -\frac{Gm_m}{\sqrt{R_e^2 + R_m^2 - 2R_eR_m\cos\varphi}} \tag{2.15}$$

Since $R_e \ll R_m$, this can be expressed in terms of Legendre polynomials.

$$\Phi = -\frac{Gm_m}{R_m}\sum_{n=0}^{\infty}\left(\frac{R_e}{R_m}\right)^n P_n(\cos\varphi) \tag{2.16}$$

Consider the first few Legendre polynomials.

$$P_0(\cos\varphi) = 1 \tag{2.17}$$

$$P_1(\cos\varphi) = \cos\varphi \tag{2.18}$$

$$P_2(\cos\varphi) = \frac{1}{2}\left(3\cos^2\varphi - 1\right) \tag{2.19}$$

The tidal forces can be found as the gradient of the polynomials. For $n = 0$, the value is constant and so there is no force. The force from the $n = 1$ term is uniform along the direction pointing from the center of the Earth to the center of the moon. The tidal forcing is produced by the $n = 3$ term, with higher-level terms typically neglected due to their small value. The tidal potential can be written as the following.

$$\Phi_t = -\frac{Gm_mR_e^2}{2R_m^3}\left(3\cos^2\varphi - 1\right) \tag{2.20}$$

2.2.2 Equilibrium Tide

We can express the tidal potential in terms of the equilibrium tide, or the height the sea-surface would attain if it were able to reach equilibrium. First, we can express the lunar angle in terms of the latitude at the point P, ϕ, the declination of the moon, d, and the difference in longitudes between P and the point directly underneath the moon, λ. The relationship between these values is

$$\cos\varphi = \sin\phi\sin d + \cos\phi\cos d\cos\lambda. \tag{2.21}$$

Using the new variables along with the substitution $g = \frac{Gm_e}{R_e^2}$ for a mass on Earth, we can rewrite the tidal potential.

$$\begin{aligned}\Phi_t &= -\tfrac{m_m g R_e^4}{m_e R_m^3}\Big[\tfrac{3}{4}\cos^2 d\cos^2\phi\cos 2\lambda + \tfrac{3}{4}\sin 2d\sin 2\phi\cos\lambda \qquad (2.22)\\ &+ \big(\tfrac{3}{2}\sin^2 d - \tfrac{1}{2}\big)\big(\tfrac{3}{2}\sin^2\phi - \tfrac{1}{2}\big)\Big]. \qquad (2.23)\end{aligned}$$

Both the declination of the moon (d), and the longitude difference between the moon and the point P (λ) change over time, while the latitude of the point is fixed. We can express the potential in terms of these time-dependent components:

$$\Phi_t = A_2\cos^2 d\cos 2\lambda + A_1\sin 2d\cos\lambda + A_0\big(\frac{3}{2}\sin^2 d - \frac{1}{2}\big). \tag{2.24}$$

The first term corresponds to semi-diurnal, or twice-daily tides; the second term is the diurnal, or once-daily tides; the final term represents long-period tides that vary slowly with the moon's declination (*Pugh and Woodworth*, 2014).

2.2.3 Tidal Details

To use the equations above in a tidal or ocean model, each constituent, or harmonic component, of the tides must be included explicitly. For each of the species described (semi-diurnal, diurnal, long-period), there are multiple constituents (of both lunar and solar origin) with different amplitudes and slightly different periods. The largest of these is the M_2, or twice-daily lunar tide. The amplitude of the solar tide, S_2 is about half that of the lunar tide. There are also once daily tides (K_1, O_1), and long-term constituents (M_m, M_f).

The solar and lunar tides work together to create month-long cycles in tides known as the *spring-neap* cycle. When the Moon, Sun and Earth are aligned (spring tide), the lunar and solar tides add constructively to create the larger spring tidal ranges, where tidal range denotes the difference between high and low tidal elevations. When the Moon, Sun, and Earth are not aligned (neap tide), the tidal range is at a minimum.

CHAPTER III

Global Barotropic Tide Modeling Using Inline Self-Attraction and Loading in MPAS-Ocean

This chapter is published in its entirety as:

Barton, K. N., Pal, N., Brus, S. R., Petersen, M. P., Arbic, B. K., Engwirda, D., Roberts, A. F., Westerink, J., Wirasaet, D., Schindelegger, M., (2022), Global barotropic tide modeling using inline self- attraction and loading in MPAS-ocean, *Journal of Advances in Modeling Earth Systems*, 14 (11), e2022MS003,207.

3.1 Introduction

Tides are an integral and dynamic component of the Earth system. According to the IPCC Special Report for Oceans and Cryosphere in a Changing Climate, "it is *very likely* that the majority of coastal regions will experience statistically significant changes in tidal amplitudes over the course of the 21st century" (*Bindoff et al.*, 2019). Additionally, the report concluded with "*high confidence*" that tides are one of several local processes essential to predicting future extreme sea level events (*Oppenheimer et al.*, 2019a). Coastal tide gauge records point to changes in tidal amplitudes by as much as 1–2% per decade (*Flick et al.*, 2003; *Ray*, 2006; *Müller et al.*, 2011). In some locations, the secular changes in tidal amplitudes are of comparable magnitude to changes in mean sea level (*Jay*, 2009). There are a number of processes that affect observed tides in a particular region, from long-term Earth system processes (such as tectonic motion) to shorter-term processes which could have impacts over the next century (*Haigh et al.*, 2020). For example, mean sea-level rise, shoreline position, or the depth of estuaries can influence the geometry of the local region such that tidal resonance is altered and amphidromic points shift spatially. Meanwhile, seabed roughness, river flow, sea ice coverage, or ocean stratification, can lead to changes in the frictional dissipation and energy exchange of the tides (*Haigh et al.*, 2020). These non-astronomical effects are the reason for efforts now to include changes in tides as a factor in assessing flood risks in a changing climate (*Jay*, 2009; *Haigh et al.*, 2020). In order to model and predict tidal changes and their impacts in a changing climate, it is desirable to simulate tides within an Earth system model.

Historically, tide modeling and climate modeling have been performed separately. In relatively recent efforts, the two types of modeling have been performed concurrently (*Arbic et al.*, 2018). Tide gauges have been used for centuries to determine tidal amplitudes and phases at specific locations, but as computational methods became more feasible, work began on developing tide models that would allow tidal amplitude and phases to be estimated at any point in the ocean (*Pekeris and Accad*, 1969). The resolution and accuracy of these early barotropic tide models increased throughout the late 20th century with the help of increased computational power and assimilation from satellite altimeter data (*Hendershott*, 1972; *Schwiderski*, 1979; *Parke and Hendershott*, 1980; *Ray*, 1993; *Le Provost et al.*, 1994; *Shum et al.*, 1997; *Dushaw et al.*, 1997). Conversely, baroclinic climate models have historically excluded explicit tide calculations due to computational constraints and the use of large time steps for long-term simulations. Early 3-D ocean models used a “rigid-lid” assumption to remove barotropic gravity waves, thus not permitting tides at all (*Bryan*, 1969a; *Griffies et al.*, 2000). The first studies to include tides in a baroclinic model were performed at regional scales (*Cummins and Oey*, 1997; *Kang et al.*, 2000; *Merrifield et al.*, 2001). The first global simulations of baroclinic tides (*Arbic et al.*, 2004; *Simmons et al.*, 2004) included only tidal forcing. Over the past decade, several ocean general circulation models have begun incorporating tides (*Arbic et al.*, 2010; *Müller et al.*, 2012; *Waterhouse et al.*, 2014; *Rocha et al.*, 2016; *Arbic et al.*, 2018), allowing for investigations into interactions of barotropic and internal tides with mesoscale eddies and other components of the Earth system.

Several factors must be examined and accounted for in global tide models, including self-attraction and loading SAL, model resolution, the underlying bathymetric dataset, and parameterized topographic wave drag. SAL accounts for a combination of effects: the deformation of the Earth's crust due to mass loading and the self-gravitation of the load-deformed Earth as well as of the ocean tide itself (*Hendershott*, 1972). Self-attraction and loading can change tidal amplitudes to first-order, up to 20% in some regions, and also significantly impacts tidal phases and amphidromic points (*Gordeev et al.*, 1977). Full calculation of SAL calls for convolution of tidal elevation with a proper Green's function or a multiplication with load Love numbers in the spectral—i.e., spherical harmonic—domain (*Ray*, 1998). Early attempts to calculate SAL using spherical harmonics proved expensive (*Stepanov and Hughes*, 2004), so ocean tide models have often employed cheaper methods, such as a scalar approximation (in which the SAL is approximated locally by a constant factor multiplied by the tidal elevation), an iterative method, or the use of SAL fields drawn from other sources. The scalar approximation fails to preserve the scale-dependent, spatially smoothing behavior of the SAL and can be particularly unreliable in shelf areas where tidal length scales are much smaller than in the open ocean (*Ray*, 1998). The iterative method is tedious to employ and relies on intermediate harmonic analysis, meaning that non-periodic self-attraction and loading effects, such as those associated with storm surges, cannot be easily accounted for. Reading in a dataset for SAL can improve the accuracy of modeled tides in the present-day, but is not appropriate for the prediction of tides in a future world where tides and other climate system components will be different. Motivated by these points and by recent works incorporating SAL in various hydrodynamic frameworks (*Schindelegger et al.*, 2018; *Shihora et al.*, 2022; *Vinogradova et al.*, 2015), we choose to implement a full inline calculation of SAL for tides. The model we use is the oceanic component of the Department of Energy Department of Energy (DOE) Energy Exascale Earth System Model Energy Exascale Earth System Model (E3SM) — namely, the ocean Model for Prediction Across Scales (MPAS-Ocean).

This paper represents a first step toward embedding tides within MPAS-Ocean. We evaluate MPAS-Ocean as a barotropic tide model in preparation for including tides in full baroclinic simulations. We demonstrate the feasibility of implementing a full inline calculation of SAL using the barotropic configuration. Furthermore, we compare tidal sensitivity to different bathymetric products, different resolutions, and parameterized topographic wave drag. Sensitivity to bathymetry in tidal simulations has been demonstrated previously and can be improved with high-quality regional patching (*Lyard et al.*, 2021; *Blakely et al.*, 2022). Convergence of tidal errors with increasing model grid resolution has been explored in, e.g., *Egbert et al.* (2004), *Arbic et al.* (2008) and *Pringle et al.* (2021a). A parameterized topographic wave drag accounts for the energy dissipation that occurs when internal tides are generated from the tidal flow over rough topography in the presence of stratification. The importance of including this term in barotropic tidal simulations has been discussed in many papers (*Jayne and St. Laurent*, 2001; *Arbic et al.*, 2004, 2008; *Egbert et al.*, 2004; *Blakely et al.*, 2022). Finally, we expect the inclusion of a full SAL calculation to increase the computational time of the simulations, as has been shown in previous implementations *Schindelegger et al.* (2018), *Shihora et al.* (2022). We end with an examination of the computational cost incurred by our SAL calculation and compare performance on the various resolution meshes used in the study.

3.2 Methods and Implementation

3.2.1 Model Description

The Model for Prediction Across Scales, or MPAS, integrates a variety of geophysical fluid dynamics models on unstructured meshes (*Ringler et al.*, 2013; *Petersen et al.*, 2019; *Golaz et al.*, 2019). MPAS contains various dynamical cores, each of which contains a specific implementation of a physical system (e.g. atmosphere, sea ice, etc.). We implement tides in the ocean core, MPAS-Ocean. The model is based on unstructured, Voronoi-type tessellations supporting variable resolution, allowing for a range of spatial length scales to be captured in a single simulation. A variable resolution unstructured mesh allows for a detailed representation of some regions (e.g., coastlines) while reducing overall computational cost through the use of lower resolutions in regions with larger length scales.

For the purpose of evaluating tides in MPAS-Ocean, we have modified the model to run in a two-dimensional (2-D) barotropic mode. The governing equations include a momentum equation in a vector-invariant form and a layer thickness equation,

$$\begin{aligned} \frac{\partial \mathbf{u}}{\partial t} + \left(\nabla \times \mathbf{u} + f\mathbf{k}\right) \times \mathbf{u} &= -\nabla K - g\nabla\left(\eta - \eta_{EQ} - \eta_{SAL}\right) \qquad (3.1) \\ & \quad -\chi \frac{\mathcal{C}\mathbf{u}}{H} - \frac{\mathcal{C}_D |\mathbf{u}|\mathbf{u}}{H}, \\ \frac{\partial h}{\partial t} + \nabla \cdot (h\mathbf{u}) &= 0, \qquad (3.2) \end{aligned}$$

where $\mathbf{u}$ represents the depth-averaged horizontal velocity, t is the time coordinate, f is the Coriolis parameter, $\mathbf{k}$ is the vertical unit vector, $K = |\mathbf{u}|^2/2$ is the kinetic energy, g is the gravitational acceleration constant, η is the sea-surface height Sea Surface Height (SSH) relative to the moving bed, η_{EQ} is the equilibrium tide, η_{SAL} is the perturbation of tidal elevations due to SAL, χ is a tunable scalar dimensionless wave drag coefficient, $\frac{\mathcal{C}}{h}$ is a topographic wave drag time scale, H is the resting depth of the ocean, and h is the total ocean thickness such that $H + \eta = h$. The full form of the drag terms in (3.2) would use the total thickness h, but our implementation uses the linearized version with the resting depth H. In addition, $\frac{H}{\mathcal{C}}$ is read in from the variable `rinv` from the HyCOM file `jsl_lim24_inv_hrs.nc`, where the original calculation is described in *Buijsman et al.* (2016). $\mathcal{C}_D$ is a log-law based drag model, evaluated according to eq. 3.3 where $\kappa = 0.4$ is the von Karman constant (*Von Kármán*, 1931), $z_0 = 0.001$ is the roughness parameter and H is the ocean resting thickness. The minimum and maximum functions constrain C_D to the range $[0.0025, 0.1]$.

$$C_D = \max\left[0.0025, \min\left[0.1, \left(\frac{\kappa}{\ln\left(\frac{H}{2z_0}\right)}\right)^2\right]\right] \tag{3.3}$$

MPAS-Ocean retains the capability to be run with multiple layers with tides and SAL for future investigations, but only the single-layer barotropic model is used in this study. The multi-layer baroclinic model would additionally include three-dimensional tracer equations for temperature and salinity, vertical advection and diffusion terms on all equations, and the computation of density from the equation of state for seawater and pressure at each layer from the hydrostatic equation.

Tidal forcing is implemented by adding a SSH perturbation, η_{EQ}, into the pressure gradient operator.

$$\eta_{EQsd,c} = A_c f_c(t_{ref}) L \cos^2(\phi) \cos\left[\omega_c(t - t_{ref}) + \chi_c(t_{ref}) + \nu_c(t_{ref}) + 2\lambda\right] \tag{3.4}$$

$$\eta_{EQd,c} = A_c f_c(t_{ref}) L \sin(2\phi) \cos\left[\omega_c(t - t_{ref}) + \chi_c(t_{ref}) + \nu_c(t_{ref}) + \lambda\right], \tag{3.5}$$

These terms are valid for semidiurnal (sd) and diurnal (d) tidal constituents (*Arbic et al.*, 2018). The total forcing comes from summing over each of the constituents,

c. Here A and ω are the forcing amplitude and frequency, respectively, dependent on the tidal constituent, t_{ref} is a specified reference time, t is time, ϕ is latitude, λ is longitude, $\chi(t_{ref})$ is an astronomical argument accounting for the constituent's phase due to astronomical positions of the Moon and/or Sun, and $f(t_{ref})$ and $\nu(t_{ref})$ are amplitude and phase nodal factors accounting for small known astronomical modulations in the tidal forcing. $L = 1 + k_2 - h_2$ is a combination of body tide Love numbers that account for changes in the gravitational potential (k_2) due to deformation of the Earth's crust and mantle from tidal forcing (h_2).

3.2.2 Self-Attraction and Loading

SAL is implemented as additional body force via the SSH gradient term in Eq. (3.2). We express the inline SAL for tides in terms of the spherical harmonic decomposition of the SSH (*Hendershott*, 1972)

$$\eta_{SAL} = \sum_n \frac{3\rho_0}{\rho_{earth}(2n+1)}(1 + k_n' - h_n')\eta_n. \tag{3.6}$$

where each spherical harmonic SSH term η_n is multiplied by a scalar coefficient. Here $\rho_0 = 1035\frac{kg}{m^3}$ is the average density of seawater, $\rho_{earth} = 5517\frac{kg}{m^3}$ is the average density of the solid Earth, and the multiplicative term $(1 + k_n' - h_n')$ represents load Love numbers (obtained from *Wang et al.* (2012)) corresponding to physical effects of SAL. The "1", k_n', and h_n' terms account for gravitational self-attraction of the ocean, gravitational self-attraction of the deformed solid Earth, and deformation due to loading of the solid Earth respectively. However, the usage of SSH for calculating SAL is only appropriate for tides and wind-driven barotropic motions. For other motions one must use bottom pressure anomalies.

Before this work, SAL was implemented in MPAS-Ocean via the scalar approxi-

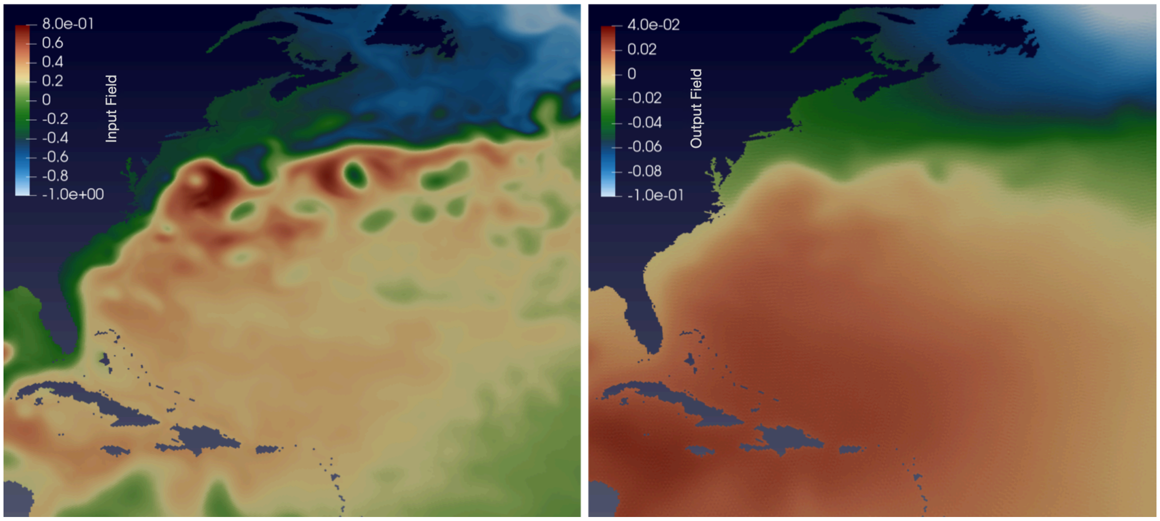

Figure 3.1: Example of spatially-smoothed output (right) of the SAL operator (eqn. 3.6) applied to an input field (left). The SAL output has amplitude roughly 1/10 that of the original. For the barotropic runs used in this model, we evaluate SAL using the SSH signal, shown here. However, for a full baroclinic model it is necessary to use the bottom pressure as input.

mation (*Accad and Pekeris*, 1978; *Ray*, 1998)

$$\eta_{SAL} = \beta\eta, \tag{3.7}$$

where η is the SSH prior to alterations, and $\beta = 0.09$ is a scalar parameter used to approximate the influence of SAL. This approximation is a computationally inexpensive method that is sufficiently accurate for many cases. However, it does not capture the spatial dependence and large-scale smoothing of the full calculation (Fig. 3.1).

We evaluate Eq. (3.6) using the fast spherical harmonics transform package, SHTns (*Schaeffer*, 2013). This package can only be run on a single node with shared memory, not across nodes with a message passing interface (MPI). In contrast, MPAS-Ocean typically runs on hundreds of nodes using MPI. Further, the input data must be arranged on a Gaussian grid, because SHTns takes advantage of the geometry of this grid (i.e., the latitudes are arranged at zeros of Legendre polynomials) to perform faster transforms. To use SHTns within MPAS-Ocean, we first gather the distributed

SSH field to a single head node before remapping the data onto the Gaussian grid. The remapped data can then be transformed into spherical harmonics, where η_{SAL} is easily calculated by multiplying the harmonic coefficients by the known load Love numbers. Finally, the process is performed in reverse as η_{SAL} is transformed into a spatial field on the Gaussian grid, remapped onto the MPAS mesh, and sent back out to the nodes (Fig. 3.2). For each of the quasi-uniform meshes, the Gaussian grid resolution was chosen to match the mesh resolution at the equator. For the variable resolution mesh, the Gaussian grid resolution is equal to the minimum resolution of the mesh, or 5 km. The spherical harmonic order cutoff is determined by the number of latitudes in the Gaussian grid according to Eqs. 3.8, where l_{max} is the maximum degree, m_{max} is the maximum order, and $nlat$ is the number of latitudes in the Gaussian grid.

$$\begin{aligned} l_{max} &= \text{integer}\left(\tfrac{nlat}{2}\right) - 1 \\ m_{max} &= l_{max} \end{aligned} \tag{3.8}$$

Prior to our global tidal simulations, we validated the above approach by initializing the SSH to a single spherical harmonic function on the MPAS mesh, allowing us to easily confirm that the results matched the theoretical expectation.

3.2.3 Meshes

Several studies have demonstrated the effect of resolution on the accuracy of tidal models (*Egbert et al.*, 2004; *Arbic et al.*, 2008; *Pringle et al.*, 2021a). Here, we compare two types of meshes: icosahedral and variable resolution. Icosahedral meshes are spatially quasi-uniform, and have the smallest variations of cell area, vertex angles, and edge lengths across the sphere among any global meshes, so are the perfect choice for comparisons between resolutions. Table 3.1 shows the resolutions of the

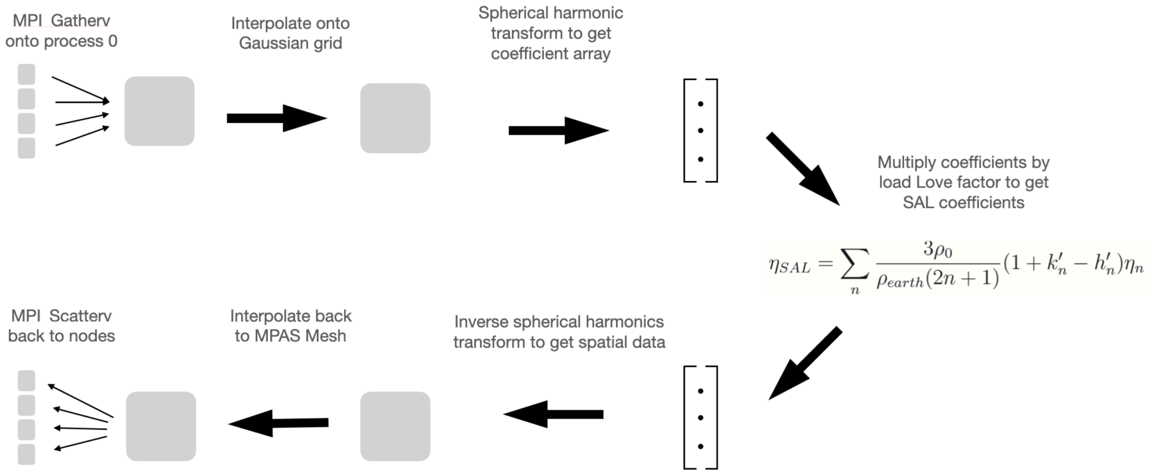

Figure 3.2: Overview of the procedure used to calculate SAL. The SSH field is sent to process 0, remapped onto a Gaussian grid, then decomposed into spherical harmonics. The perturbation in SSH due to SAL is calculated and then transformed into spatial data, remapped onto the MPAS-Ocean mesh, and sent back to the nodes.

icosahedral meshes used in our simulations. The numbers 7–10 refer to the number of refinement iterations in the mesh generation process, where each iteration divides every triangle on the primal (triangular) mesh into four triangles, so that the mesh at step n contains $2+10\cdot 4^n$ cells on the dual mesh (12 pentagons and the rest hexagons).

The variable resolution 45 to 5-km mesh (Fig. 3.3 and 3.4) is an ADCIRC (Advanced CIRCulation)-style mesh (*Pringle et al.*, 2021a). Tides are particularly sensitive to shallow coastal areas and steep topographic gradients, where significant tidal energy dissipation takes place. In fact, about 2/3 of tidal dissipation occurs in coastal regions (*Egbert and Ray*, 2000, 2003). In our variable-resolution configuration, we adapt the length scale of the mesh in critical areas to better capture dynamics in shallow tidal flats and in regions of sharp bathymetric variation; employing the following mesh spacing heuristics to design a global mesh that captures local tidal processes:

$$l_{wav}(\mathbf{x}) = \beta_{wav} T_{M_2} \sqrt{g\tilde{H}}\,, \tag{3.9}$$

$$l_{slp}(\mathbf{x}) = \beta_{slp} \frac{2\pi\tilde{H}}{\tilde{\nabla H}}\,, \tag{3.10}$$

$$l^*(\mathbf{x}) = \max\left(\min\left(l_{wav}(\mathbf{x}), l_{slp}(\mathbf{x}), l_{max}\right), l_{min}\right)\,, \tag{3.11}$$

$$l^* \rightarrow |\nabla l| \leq \gamma\,. \tag{3.12}$$

Here, $l_{wav}(\mathbf{x})$ and $l_{slp}(\mathbf{x})$ are barotropic tidal length-scale heuristics, with l_{wav} increasing mesh resolution in shallow regions to resolve the wavelength of shallow-water dynamics, and l_{slp} increasing mesh resolution in areas of large relative bathymetric gradients to capture topographically-induced flow. β_{wav} and β_{slp} are tunable 'resolution-selection' parameters, set to $\beta_{wav} = \frac{1}{80}$ and $\beta_{slp} = \frac{1}{4}$ in this study. To produce smooth distributions suitable for mesh generation, $\tilde{H}$ and $\tilde{\nabla H}$ represent Gaussian-filtered ($\sigma = \frac{1}{2}$) depths and gradients obtained from the raw GEBCO2021 bathymetry. $l^*(\mathbf{x})$ is an initial combined estimate of mesh spacing throughout the domain, taking limiting values of l_{wav}, l_{slp} at each spatial point and clipping to $l_{min} = 5km$ and $l_{max} = 45km$. To control the gradation of the mesh overall, this initial estimate is 'gradient-limited' to ensure the relative increase in mesh spacing is bounded below a user-defined threshold, here set to $\gamma = \frac{1}{8}$. See Figure 3.3 for a detailed view of the resulting mesh spacing pattern $l(\mathbf{x})$ in the North Atlantic region. Meshes in this study are generated using the `JIGSAW` unstructured meshing library (*Engwirda*, 2017), with pre-processing completed using the `scikit-image` package (*Van der Walt et al.*, 2014).

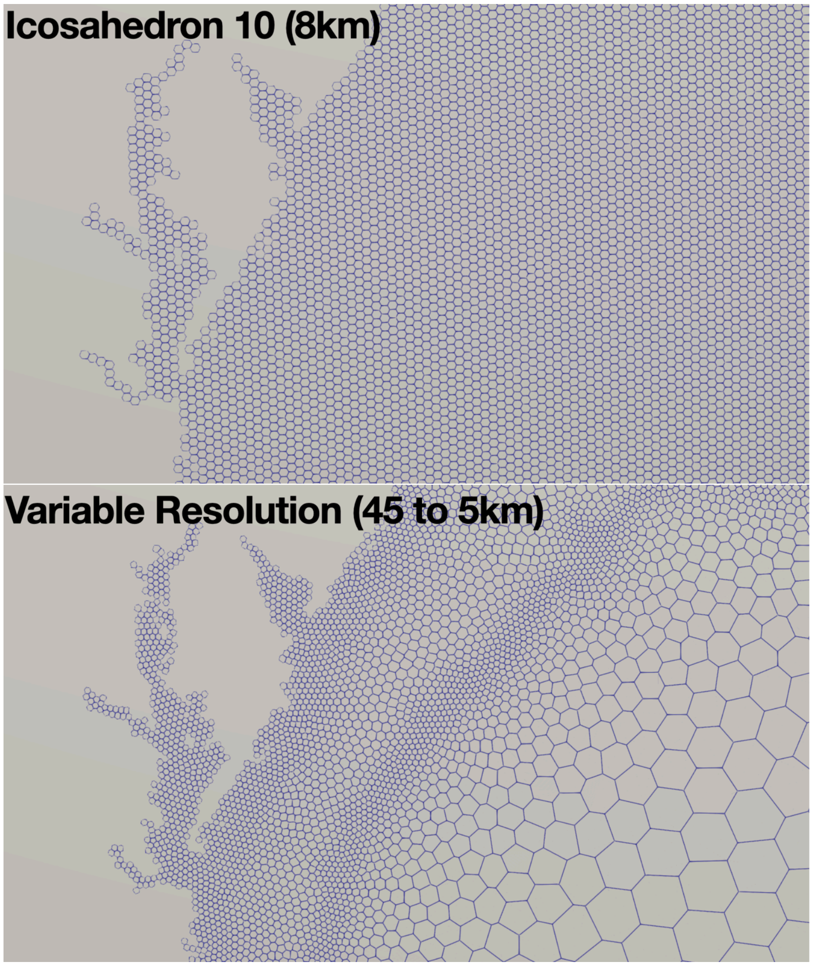

Figure 3.3: Comparison of the Icosahedron 10 mesh (top) and the variable resolution mesh (bottom) in the North Atlantic near Delaware Bay. The Icosahedron 10 mesh is a quasi-uniform 8-km mesh while the variable resolution mesh ranges from 45 km to 5 km.

Mesh Type	Average Cell Width	Wave Drag Coefficient	Number of Cells	Time Step (s)
Icosahedron 7	62.9 km	1.80	163,842	60
Icosahedron 8	31.5 km	1.08	655,362	60
Icosahedron 9	15.7 km	0.72	2,621,442	30
Icosahedron 10	7.87 km	0.36	10,485,762	15
VR 45 to 5	45 to 5 km	0.72	2,359,578	20

Table 3.1: Details for each mesh used in the simulations. Cell width of a polygon is computed as the diameter of a circle with the same area.

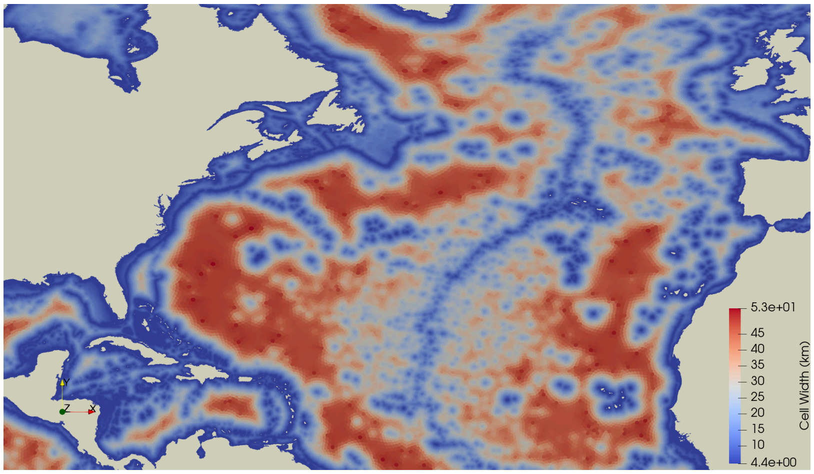

Figure 3.4: View of the variable resolution mesh around the Atlantic Ocean. The colors indicate the size of each cell in the mesh, with blue indicating smaller cell size and red indicating larger cell size. There is more refinement around 1) shallow depths, and 2) regions of steep topographic gradients.

3.2.4 Topographic Wave Drag

Tidal dissipation occurs as a stratified fluid flows over rough topography, causing energy to transfer from barotropic to baroclinic tides (*Munk*, 1966; *Munk and Wunsch*, 1998). Including this topographic wave drag has been shown to decrease the tidal elevation errors in tidal models (*Egbert et al.*, 2004; *Arbic et al.*, 2004; *Green and Nycander*, 2013a; *Lyard et al.*, 2006). Different parameterization methods exist, and several studies include comparisons of various methods (*Egbert et al.*, 2004; *Green and Nycander*, 2013a; *Buijsman et al.*, 2015). Here, we have implemented the scheme proposed by *Jayne and St. Laurent* (2001) which uses a simple tunable scalar,

$$\mathcal{C} = \frac{\pi}{L}\hat{H}^2 N_b. \tag{3.13}$$

Here $\mathcal{C}$ is the same as that in Eq. (3.2), $\hat{H}$ represents the bottom roughness and N_b is the buoyancy frequency at the bottom. L is a wave length representing the topography, which we set to 10 km, as in *Jayne and St. Laurent* (2001) and *Buijsman et al.* (2015). MPAS-Ocean reads in the Hycom variable `rinv`, which is $H/\mathcal{C}$. The value of the parameter χ depends on the resolution (*Arbic et al.*, 2008; *Buijsman et al.*, 2020), and required a tuning of the wave drag for each mesh in this study (Fig. 3.5).

3.2.5 Bathymetry

The quality of bathymetric datasets can impact the errors found in tidal models. In particular, it has been found that Hudson Bay and other areas can significantly change tides in regions around the globe (*Arbic et al.*, 2009; *Pringle et al.*, 2018a). It was demonstrated by *Arbic et al.* (2009) and *Arbic and Garrett* (2010) that regions of large resonant coastal tides, such as Hudson Bay, have a substantial"back effect" on the global ocean tidal system. *Blakely et al.* (2022) showed that tidal errors can be improved by combining GEBCO bathymetry with various high-quality regional bathymetric datasets. Motivated by this, we include a comparison of two different global bathymetric datasets: GEBCO2021 (*GEBCO Compilation Group*, 2021) and SRTM15+ (*Tozer et al.*, 2019), each with regional patching around Canada (*Canadian Hydrographic Service*, 2018), northern Australia (*Beaman*, 2016) and the great barrier reef (*Beaman*, 2010).

3.3 Simulation Details

3.3.1 Tidal Evaluation

It is common to evaluate tidal models by comparing the root-mean squared complex error (RMSE) vs. a benchmark, such as TPXO8 (*Egbert and Erofeeva*, 2002). Here, as in *Arbic et al.* (2004), we separate the errors into three regions: *deep* (depths >1000m and between 66°N and 66°S), *shallow* (<1000m) and global (no restriction). The pointwise RMSE for the tidal constituent, which we also denote by D (for discrepancy) can be computed as

$$D^2 = \frac{1}{2}(A_{TPXO}^2 + A_{MPAS}^2) - A_{TPXO}A_{MPAS}\cos(\phi_{TPXO} - \phi_{MPAS}), \tag{3.14}$$

$$RMSE_{areaweighted} = \sqrt{\frac{\int\int D^2 dA}{\int\int dA}} \tag{3.15}$$

In Eq. 3.15, A_{TPXO} and A_{MPAS} are the M_2 amplitudes and ϕ_{TPXO} and ϕ_{MPAS} are the phases of TPXO and MPAS-Ocean, respectively. The quantity $RMSE_{areaweighted}$ is weighted by the area dA of each cell.

We also evaluate the model against tide gauge observations as

$$D^2 = \frac{1}{2}(A_{tg}^2 + A_{MPAS}^2) - A_{tg}A_{MPAS}\cos(\phi_{tg} - \phi_{MPAS}), \tag{3.16}$$

$$RMSE_{tg} = \sqrt{\sum \frac{D^2}{N_{tg}}} \tag{3.17}$$

where tg denotes tide gauge data and N_{tg} is the number of tide gauge stations. For these comparisons we divide the errors into a different set of categories than we use for the TPXO comparison. These are: *deep* (depths <1000m), *shallow* (depths between 100m and 1000m), and *coastal* (depths <100m). Note that for the tide gauge comparisons, we do not restrict latitude as we do for the TPXO comparisons.

The complete list of simulations is given in Table 3.2. We compare results from different Icosahedral meshes (7, 8, 9, and 10) to results from a variable resolution mesh. We also compare the results of simulations with inline SAL versus scalar SAL for the highest resolutions: Icosahedral 10 and the variable resolution. Furthermore, we tested two different bathymetric datasets: GEBCO 2021 and SRTM15+, each with and without refinement in critical areas. We ran all simulations for 120 days using a fourth-order Runge-Kutta time-stepping method. The tidal phases and amplitudes are calculated from harmonic analysis of the final 90 days of the simulation, allowing for a 30-day spin-up.

Mesh	Bathymetry	SAL type	Global	Deep	Shallow
Icosahedron 7	GEBCO2021	Inline	14.1	12.0	30.0
		Scalar	14.8	12.9	28.8
Icosahedron 8	GEBCO2021	Inline	10.7	8.8	22.5
		Scalar	12.9	11.3	22.7
Icosahedron 9	GEBCO2021	Inline	8.0	6.4	16.3
		Scalar	12.2	10.5	20.5
Icosahedron 10	GEBCO2021	Inline	7.4	5.8	14.0
		Scalar	14.3	12.2	23.8
VR 45 to 5 km	GEBCO2021	Inline	6.8	5.4	13.3
		Scalar	10.4	8.9	17.2
	SRTM15+	Inline	7.0	5.7	12.6

Table 3.2: Complex M_2 error (cm) for all simulations, where columns show error calculations for global (all cells), deep, and shallow water.

3.3.2 Tuning

Two parameters required tuning in order to perform these tests: a wave drag parameter and the interval at which SAL is updated.

3.3.2.1 Topographic Wave Drag

The MPAS-Ocean model follows the Jayne and St. Laurent drag scheme in that it has a single tunable wave drag parameter, χ, as seen in Eq. (3.2). It is necessary to tune the wave drag parameter for each resolution to ensure optimally modeled tides and tidal energy dissipation. Table 3.1 shows the values chosen for each resolution with the sampled wave drag parameters for each resolution shown in Fig. 3.5. We can also see in this figure that as χ approaches 0 (at which point wave drag would be turned off), the errors begin to increase by up to several centimeters.

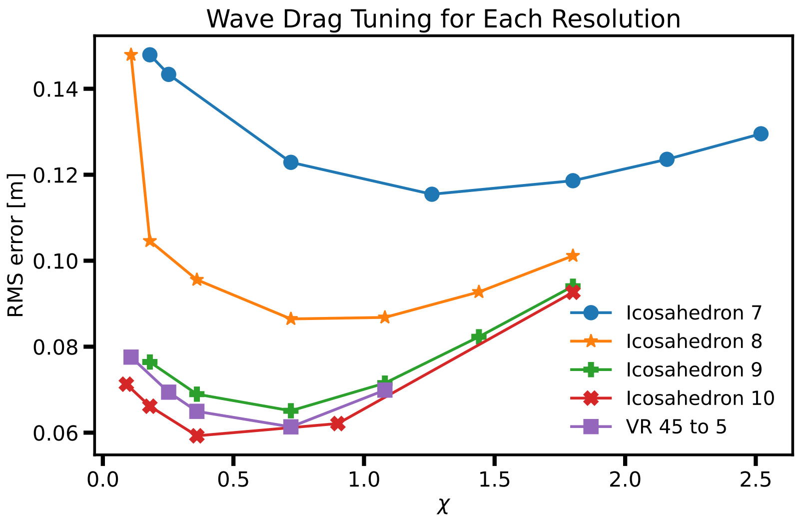

Figure 3.5: Wave drag (χ) tuning for each mesh. These were evaluated with full inline SAL. The optimal wave drag coefficient for each mesh was used to perform all other simulations using that mesh.

Calculation Interval	30 min.	10 min.	1 min.
Icosahedron 8 RMSE (cm)	8.8	8.4	8.4
Icosahedron 9 RMSE (cm)	6.4	6.4	6.5
VR 45 to 5 km RMSE (cm)	6.1	6.1	6.4

Table 3.3: RMSE error for M_2 constituent at different SAL update intervals.

3.3.2.2 SAL Calculation Interval

The full inline SAL calculation can be costly, particularly at high resolution. To help reduce this computational burden, we experimented with updating the value of the SSH perturbation due to SAL at various intervals of 1 minute, 10 minutes, and 30 minutes. We continue to apply SAL at every time step between the update intervals. Table 3.3 shows the resulting M_2 errors on the Icosahedral 8 and 9 meshes for each of these cases. Decreasing the intervals of calculation does not necessarily lead to decreased tidal errors, likely due to other sources of error dominating. Ultimately, we decided that the 30-minute intervals best optimized the benefits of the inline calculation relative to the computational cost. We include further results of the computational cost in Section 3.4.3.

3.4 Results

3.4.1 TPXO8 Comparison

The RMSE for the M_2 tidal constituent as compared to TPXO8 are shown in Table 3.2. Figures 3.6 and 3.7 show the distribution of the M_2 RMS error D in the solution as compared to TPXO8. The decreasing error at finer resolutions demonstrates approximate numerical convergence. The largest errors, particularly in the variable resolution mesh, lie in the region around Antarctica. The E3SM water cycle configurations do not include ice shelf cavities. As such, we are planing a follow-up study focused on the accuracy of tides under those circumstances. For now, the simulations in this paper do not include an explicit representation of ice shelf cavities, which have been shown to impact tidal accuracy, particularly in this region (*Stammer et al.*, 2014; *Blakely et al.*, 2022).

Comparing the results for inline SAL and the scalar approximation (Fig. 3.8), we can see that at every resolution, the deep (>1000m) RMS error improves with the inline SAL. Finer resolution meshes see a larger benefit to inclusion of inline SAL than the coarser resolutions. As the quasi-uniform meshes increase resolution, inline SAL reduces the error by as much as 50%. For the scalar SAL case, the Icosohedron 10 mesh has unusually larger errors. This could be due to keeping the β constant for all cases, rather than tuning it for specific resolutions. Additionally, the wave drag parameter χ was tuned for the inline SAL cases, so further tuning may lead to more typical results for the scalar case on the Icosohedron 10 mesh. For the variable resolution mesh, the improvement is not as large but inline SAL still reduces the error by 39% as compared to the scalar SAL. The lowest error achieved is on the 45-km to 5-km variable resolutions mesh, with a deep M_2 RMS error of 5.4 cm. As a point of comparison, *Schindelegger et al.* (2018) and *Shihora et al.* (2022) both included full inline SAL calculations into a barotropic tide model and found deep

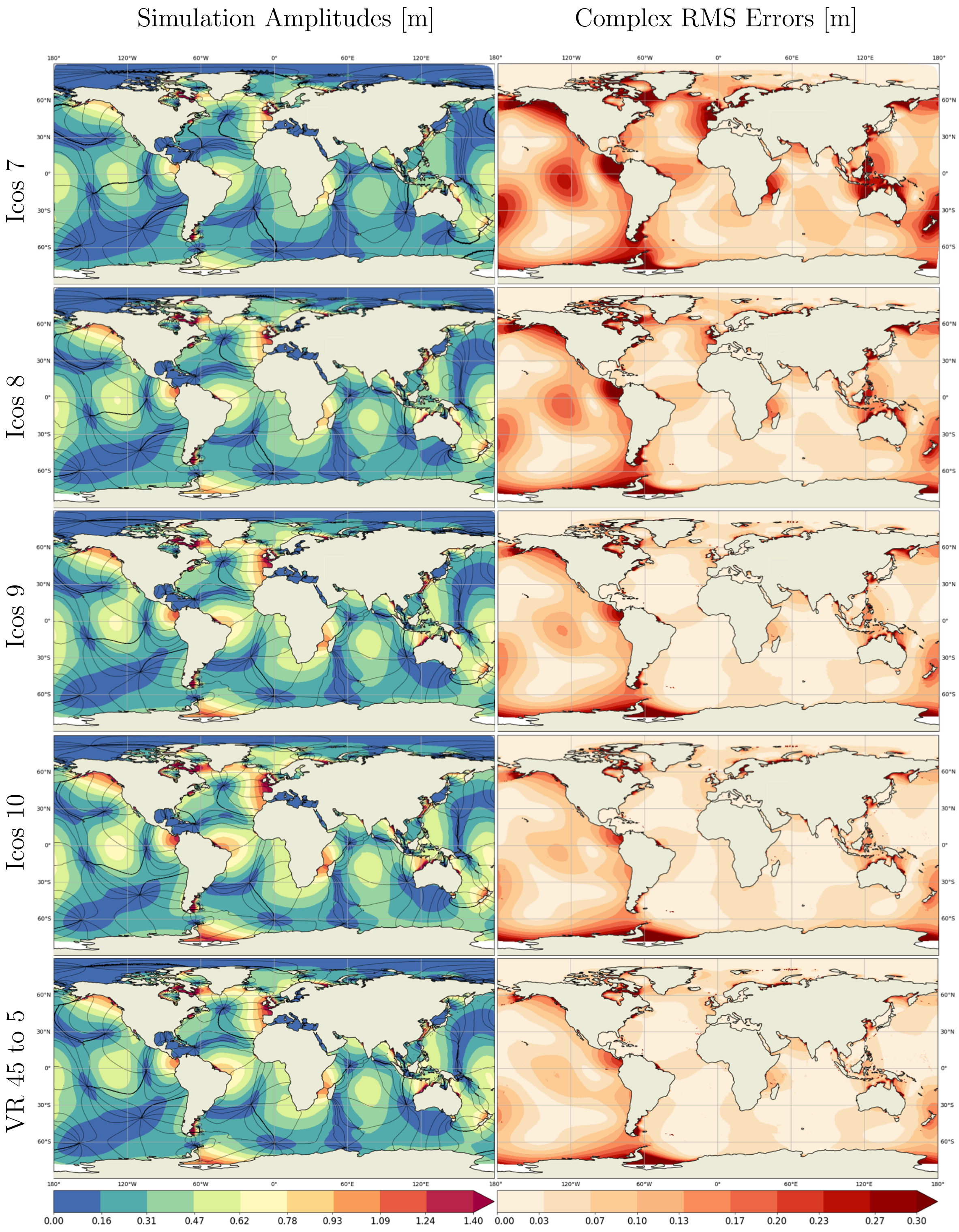

Figure 3.6: Pointwise complex RMS differences (D) between MPAS and TPXO8, showing simulated M_2 tidal amplitudes (colors) and phases (lines) from MPAS-O at various resolutions (left); M_2 RMS errors calculated with respect to TPXO8 data (right). These represent the errors on each mesh obtained from using inline SAL and GEBCO2021 bathymetry.

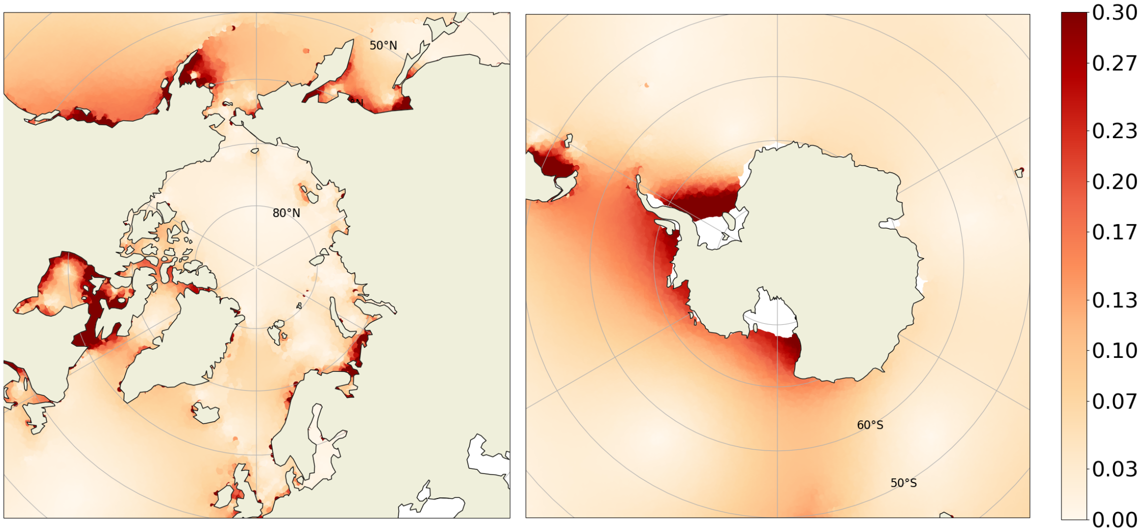

Figure 3.7: RMS error (m) of the variable-resolution simulation versus TPXO8 in the Arctic Ocean (left) and Southern Ocean (right).

ocean M_2 RMS errors of 4.4 cm and 3.4 cm, respectively. Both studies used global $1/12^o$ resolution regular latitude-longitude grids with ice shelf cavities included. The *Schindelegger et al.* (2018) model domain ranged from 86^oS to 84^oN. M_2 RMS errors with ADCIRC were found to be 2.9 cm by *Pringle et al.* (2021a) and were further lowered to 1.9 cm by *Blakely et al.* (2022). All of the previous studies used more sophisticated wave drag schemes, such as a full tensor calculation or optimization of a spatially-dependent coefficient and evaluated RMSE at depths > 1000 m and latitudes $\leq | \pm 66^o|$. The two ADCIRC studies implemented SAL by reading in values from a data-assimilated model and featured a global 2 km to 25 km variable resolution mesh. *Stammer et al.* (2014) includes a comparison of errors for various purely hydrodynamical, non-data assimilative models ranging from 5.3-7.8 cm. While the tidal errors in MPAS-Ocean are not as competitive as some state-of-the art models that focus exclusively on tidal modeling, they are low enough to represent tides in an Earth system model, thus paving the way for studies of tidal interactions with storm surges, rivers, or components of the cryosphere in the future (see Section 3.5). In at least one other run using settings not directly tested here, we have achieved an even

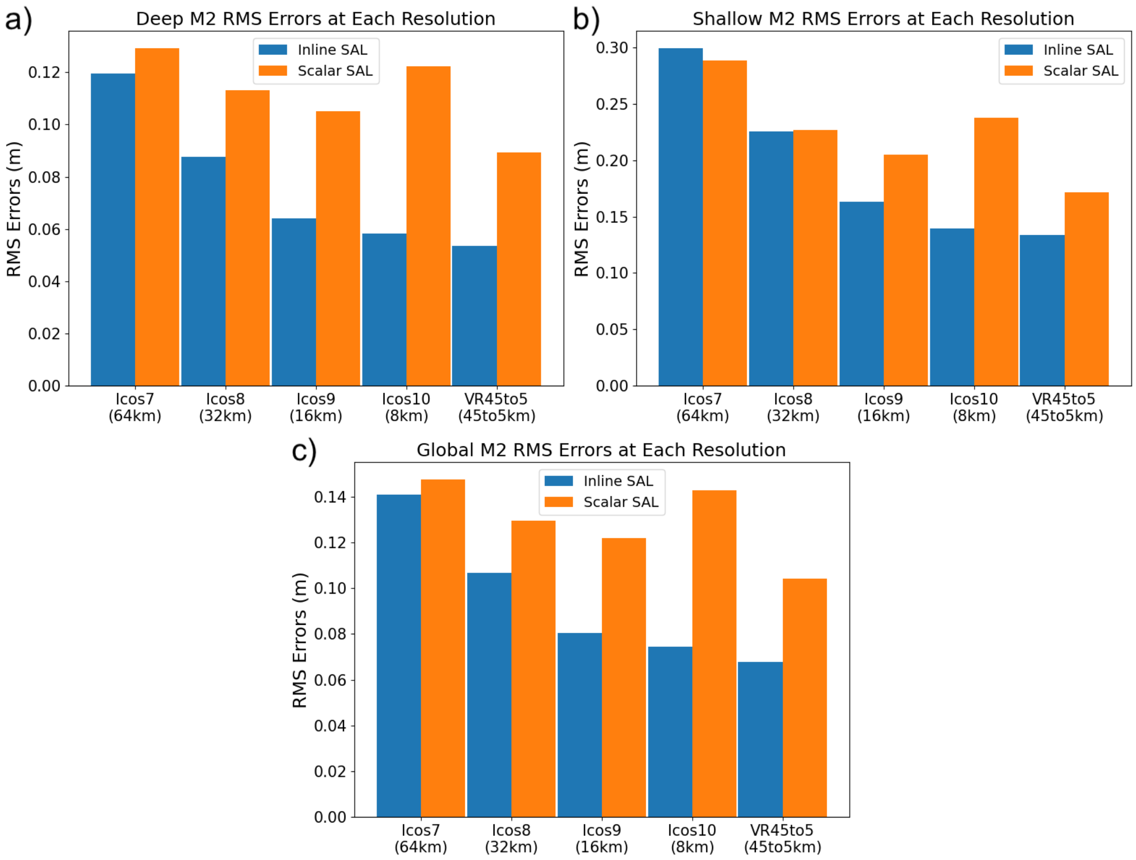

Figure 3.8: M_2 RMS errors relative to TPXO8 for different simulations. The plots show a) deep regions, b) shallow regions, and c) global errors (see Section 3.3.1). Errors reduce with higher resolution, and inline SAL is better than scalar SAL.

lower RMS error of 5.1 cm, indicating there is still room for improvement.

Aside from inclusion of explicit ice-shelf cavities, the errors in our model could be improved by using a more sophisticated wave-drag scheme or a better-optimized variable resolution mesh. Optimization for improved tidal errors on the VR mesh include adjusting the maximum and minimum cell size as well as the limiting gradient that determines the relative increase in cell size. As discussed in the tuning section, the wave drag coefficient is highly dependent on the resolution of the mesh. For the variable resolution mesh, the "best" wave-drag coefficient may be different depending on the resolution of a particular region of cells. Furthermore, we may find that the scalar parameterization of wave drag is not as accurate as a full implementation. The generation of the variable mesh itself also requires decisions about minimum / maximum cell width, and the gradient of cell width (i.e., how rapidly the cell sizes change throughout the mesh). Refining these parameters could lead to further improvement in the results found on the VR mesh.

3.4.2 Tide Gauge Comparison

We compare the results of MPAS-Ocean to tide gauge datasets including the "ground truth" stations (pelagic, shallow, and coastal) from *Stammer et al.* (2014), as well as stations from NOAA, KHOA, JMA, and GESLA. These stations were consolidated by *Pringle* (2019), including directly provided tidal harmonics or using UTIDE (*Codiga*, 2011) on time level histories. Fig. 3.9, shows the model versus tide gauge amplitudes and phases. The tide gauge datasets have been filtered to exclude gauges generally outside of the domain of the simulation. For the phase data, we shifted the values so that the phase differences were all within 180 degrees. The RMS error when comparing against the 151 pelagic stations is 5.8 cm for the variable resolution mesh and 5.9 cm for the 8 km quasi-uniform mesh (Table 3.4), which is consistent with the results seen from the TPXO8 comparison of 5.4 cm and 5.8 cm,

Mesh	SAL type	RMSE (pelagic)		R^2		
				Deep	Shallow	Coastal
Icosahedron 10	Inline	5.9	Amplitude	0.986	0.950	0.933
	Scalar	13.1		0.982	0.952	0.928
VR 45 to 5 km	Inline	5.8		0.983	0.974	0.950
	Scalar	9.3		0.986	0.982	0.959
Icosahedron 10	Inline		Phase	0.993	0.975	0.974
	Scalar			0.991	0.933	0.965
VR 45 to 5 km	Inline			0.994	0.969	0.985
	Scalar			0.993	0.930	0.979

Table 3.4: R^2 values for the M_2 tide gauge amplitude (top) and phase (bottom) comparisons in deep (>1000m), shallow (between 1000m and 100m, and coastal (<100m) regions. The complex RMS error (cm) for the 151 "ground truth" pelagic stations is also included.

respectively, for the deep ocean. For reference, in the previous studies about full inline SAL, *Schindelegger et al.* (2018) had an RMS error of 5.9 cm and *Shihora et al.* (2022) had an error of 4.8 cm when comparing to the pelagic stations.

A large majority of the tide gauges sampled are near the coasts, and we can see from the figures that the MPAS-O has more accurate tides near the deep-ocean gauges (Fig. 3.9). The R^2 value for M_2 amplitudes increases for increasing depths. In the zoomed-in plot showing only tidal amplitudes between 0-1 m, we can see that most of the spread is due to errors in the shallower locations (mainly regions less than 100m deep). Comparing the two different meshes, we can see that while they both give similar results, the variable resolution mesh does outperform the quasi-uniform mesh slightly in the shallower regions. For depths less than 100m, the variable resolution mesh amplitude has a value of $R^2 = 0.950$ compared to the quasi-uniform mesh value of $R^2 = 0.933$. Similarly, for depths between 100m and 1000m, they have values of $R^2 = 0.974$ and $R^2 = 0.950$ respectively. For depths greater than 1000m, we can see a slight advantage in the quasi-uniform mesh, with a value of $R^2 = 0.986$ compared to the variable resolution mesh value of $R^2 = 0.983$. The quasi-uniform mesh has an 8-km resolution over the entire ocean, while the variable resolution mesh has cells as large as 45-km in this region. Despite the slight advantage this gives the quasi-uniform mesh for amplitudes, the variable resolution mesh also has similar or better phase results, leading to reduced RMSE (Fig. 3.4) for this mesh. When comparing the scalar results to the inline SAL, we can see that the inline calculation performs better overall for the Icosahedron 10 mesh, but the variable resolution mesh sees most benefit in the phase errors. Even though the RMSE is higher for both meshes, the amplitude R^2 values are actually higher for the scalar while the phase values are lower. We can also consider the physical spread of errors by separating the tide gauges based on whether their errors are larger or smaller than the RMS error (Fig. 3.10). MPAS-O tidal errors are generally greater than the total RMS error in regions near coastlines, whereas tidal errors in the deep-ocean are generally less than the RMS error. While we expect the shorelines to have larger overall tides and therefore larger errors in the model, the figure also demonstrates that many shallow regions also have lower errors. We expect that once further improvements to the variable resolution mesh allow us to resolve the coastline in better detail, these errors might reduce even further. Additionally, allowing for different wave drag coefficients for different regions may help optimize drag specifically along shelves and coastlines, e.g. as in *Blakely et al.* (2022).

3.4.3 Computational Scaling

We show differences between performance for the inline SAL updated at various intervals and performance on the variable resolution mesh compared to the Icosahedron mesh. All runs were performed on NERSC Cori compute nodes with 2.3 GHz Haswell processors (Intel Xeon Processor E5-2698 v3). For the mesh comparisons, the variable resolution performance is better than the Icosahedron 10 mesh (Fig. 3.11), with comparable RMS errors (Fig. 3.2). Table 3.1 shows the number of cells and the time step needed to run the model on each mesh. The variable resolution mesh allows

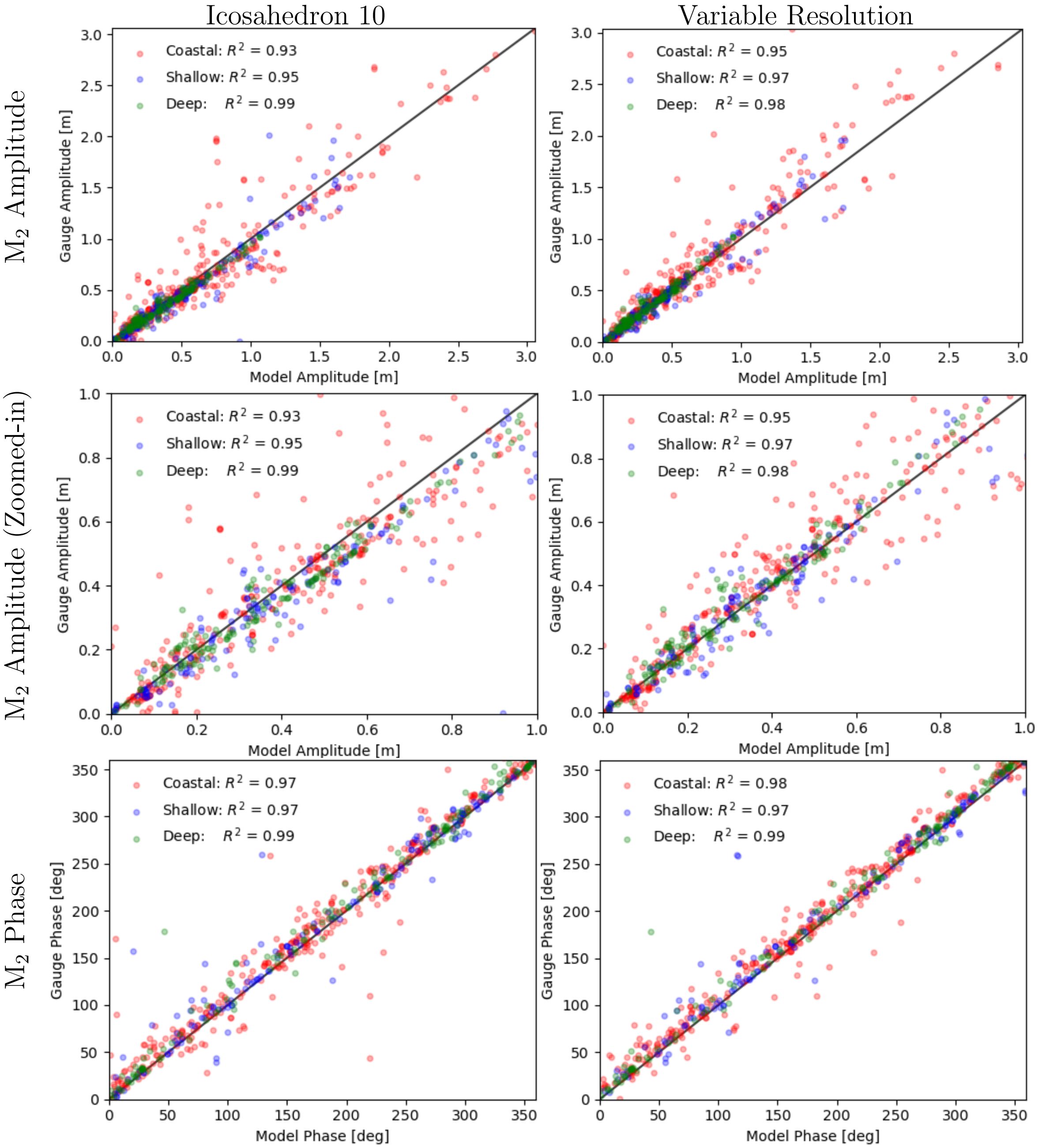

Figure 3.9: M$_2$ tidal results from inline SAL Icosahedron 10 run compared to tide gauge data for the deep, shallow, and coastal tide gauges (see Section 3.3.1). The R^2 values are given in the legend.

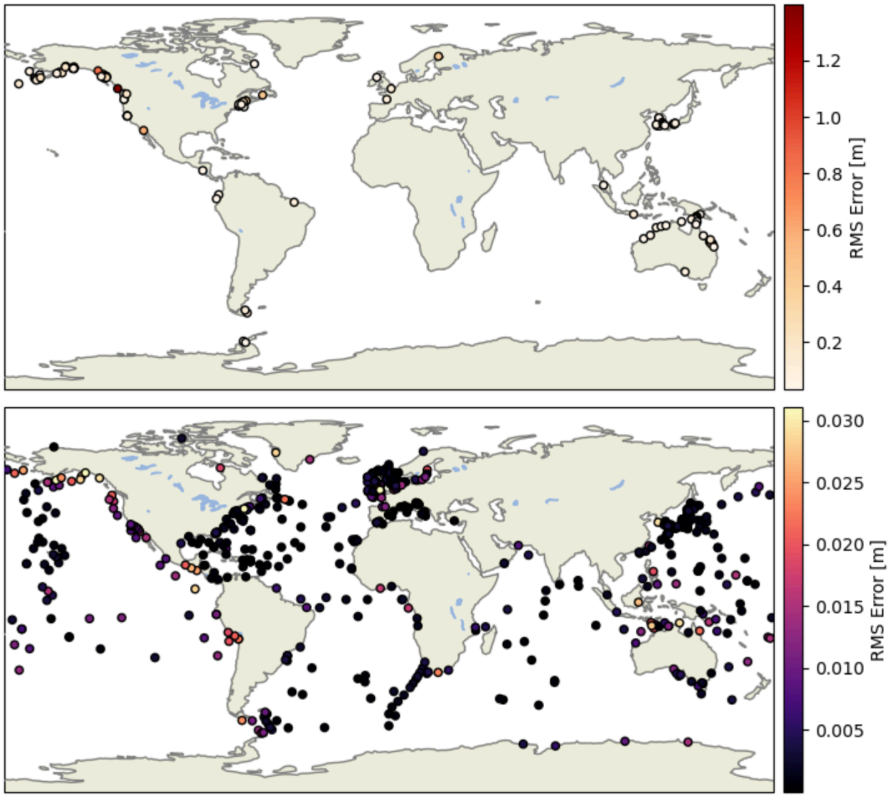

Figure 3.10: Global distribution of tide gauges, colored by model error from the variable resolution mesh simulation. The top plot shows locations with errors greater than the RMS value of all stations, and the bottom plot shows gauges with errors less than the RMS value. The majority of points have a small error, while the small number of stations with large error are near coastlines. This analysis is restricted to gauges at depths $\geq$ 100m

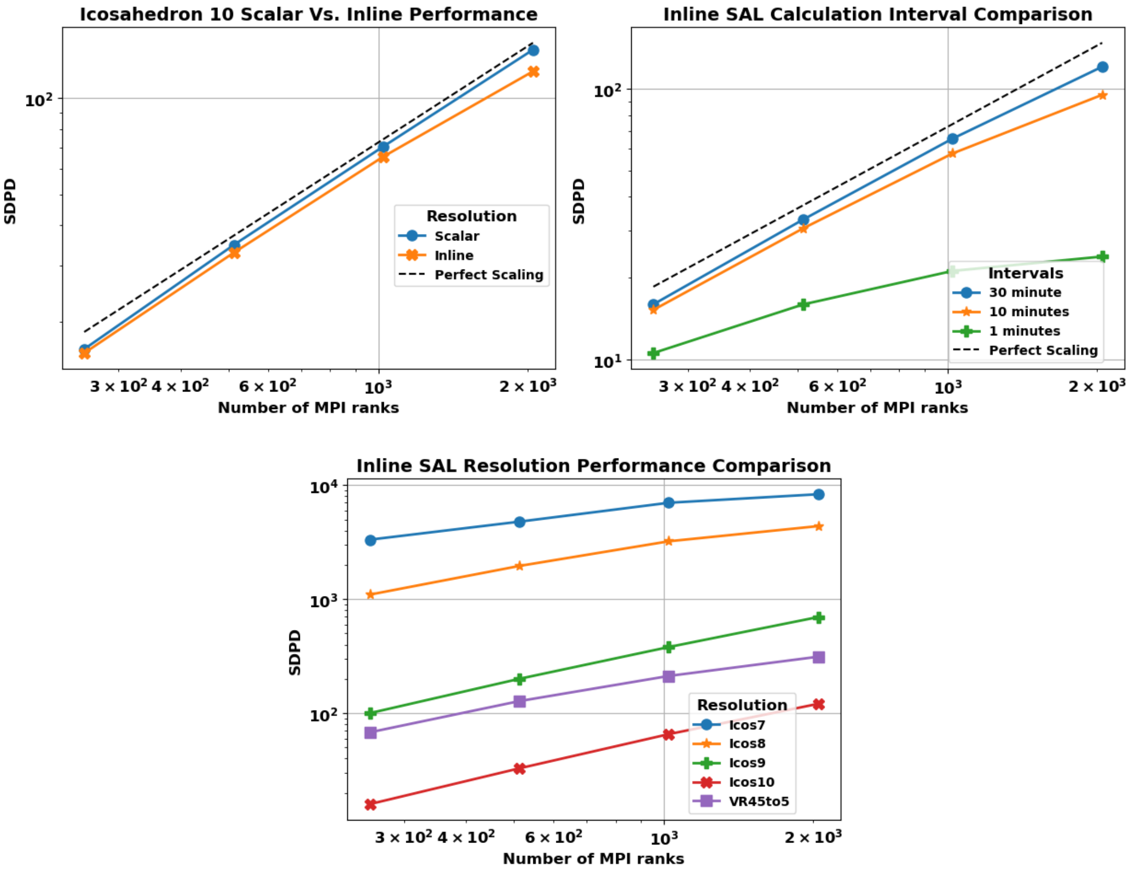

Figure 3.11: Performance comparisons of MPAS-Ocean including: scalar versus inline on Icosahedron 10; SAL update intervals at 1 minute, 10 minutes, and 30 minutes; and performance with inline SAL on all of the meshes used in this study. The computational throughput is measured in units of simulated days per day (SDPD).

for significantly fewer cells, leading to improved computational performance. For all meshes, the explicit time step is restricted by the advective CFL condition, defined as the ratio of the cell width to the wave propagation speed,

$$dt < \frac{\text{cell width}}{\text{wave speed}}, \quad \text{wave speed} = \sqrt{gh} \tag{3.18}$$

where dt is the time step, h is the water depth, and g is the gravitational constant. In ocean flows, the surface gravity wave speeds produces the fastest velocities. For the variable resolution mesh, this condition means that the time step is not necessarily limited by the minimum cell size alone, but by the relationship between cell sizes and wave speeds throughout the domain. Noting that our variable resolution heuristics (see Section 3.2.3) place fine resolution in shallower, and hence lower wave-speed regions, the overall CFL restriction is found to be significantly less onerous than quasi-uniform configurations that employ higher resolution in the deep ocean. In our simulations, not only does the 45-km to 5-km mesh have fewer cells than the 8-km mesh and higher resolution around the coasts, it also runs with a larger time step as can be seen in Table 3.1.

While the inline SAL calculations do increase the computational cost, Table 3.3 shows that there is only a small difference in the RMS error when updating the SAL term at larger intervals than the model time step. In fact, at higher resolutions we see that the more frequent updates may lead to higher errors. Fig. 3.11, which plots simulation run time performance, demonstrates that updating the SAL perturbation every 30 minutes can improve the computational performance as compared to evaluation at more frequent time steps. When using a 30 minute interval, the computational performance of the full SAL calculation is marginally but not marginally larger than the scalar implementation. Based on the scaling and the RMS errors, either 30 minutes or 10 minutes may actually be the ideal update interval for the SAL, providing computational benefit over the 1 minute or more frequent intervals with little decrease in tidal accuracy.

3.5 Conclusions

In this paper, we demonstrated the feasibility of calculating tides within the MPAS-Ocean model employing a full inline SAL calculation in high-resolution barotropic simulations. We also examined sensitivities of the modeled tide to the SAL calculation method, careful selection of bathymetric datasets, model resolution, and a tuned wave drag coefficient. The full SAL calculations showed decreases in tidal RMS elevation errors of several centimeters across all meshes tested, relative to results computed using the scalar approximation for SAL. The variable resolution mesh had tidal errors similar to that of the Icosahedron 10 mesh, but with better computational performance, lying closer to results computed on the Icosahedron 9 mesh. Comparison of simulations using the different bathymetric datasets show that GEBCO2021 slightly outperforms SRTM15+ on the variable resolution mesh. The computational performance of the full SAL can incur large costs when evaluated at every time step. It appears that this cost can be mitigated by updating SAL at 10 or 30 minute intervals, rather than at every time step, with little effect on tidal errors. Another avenue for increasing the computational efficiency is evaluation of the spherical harmonics in parallel, rather than the serial routines implemented by the SHTns package used in this study. This can be done by evaluating the integrals directly on the MPAS mesh so that the interpolation step is not needed, as pursued in a related study by our group. Comparison to tide gauge data shows that this first attempt at including tides results in slightly larger errors than tides in some other models (*Pringle et al.*, 2021a; *Schindelegger et al.*, 2018; *Stammer et al.*, 2014; *Blakely et al.*, 2022). However, we expect that the RMS errors for the M_2 tide could be improved with a) variable resolution meshes with smaller minimum cell size, b) optimization of parameters in the variable resolution mesh generation, c) the addition of a spatially-dependent wave drag coefficient or a more sophisticated wave drag scheme (e.g., *Green and Nycander* (2013a)), and d) the inclusion of ice-shelf cavities.

It is becoming clear that inclusion of tides is important for predictions of future climate and extreme sea level events (*Bindoff et al.*, 2019; *Oppenheimer et al.*, 2019a). Our results show that MPAS-Ocean has relatively low tidal errors that are small enough to merit inclusion within a full climate system model. An important difference between the setup described for the barotropic case in this paper, and the setup needed for use in a full baroclinic framework, is the variable which is used in the SAL calculations. As mentioned in the discussion on SAL, tidal elevations can be used for spherical harmonic decomposition in the barotropic case because it is a direct measure of the mass of the water column. By contrast, baroclinic simulations require bottom pressure anomalies for this purpose. Furthermore, implementation of tides in a baroclinic model calls for some modifications to the topographic wave drag, such as by applying wave drag to the flow averaged over the bottom 500 m (e.g., *Arbic et al.* (2018)) or using different parameter optimizations. The addition of tides in an Earth system model will allow us to examine a number of advanced aspects in the physical Earth system. For example, there is a need for inclusion of tides when considering the Arctic ocean and sea ice (*Holloway and Proshutinsky*, 2007) as tides can have a substantial effect on sea ice volume and salinity (*Luneva et al.*, 2015). A review of tidal influences on ice sheets by *Padman et al.* (2018) suggests that feedback between ice shelf geometry and tidal currents could imply a need for explicit tides in Earth system models; see also *Williams et al.* (1985) and *Dinniman et al.* (2016). Tides also have important effects on estuaries. *Ruault et al.* (2020) found that baroclinic tides can influence the Amazon plume, which itself can impact the Atlantic climate (*Jahfer et al.*, 2017). High-frequency interactions of tides with storm surges and fluvial processes in estuaries *Orton et al.* (2012), *Spicer et al.* (2019) are important for predicting coastal flooding during extreme weather events. In future studies, we plan to use MPAS-Ocean to explore these interactions between tides and other components of the Earth system (e.g., ice shelves and basal melt rates, sea ice, estuaries) and their potential impacts on future climate.

CHAPTER IV

Further Improvements to MPAS-Ocean Tide Modeling with Topographic Wave Drag Parameterization

4.1 Introduction

We can accurately model most large-scale sea-level fluctuations due to tidal forcing on the ocean with a single-layer ocean model in which the horizontal velocities are uniform ("barotropic") throughout the entire water column. The actual ocean, however, features stratified layers. Tidal forcing in these stratified conditions yield waves within the layers known as *baroclinic tides*, or *internal tides*. While tidal models traditionally focused on energy dissipation due to friction with the seabed in shallow regions, *Egbert and Ray* (2000) showed that 25-30% of tidal dissipation occurs in the deep ocean due to energy flow from the barotropic tide into internal tides as flow over rough topography leads to vertical motion between the density layers of the stratified ocean. Several methods of parameterizing this flow of energy from large-scale barotropic tides to shorter-scale internal tides have been developed over the years, leading to varying improvements in the accuracy of tidal models.

One early method to parameterize this topographic wave drag, developed by *Jayne and St. Laurent* (2001), was implemented into the Model for Prediction Across Scales

(MPAS-Ocean) due to its simplicity of incorporating a scalar term (i.e., by multiplying the drag term in the momentum equation by a scalar field) that is dependent on the mean-squared bottom roughness of the ocean, averaged over grid cells. This method was used in *Barton et al.* (2022) and *Pal et al.* (2023) to incorporate bottom roughness and buoyancy data from a separate ocean model called the Hybrid Coordinate Ocean Model, or HyCOM, based on calculations described in *Buijsman et al.* (2016), rather than calculated internally in MPAS-Ocean. However, due to limitations from different grids and bathymetry datasets, we were interested in exploring whether improving the current formula, through calculation of variables on the native grid, or changing the parameterization scheme altogether could lead to significant improvements in the tides.

Some work has already been done to compare the use of topographic wave drag schemes within a barotropic tide model. *Green and Nycander* (2013b) compared three popular methods: first, the previously mentioned Jayne and St. Laurent; second, another scalar parameterization by *Zaron and Egbert* (2006), which incorporates the horizontal gradients of topography instead of their mean variations; lastly, a more physically-based tensor scheme developed by *Nycander* (2005a) where the momuntum drag term is multiplied by a second-order tensor field instead of a scalar field. Another study by *Buijsman et al.* (2015) compared Jayne and St. Laurent to the original Nycander and two modified versions. Both studies found that the tides' total root-mean-square error Root-Mean-Squared Error (RMSE) decreased when using the Nycander formula.

In this study, we test the two scalar topographic wave drag TWD parameterizations: Jayne and St. Laurent (JSL) and Zaron and Egbert ZAE. We also include a modified version of the Nycander scheme used in the Advanced Circulation, or ADCIRC, model *Pringle et al.* (2021b). This version, known as the Local Generation Formula LGF, has the benefit of remaining a physically-based tensor scheme but is simpler to implement (*Pringle et al.*, 2018c). In the following sections, we discuss the details of each method, followed by results on improvements in the tides.

4.2 Topographic Wave Drag Schemes

Topographic wave drag (TWD) is included as a dissipative term within the momentum equation for the barotropic ocean model,

$$\begin{aligned}\frac{\partial \mathbf{u}}{\partial t} + (\nabla \times \mathbf{u} + f\mathbf{k}) \times \mathbf{u} &= -\nabla K - g\nabla(\eta - \eta_{EQ} - \eta_{SAL}) \\ &\quad -\chi \frac{\mathcal{C}\mathbf{u}}{H} - \frac{\mathcal{C}_D|\mathbf{u}|\mathbf{u}}{H},\end{aligned} \tag{4.1}$$

where $\mathbf{u}$ represents the depth-averaged horizontal velocity, t is the time coordinate, f is the Coriolis parameter, $\mathbf{k}$ is the vertical unit vector, $K = |\mathbf{u}|^2/2$ is the kinetic energy, g is the gravitational acceleration constant, η is the sea-surface height relative to the moving bed, henceforth called SSH, η_{EQ} is the equilibrium tide, η_{SAL} is the perturbation of tidal elevations due to SAL, $\frac{\mathcal{C}}{h}$ is a topographic wave drag time scale, H is the resting depth of the ocean, and h is the total ocean thickness such that $H + \eta = h$. $\mathcal{C}$ can be either a scalar value ($\mathcal{C}_{JSL}$, $\mathcal{C}_{ZAE}$) or a tensor ($\mathbb{C}_{LGF}$), with descriptions of each parameter in the following sections. The tuning parameter, χ is tuned independently for each parameterization based on the RMS error in the M_2 tides after a 30-day simulation with a 7-day spin-up period.

4.2.1 Jayne and St. Laurent

The scheme proposed by *Jayne and St. Laurent* (2001) uses a simple tunable scalar combined with the average roughness of the topography within a grid cell. This method is more empirically-based than the other two schemes, based on the statistics of bathymetric roughness and dimensional analysis *Green and Nycander*

(2013b).

$$\mathcal{C}_{JSL} = \frac{\pi}{L}\hat{H}^2 N_b. \tag{4.2}$$

Here, $\hat{H}$ represents the bottom roughness and N_b is the observed buoyancy frequency at the bottom. L is a wave length representing the topography, set to 10 km as in *Jayne and St. Laurent* (2001) and *Buijsman et al.* (2015). The roughness of topography, $\hat{H}$ is determined by calculating the standard deviation of the residual heights after fitting the topography within each cell to a planar fit,

$$\hat{H} = std(\Delta H) = std(h_t - (a + bx + cy + dxy)), \tag{4.3}$$

where *std* is the standard deviation calculation, h_t is the topography heights within a grid cell, a, b, c, and d are best-fit coefficients between the polynomial and the topographic data, and x, y are the latitude and longitude values of the topographic data points within a cell, respectively.

4.2.2 Zaron and Egbert

The scheme described in *Zaron and Egbert* (2006) is another scalar parameterization that is easy to implement and has been used successfully in global tide models, such as by *Schindelegger et al.* (2018). ZAE is more analytically-based than the previously described JSL scheme, and uses a simplification of the Wentzel–Kramers–Brillouin approximation, which expresses the baroclinic energy conversion based on linear wave theory.

$$\begin{aligned}
\mathcal{C}_{ZAE} &= \Gamma H(\nabla H)^2 \frac{N_b \bar{N}}{8\pi^2\omega} && (4.4)\\
N(z) &= e^{z/1300} && (4.5)\\
\bar{N} &= 1300 N_0 \big(1 - e^{-H/1300}\big)/H && (4.6)
\end{aligned}$$

where H is the bottom depth, N_b is buoyancy frequency evaluated at the ocean bed ($N(-H)$), ω is the frequency of tidal motions which we take to be the M_2 frequency (1.405×10^{-4}), $\bar{N}$ is the vertical average of the buoyancy frequency, and the constants $N_0 = 5.24 \times 10^{-3}$ and $\Gamma = 50$ are taken from *Green and Nycander* (2013b). $(\nabla H)^2$ is calculated as the square-magnitude of the horizontal gradients of the topography.

4.2.3 Local Generation Formula

The Local Generation Formula is a tensor-based scheme used in the ADCIRC model (*Pringle et al.*, 2018b,c, 2021b). This scheme is distinct from the *nonlocal* Nycander scheme from which it is derived. The Nycander formulation is a semi-analytical scheme derived from linear wave theory (*Nycander*, 2005b). It has the benefit of including nonlocal effects of topography. LGF is a localized version of the Nycander scheme with two primary benefits. First, it is much simpler and is computationally efficient to calculate. Second, unlike the Nycander scheme, the LGF scheme contains a positive-definite tensor, which ensures the term always dissipates energy.

$$\mathbb{C}_{LGF} = \frac{\left[(N_b^2 - \omega^2)(N_m^2 - \omega^2)\right]^{1/2}}{4\pi\omega} \begin{pmatrix} (\nabla_\lambda H)^2 & \nabla_\lambda H \nabla_\phi H \\ \nabla_\lambda H \nabla_\phi H & (\nabla_\phi H)^2 \end{pmatrix}, \tag{4.7}$$

where N_b is the observed buoyancy frequency, N_m is the depth-averaged buoyancy frequency, $\omega = 1.405 \times 10^{-4}$ is the tidal frequency, and $\nabla_\lambda H$, $\nabla_\phi H$ are the longitudinal and latitudinal gradients, respectively.

To implement LGF as described above, the tensor would be multiplied by a velocity vector, $\mathbf{u} = (u_\lambda, v_\phi)$ where u_λ and v_ϕ are the longitudinal and latitudinal velocities. However, MPAS-Ocean uses a different coordinate system from ADCIRC where the velocities are $\mathbf{u} = (u_\parallel, v_\perp)$, i.e. the coordinates are normal and perpendicular to the cell edge. To account for this, we can rotate the gradients to fit the new coordinate system (4.8), which leads to a relation between the momentum update and the LGF tensor in 4.9.

$$\begin{pmatrix} \nabla_{\|} H \\ \nabla_{\perp} H \end{pmatrix} = \begin{pmatrix} \cos(\theta_e) & -\sin(\theta_e) \\ \sin(\theta_e) & \cos(\theta_e) \end{pmatrix} \begin{pmatrix} \nabla_{\lambda} H \\ \nabla_{\phi} H \end{pmatrix} \tag{4.8}$$

$$\frac{\partial}{\partial t} \begin{pmatrix} u_{\|} \\ u_{\perp} \end{pmatrix} \sim \begin{pmatrix} (\nabla_{\|} H)^2 & \nabla_{\|} H \nabla_{\perp} H \\ \nabla_{\|} H \nabla_{\perp} H & (\nabla_{\perp} H)^2 \end{pmatrix} \begin{pmatrix} u_{\|} \\ u_{\perp} \end{pmatrix} \tag{4.9}$$

When running simulations in MPAS-Ocean, only the velocity perpendicular to the cell edge is updated. The velocity parallel to the edge is calculated, but not used to update the state of the model. Therefore, we only need to use the bottom row in the LGF tensor. In practice, the topographic gradients are evaluated in latitude-longitude coordinates and then rotated using Eq. 4.8. Then, the term in the model becomes

$$\mathbb{C}_{LGF} = \frac{\left[(N_b^2 - \omega^2)(N_m^2 - \omega^2)\right]^{1/2}}{4\pi\omega} \Big[\big(\nabla_{\|} H \nabla_{\perp} H\big) u_{\|} (\nabla_{\perp} H)^2 v_{\perp} \Big]. \tag{4.10}$$

4.3 Results

We found that ZAE was associated with the lowest RMS errors in our tide model. Fig. 4.1 shows the results of tuning for each scheme. The deep RMS complex M_2 error when compared to TPXO8 is 3.5 cm ($\chi = 0.3$) for ZAE, 4.0 cm ($\chi = 3000$) for LGF, and 5.1 cm ($\chi = 11.0$) for JSL. We expected LGF to perform well due to using a more physically-based tensor formulation, but for our model ZAE seems to work the best. Fig. 4.2 shows a comparison of the RMS values for the tuned wave drags at different regions. For both shallow and deep regions, ZAE still performs better than either of the other schemes. The map of RMS errors for the tuned ZAE scheme is in Fig. 4.3. We can see that there are still larger errors in regions of larger tides near coastlines. However, overall the ZAE scheme improves tidal results in the MPAS-Ocean model.

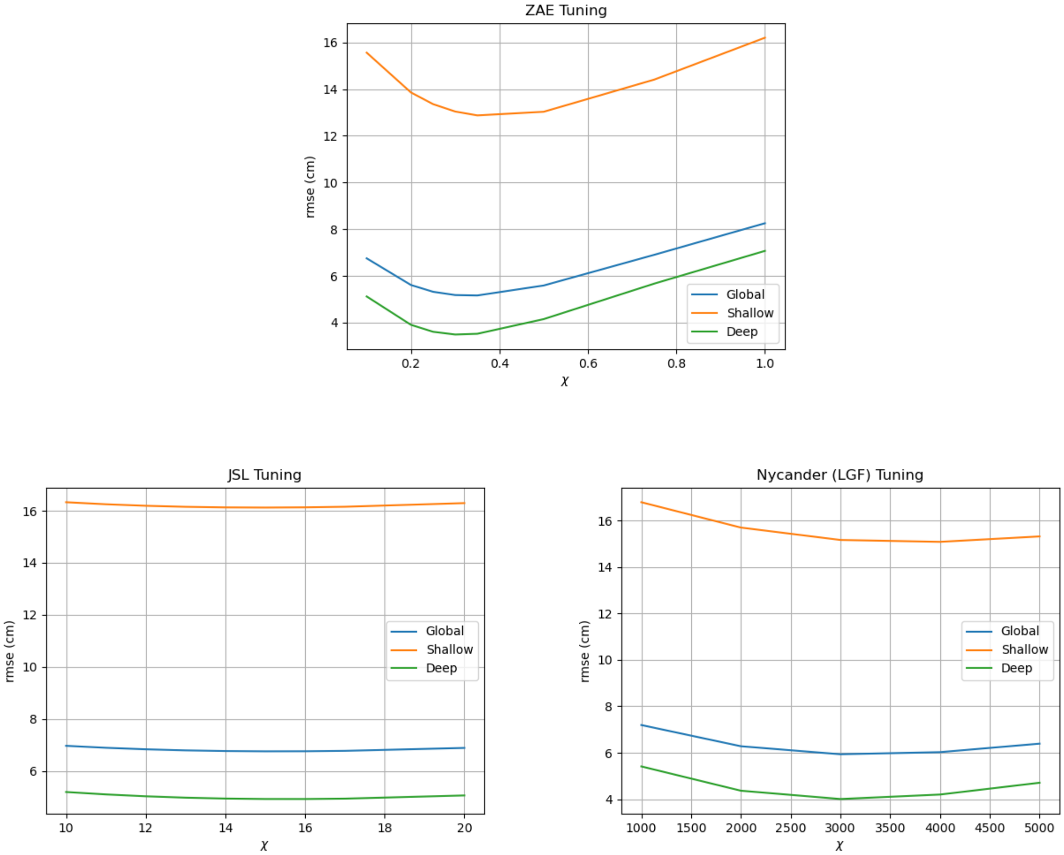

Figure 4.1: The figures above show the impact of tuning the value of χ for each constituent. LGF had the largest tuning parameter overall. JSL did not improve very much with tuning, having overall large RMS errors.

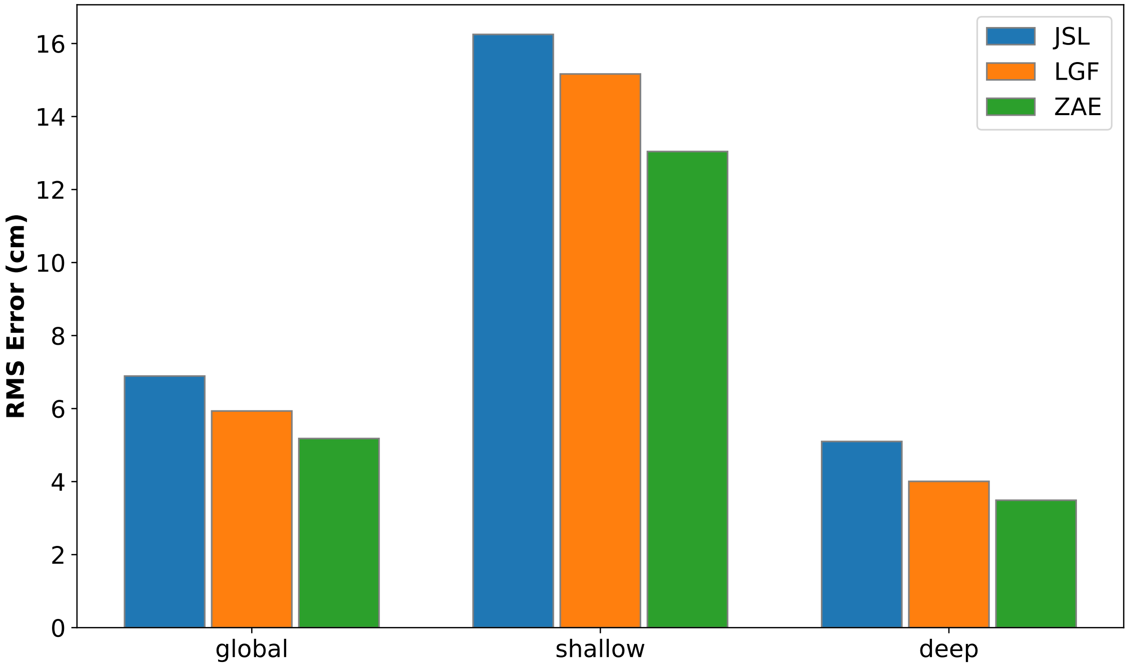

Figure 4.2: Plot of best tuning case for each TWD scheme, and comparing the global, shallow, and deep regions. The ZAE scheme performs best in every region.

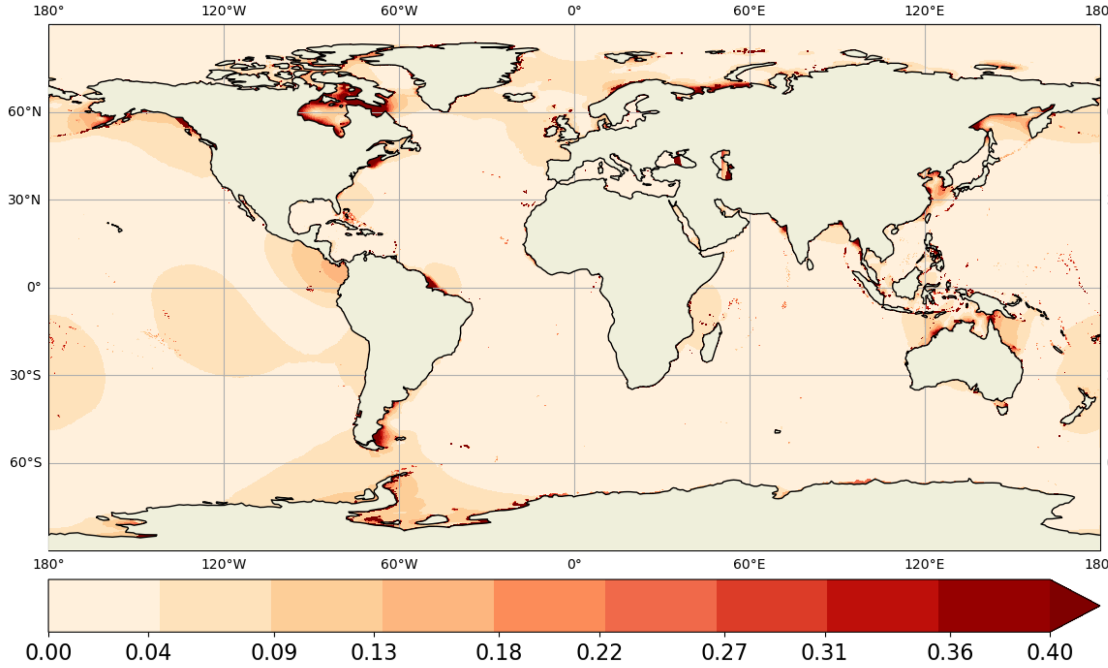

Figure 4.3: Global map of RMS errors using the best TWD scheme, ZAE with $\chi = 0.3$.

CHAPTER V

Impacts on Future Tides from Changes in Sea-Level, Ice Shelf Cavity Geometry, and Landfast Ice Extent

This chapter is a draft of a manuscript currently being prepared for publication.

5.1 Introduction

Climate change continues to impact the earth as the environmental policies of nations around the world will likely result in warming of over 2.0^{o}C by 2100 (*Raftery et al.*, 2017). Many European cities are expected to experience increases in both drought and flood risks (*Guerreiro et al.*, 2018), and ice sheet melt could contribute up to 25 cm in sea-level rise and slow the Atlantic overturning circulation (*Golledge et al.*, 2019), which can influence flood risks along the southeast United States coast (*Volkov et al.*, 2023). Tropical communities are facing losses to fisheries and agriculture (*Cinner et al.*, 2022), and regional studies show that tides in some areas, such as the Pearl River Delta, could become amplified by up to 2.1 m (*De Dominicis et al.*, 2020).

Understanding how tides will change globally over the next century is essential for predicting local changes to tides and flood risks. Many studies have worked to understand how sea-level changes may influence tides in the near future. For example, *Pickering et al.* (2012) and *Idier et al.* (2017) both look at how sea-level rise may impact tides along the European shelf; *Hall et al.* (2013) focuses on changes in paleotides in the Delaware Bay, with some discussion of future tides showing that sea-level rise can lead to sizeable spatial variability even within the bay as tides increase in some areas and decrease in others; *Luz Clara et al.* (2015) observed nonlinear, spatially-varying changes in M_2 tidal amplitudes in simulations of the Patagonian shelf with sea-level rise, *Kuang et al.* (2017) found potential tidal amplitude changes of up to 2 m in the China Sea; *Thompson et al.* (2021) shows that the US coast will experience higher frequency of high-tide flooding with sea-level change, while *Schindelegger et al.* (2018) and *Pelling et al.* (2013) both examine global tidal changes with sea-level rise. Some studies also explore the importance of the cryosphere on tides. For example, *Wilmes et al.* (2017) focuses on tides in the case of large-scale ice sheet collapse; *Murty* (1985) is a regional study examining the influence of ice cover on tides and other hydrographic characteristics in Tuktoyaktuk Harbor; *Bij de Vaate et al.* (2021) shows seasonal modulation of the M_2 tides up to 25 cm in the Arctic due to changes in landfast ice coverage; *Hayden et al.* (2020) explores ocean tides in Hudson Bay and the impacts ice sheet retreat will have over the next few centuries; *Wilmes et al.* (2019) looks at the impact of ice sheets on tidal mixing. However, the near-term effects of ice-sheet changes and their relative impact on global tidal amplitudes compared to sea-level changes are still poorly understood.

In this paper, we look at the impacts of sea-level change, ice shelf cavity geometry, and reduction of landfast ice in influencing tides over the near term, focusing on time slices at 2015, 2060, and 2100. We also examine the nonlinearity of the three factors by comparing individual influence to a combined simulation that includes all changes.

5.2 Methods

5.2.1 Model Details

To study the influence of various changes to the Earth system on tides, we use a barotropic (depth-averaged) tidal configuration of the Department of Energy's Model for Prediction Across Scales (MPAS-Ocean) (*Golaz et al.*, 2019; *Petersen et al.*, 2019). One of the benefits of using MPAS-Ocean is its use of variable resolution meshes, allowing for global ocean simulations that can focus high resolution on areas of interest while reducing computational cost. These meshes are based on Spherical Centroidal Voronoi Tesselations in which cells are placed based on a specified density function and then regularized using an iterative calculation (*Ringler et al.*, 2008). The governing equations of MPAS-Ocean consist of the 2-D shallow water equations written in the following vector-invariant form:

$$\begin{aligned} \frac{\partial \mathbf{u}}{\partial t} + (\nabla \times \mathbf{u} + f\mathbf{k}) \times \mathbf{u} &= -\nabla K - g\nabla\left(\eta - \eta_{EQ} - \eta_{SAL}\right) \\ &\quad -\frac{\nabla p^s}{\rho_0} - \chi\frac{\mathcal{C}\mathbf{u}}{H} - \frac{\mathcal{C}_D|\mathbf{u}|\mathbf{u}}{H}, \end{aligned} \tag{5.1}$$

$$\frac{\partial h}{\partial t} + \nabla \cdot (h\mathbf{u}) = 0, \tag{5.2}$$

$$p(x,y,z) = p^s(x,y) + \rho_0 g h, \tag{5.3}$$

where $\mathbf{u}$ is the depth-averaged horizontal velocity, t is the time coordinate, f is the Coriolis parameter, $\vec{k}$ is the vertical unit vector, K is the kinetic energy, g is the gravitational acceleration constant, η is the sea-surface height (measured relative to the unperturbed ocean surface height), η_{EQ} is the height of the equilibrium tide, η_{SAL} is the height of the sea-surface perturbation due to self-attraction and loading (SAL), p^s is the surface pressure on the ocean due to ice shelf cavities, $\rho_0 = 1035\frac{km}{m^3}$ is the average density of seawater, χ is a tunable dimensionless scalar, $\frac{\mathcal{C}}{H}$ is a topographic wave drag time scale where H is the resting depth of the ocean and h is total ocean thickness such that $H = \eta + h$, and C_D is the bottom friction coefficient. These equations, in vector-invariant form, separate the advection term into a curl term and a kinetic energy term using the identity $(\mathbf{u} \cdot \nabla)\mathbf{u} = (\nabla \times \mathbf{u}) \times \mathbf{u} + \nabla |\mathbf{u}|^2/2$, which can help in conserving kinetic energy (*Ringler et al.*, 2010).

The present setup of the barotropic configuration includes the bottom friction and ice shelf cavity improvements detailed in *Pal et al.* (2023). The ice shelf cavity forcing does not include dynamic coupling between the ice sheets and the ocean. Instead, the pressure, p^s, is added to the governing equations and is calculated as $p^s = \rho g D$ where D is the ice shelf draft beneath the ocean and ρ is the density of the displaced water. The model also includes the parallel implementation of inline self-attraction and loading introduced by *Brus et al.* (2023), with the SAL term updated in 15-minute intervals to both decrease computational cost and improve tidal errors.

Topographic wave drag occurs when a stratified fluid flows over rough topographic features. It is important for calculating tides due to its role in transferring energy from barotropic to baroclinic tides. This process cannot be explicitly calculated in barotropic tide models, and several methods exist to parameterize the process. Previous studies using MPAS-Ocean as a barotropic tide model (*Barton et al.*, 2022; *Pal et al.*, 2023) parameterized the topographic wave drag using the Jayne and St. Laurent formulation (*Jayne and St. Laurent*, 2001). In this study, we have instead implemented the Zaron and Egbert formulation (*Zaron and Egbert*, 2006; *Green and Nycander*, 2013b):

$$\begin{aligned} \mathcal{C} &= \Gamma H (\nabla H)^2 \frac{N_b \overline{N}}{8\pi^2 \omega}, && (5.4) \\ N(z) &= N_0 e^{z/1300}, && (5.5) \end{aligned}$$

where $\mathcal{C}$ is the same as in eqn. 5.2, Γ is an independent tunable scalar, H is the resting depth of the ocean, $N(z)$ is the buoyancy frequency at depth z, N_b is the buoyancy frequency evaluated at the ocean floor ($z = -H$), and $\overline{N}$ is the depth-averaged buoyancy frequency, and ω is the frequency of the M_2 tide. We use the same values of $\Gamma = 50$ and $N_0 = 5.24 \times 10^{-3}$ as described in *Green and Nycander* (2013b).

5.2.2 Simulation Details

The current capability of the tidal model has improved the M_2 root-mean-square error (RMSE) to 3.3 cm in the deep ocean ($H < 1000m$) for latitudes of absolute value less than 66^o when compared to TPXO8. We evaluate the tides based on 184-day simulations including eight tidal constituents: M_2, S_2, N_2, K_2, K_1, O_1, Q_1, P_1 on a global 45-to-5km variable resolution mesh. The model allows for wetting and drying in shallow regions. We exclude cells that are dry during simulations from the evaluation of final results. Table 5.1 shows the simulations performed for the study. The landfast ice includes seasonality, accounting for the difference between March and Spring extent in the northern and southern hemispheres. There are independent and combined simulations for 2015, 2060, and 2100. The independent cases use present-day March conditions for all control components.

5.3 Data Sources

5.3.1 Ice Shelf Cavities

We adopt 21^{st}-Century projections of Antarctic ice shelf cavities Ice Shelf Cavities (ISC) using estimates based on the Representative Concentration Pathways (RCP) and Shared Socioeconomic Pathways (SSP). These pathways represent potential future carbon dioxide scenarios and are commonly used as inputs into climate

Simulation Name	Ice-Shelves	Sea-Level	Landfast Ice
ctrl2015M	2015 CTRL	2015 CTRL	CTRL March
ctrl2015S	2015 CTRL	2015 CTRL	CTRL Sept.
isc2060ae05	2060 AE05	2015 CTRL	CTRL March
isc2060ae03	2060 AE03	2015 CTRL	CTRL March
isc2100ae05	2100 AE05	2015 CTRL	CTRL March
isc2100ae03	2100 AE03	2015 CTRL	CTRL March
lfi2100M	2015 CTRL	2015 CTRL	future March
lfi2100S	2015 CTRL	2015 CTRL	future Sept.
slc2060ae05	2060 CTRL	2015 AE05	CTRL March
slc2060ae03	2060 CTRL	2015 AE03	CTRL March
slc2100ae05	2100 CTRL	2015 AE05	CTRL March
slc2100ae03	2100 CTRL	2015 AE03	CTRL March
comb2060M	2060 AE03	2060 AE03	future March
comb2060S	2060 AE03	2060 AE03	future Sept.
comb2100M	2100 AE03	2100 AE03	future March
comb2100S	2100 AE03	2100 AE03	future Sept

Table 5.1: Array of simulations performed in this study. The cells indicate the year and type of the data used for each simulation. For the ice sheets and sea-level datasets, AE03 refers to the more extreme case, and AE05 refers to the more moderate case. CTRL indicates that it is the present-day “control” dataset. For the landfast ice, there are no robust future predictions at specific years, so we have only a “present” and “future” case, whereas the “future” case contains no landfast ice in the summer hemisphere.

models. We select both a moderate and an extreme cases of the RCP5-8.5 scenario (*Seroussi et al.*, 2020). The ice sheets were simulated in MALI (*Hoffman et al.*, 2018) following the experimental protocol outlined in *ISMIP* (2022). For the extreme case, we use exp03 (HadGEM2 RCP8.5), which has the most ice-sheet mass change, and for the moderate case, we use expAE05 (UKESM SSP5-8.5), which has the least mass change. We add the projected changes to the present-day ice-shelf cavities from BedMachine Version 2 (*Morlighem et al.*, 2020; *Morlighem*, 2020). For the purpose of ice-shelf cavities, we include only shelves in the Antarctic region due to their large area extent. Ice sheets in Greenland are important for melt and sea-level (discussed below), but do not have a significant cavity area as in the Antarctic region.

5.3.2 Sea-Level Projections

Sea-level projections consist of a steric and dynamic component and fingerprints associated with mass fluxes from future ice sheets and glacier projections. Steric sea-level changes Sea Level Change (SLC) are due to increasing water volume as temperatures rise. Dynamic sea-level changes occur due to the dynamic response of the ocean to atmospheric wind and buoyancy forces. The data for these (steric and dynamic) changes are calculated in *Jackson and Jevrejeva* (2016) from CMIP5 variables with appropriate corrections (e.g., inverted barometer, model drift). Changes in glacier mass from *Huss and Hock* (2015) are used to determine glacial SL fingerprints by solving the sea-level equation accounting for gravitational, rotational, and deformational effects (*Rietbroek et al.*, 2012). We compute SLC fingerprints for the Antarctic and Greenland ice sheets using the gravitationally self-consistent sea level theory and pseudo-spectral algorithm outlined in *Kendall et al.* (2005), adopting the code from *Han et al.* (2022), with truncation at spherical harmonic degree and order 512. We use a depth-varying elastically compressible visco-elastic Earth model in which the seismically inferred Preliminary Reference Earth Model (PREM)

(*Dziewonski and Anderson*, 1981) provides depth-varying elastic and density profiles through Earth's crust and mantle. We use the ice-sheet melt described in 5.3.1 for the Antarctic region. For Greenland, we use AWI_ISSM1 for experiment 5 from *Goelzer et al.* (2020) as a representative result for a high emissions scenario. The glacial fingerprints, ice sheet fingerprints, steric, and dynamic components of the SLC are incorporated into the model by subtracting them from the bathymetry.

5.3.3 Landfast Ice

Ocean ice, such as sea ice (free-floating ocean ice) and landfast ice (floating ice held fast against coastlines or ice sheets), can interact with the ocean through friction, pressure, and ice-ocean stress. However, for a single-layer barotropic model, a simple representation of sea ice is unrealistic. As shown in *Hibler et al.* (2006), a correct representation requires a dynamically embedded sea-ice layer with an ocean boundary layer. Because this is not possible in our barotropic model, we focus instead on only landfast ice, which can interact with the ocean through friction and pressure. Future simulations building upon this work but performed in a stratified ocean will be better able to incorporate sea ice.

Several studies indicate that the Arctic will be free of sea-ice by 2030-2050 (*Overland and Wang*, 2013; *Wang and Overland*, 2012; *Årthun et al.*, 2021; *Jahn et al.*, 2016). Here, we estimate future landfast ice using the most recent complete datasets of present-day extent and removing all landfast ice in the "summer" hemisphere (i.e., the northern hemisphere in September and the southern hemisphere in March). "Present" day Arctic landfast ice extent comes from *Konig Beatty* (2012) and Antarctic landfast ice extent comes from *Fraser and Massom* (2020). Landfast ice is incorporated into the model using the same equations as the ice shelf forcing, which includes the pressure term in eqn. 5.3 and a friction term between the fast ice and the ocean beneath it, using a friction coefficient of $\mathcal{C}_{lfi} = 5.36 \times 10^{-3}$.

5.4 Tidal Amplitude Changes

5.4.1 Changes in Tidal Constituent Amplitudes

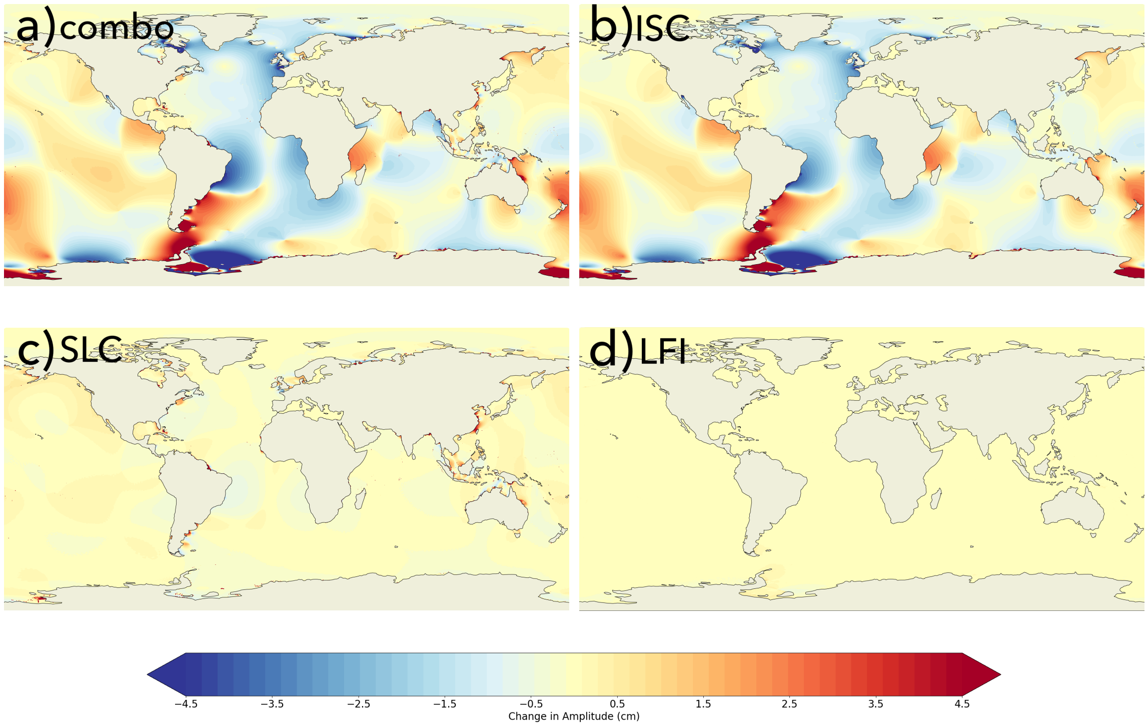

Figure 5.1: The plots show the change in M_2 amplitude (cm) at 2100 using AE03 ice sheet data due to a) combination of SLC, ISC changes, and LFI reduction; b) ISC changes only; c) SLC only; d) LFI reduction only. SLC impacts the coastal areas, but the ice-shelf cavity changes have much larger amplitude changes in the open-ocean.

Global tidal amplitude changes are generally in the range of several centimeters for both the ISC and SLC cases at 2100 for the AE03 (i.e., extreme) scenario. The LFI case, however, does not show much impact, even in the polar regions, with tidal changes in the range of 0.1 to 0.01 cm. These results contrast studies such as *Bij de Vaate et al.* (2021), which show the impact on tides from seasonal LFI changes when using a model that correctly accounts for the ice-water stress term by including an ice layer. For SLC, the largest impacts are on coastlines, particularly around China, the Patagonian Shelf, and the Amazon River.

In Fig. 5.1, we can see the influence of ISC on tidal changes in the range of sev-

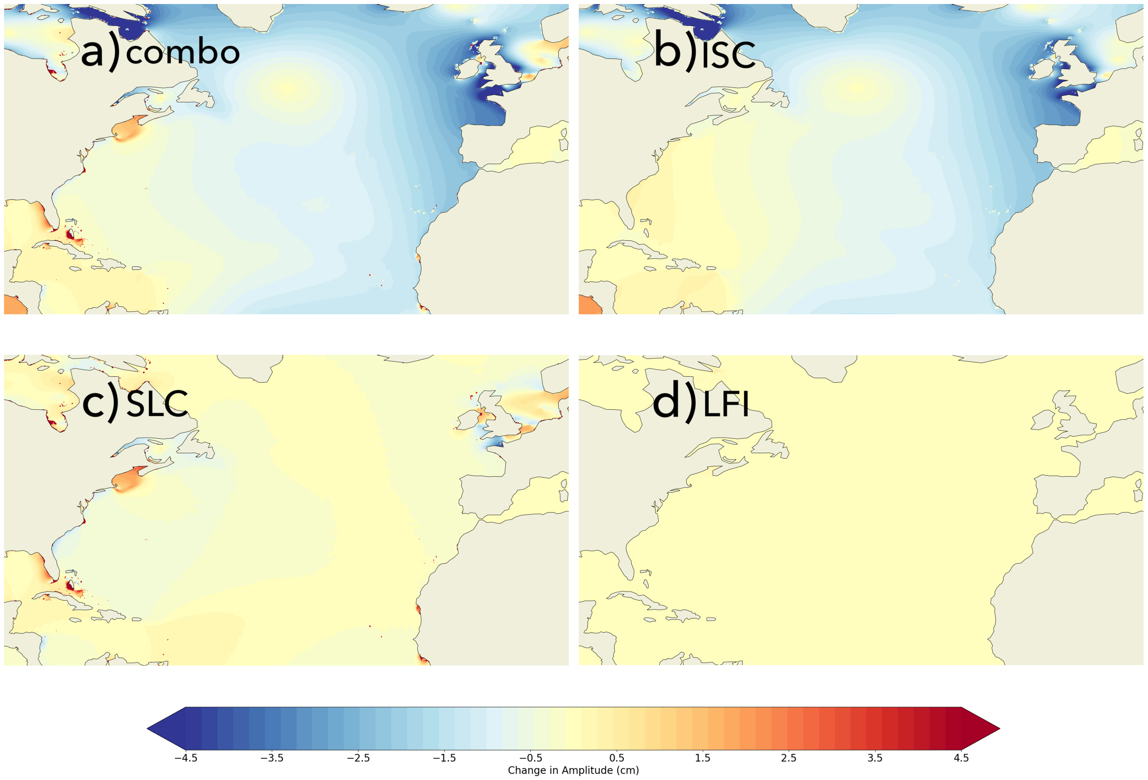

Figure 5.2: The plots show the change in M_2 amplitude (cm) in the North Atlantic region at 2100 using AE03 ice sheet data due to a) combination of SLC, ISC changes, and LFI reduction; b) ISC changes only; c) SLC only; d) LFI reduction only. The ISC changes generally lead to negative changes in amplitude in the open ocean, while SLC leads to some positive amplitude changes near the US east coast.

eral centimeters in the global oceans. The regional maps of the North Atlantic (5.2), Southeast Asia (5.3), and the South Atlantic (5.4) more clearly show the influence of relative influence of SLC and ISC near continental coastlines. In the North Atlantic, the tides in the open ocean have a general negative trend, and there are larger impacts, particularly near the English Channel and the Hudson Strait. On the eastern coast of Canada and the United States, there is more small-scale change dominated by sea level, such as increasing tides along Maine and Florida. Similarly, some near-shore influences from ISC change around Southeast Asia include increasing tidal amplitudes around north-east Australia and Papua New Guinea, while tides in the Bay of Bengal decrease. The tide changes due to SLC are especially large along the coast of China. The Patagonian Shelf is somewhat unique, showing much larger changes in the ISC

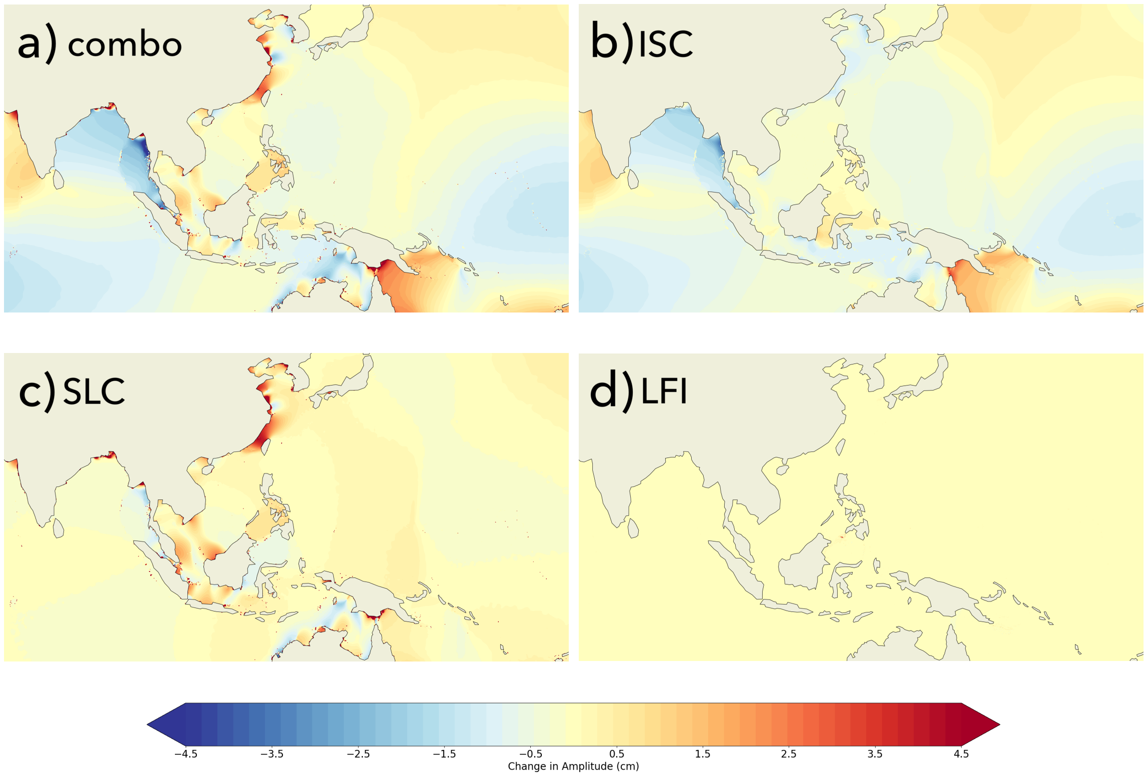

Figure 5.3: The plots show the change in M_2 amplitude (cm) around Southeast Asia at 2100 using AE03 ice sheet data due to a) the combination of SLC, ISC changes, and LFI reduction; b) ISC changes only; c) SLC only; d) LFI reduction only. There are some larger-scale near-shore impacts from ISC around the Bay of Bengal and Papua New Guinea, while SLC leads to smaller-scale changes, particularly the large increases in amplitude along the coast of China.

case, likely due to its proximity to Antarctica and the Filchner-Ronne ice sheets. These changes dominate the region, although SLC has some influence, particularly near the Amazon River, where tides increase in magnitude. In general, SLC has minimal impact on global tides, whereas ISC impacts are focused on the global ocean with some influence on near-shore tides. These results from the ISC imply the importance of resonant feedback between the cavities and the global ocean. Meanwhile, coastal tides are dominated by the local changes in geometry from changing sea level and shorelines.

The largest tidal amplitudes and changes in tidal amplitudes are in the M_2 constituent. Fig. 5.5 shows how the differences compare to all other constituents resolved

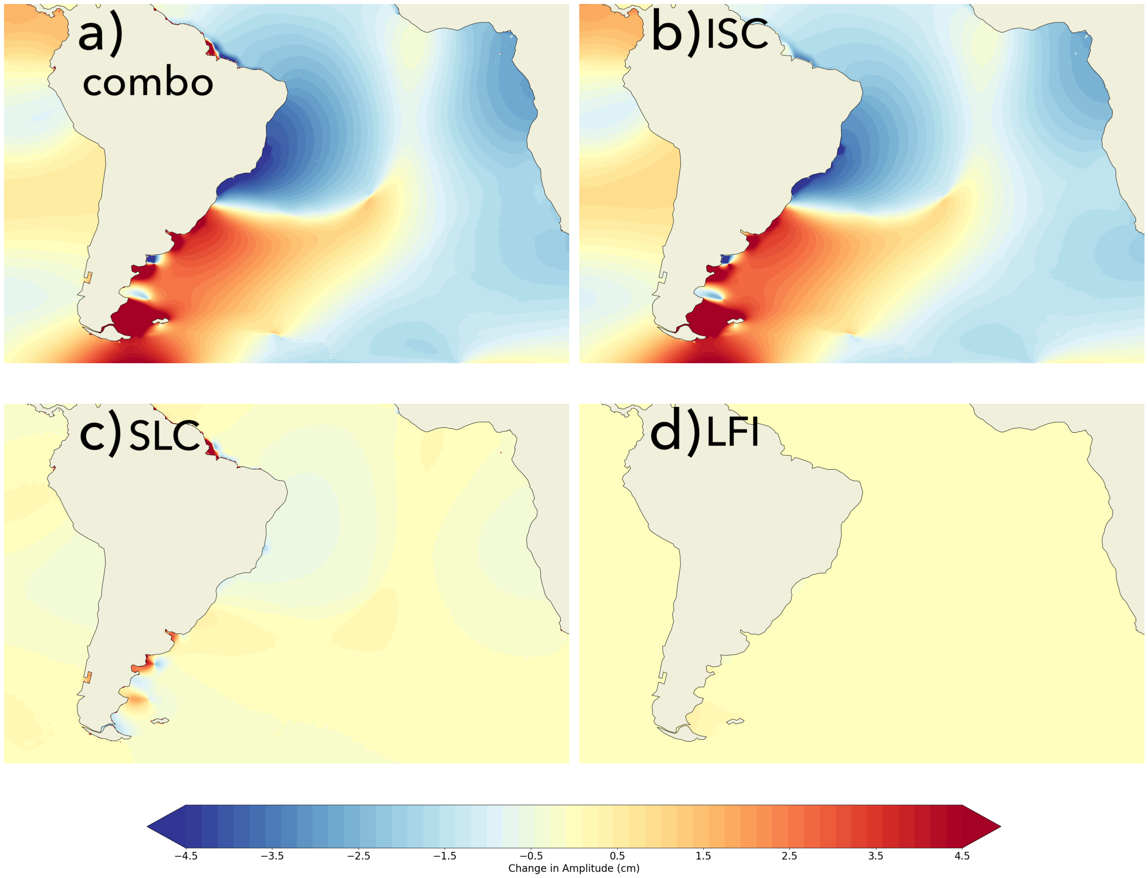

Figure 5.4: The plots show the change in M_2 amplitude (cm) around the South Atlantic at 2100 using AE03 ice sheet data due to a) the combination of SLC, ISC changes, and LFI reduction; b) ISC changes only; c) SLC only; d) LFI reduction only. Changes in the Antarctic ISC lead to large changes in amplitudes in this region, particularly around the Patagonian Shelf.

in the simulations. To contextualize these changes, we also show the total amplitudes for each constituent in Fig. 5.6 Outside the Antarctic region, the most considerable changes in global tides tend to occur in the semi-diurnal constituents, with the contribution from changes in S_2 being closest in magnitude to those from M_2. However, some significant impacts remain in the diurnal constituents K_1 and O_1 near shorelines in Southeast Asia.

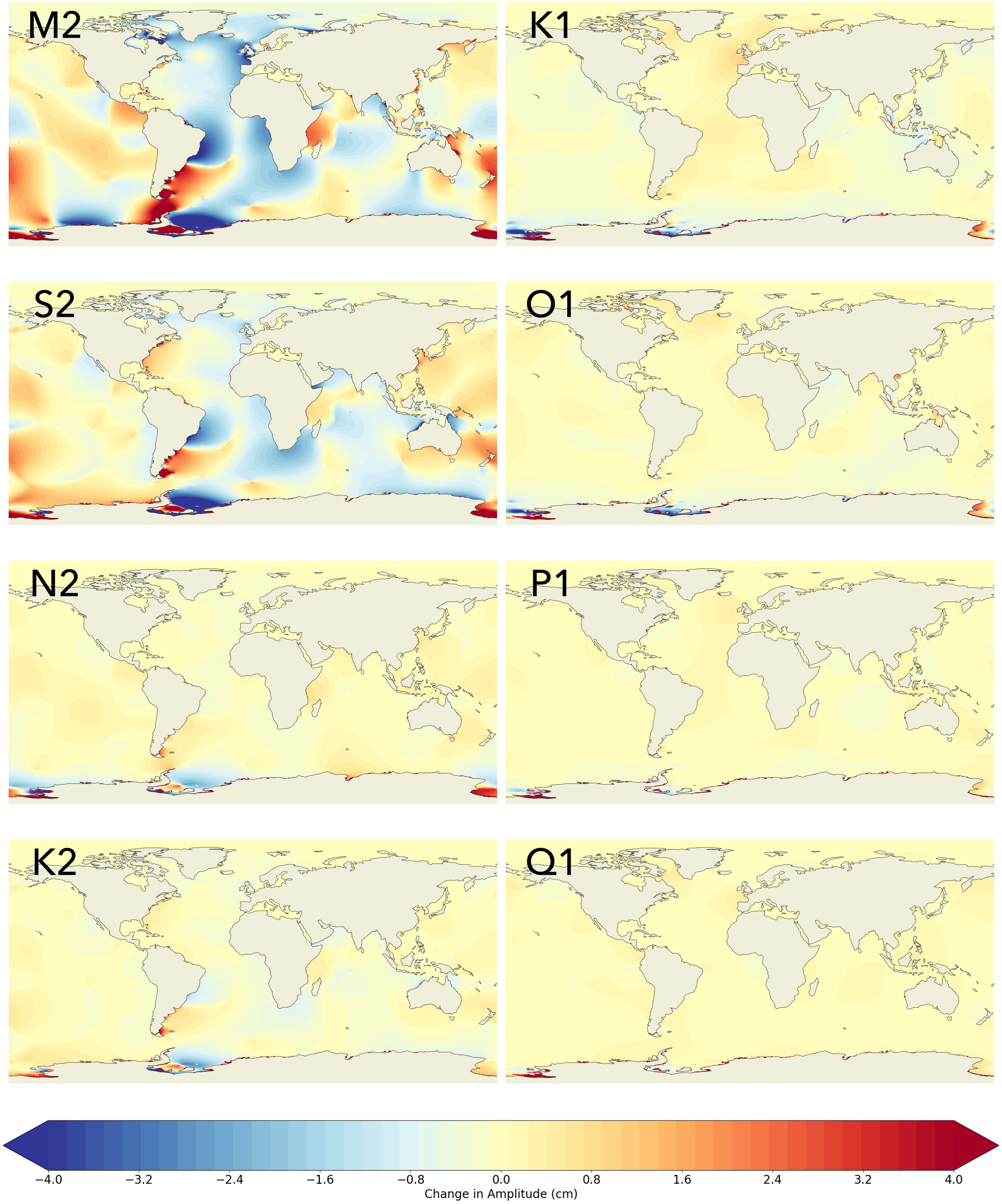

Figure 5.5: The plots show the global changes in all eight constituents included in the tidal runs for the com2100M simulation. The most significant changes outside the Antarctic region are in the M_2 and S_2 semidiurnal constituents.

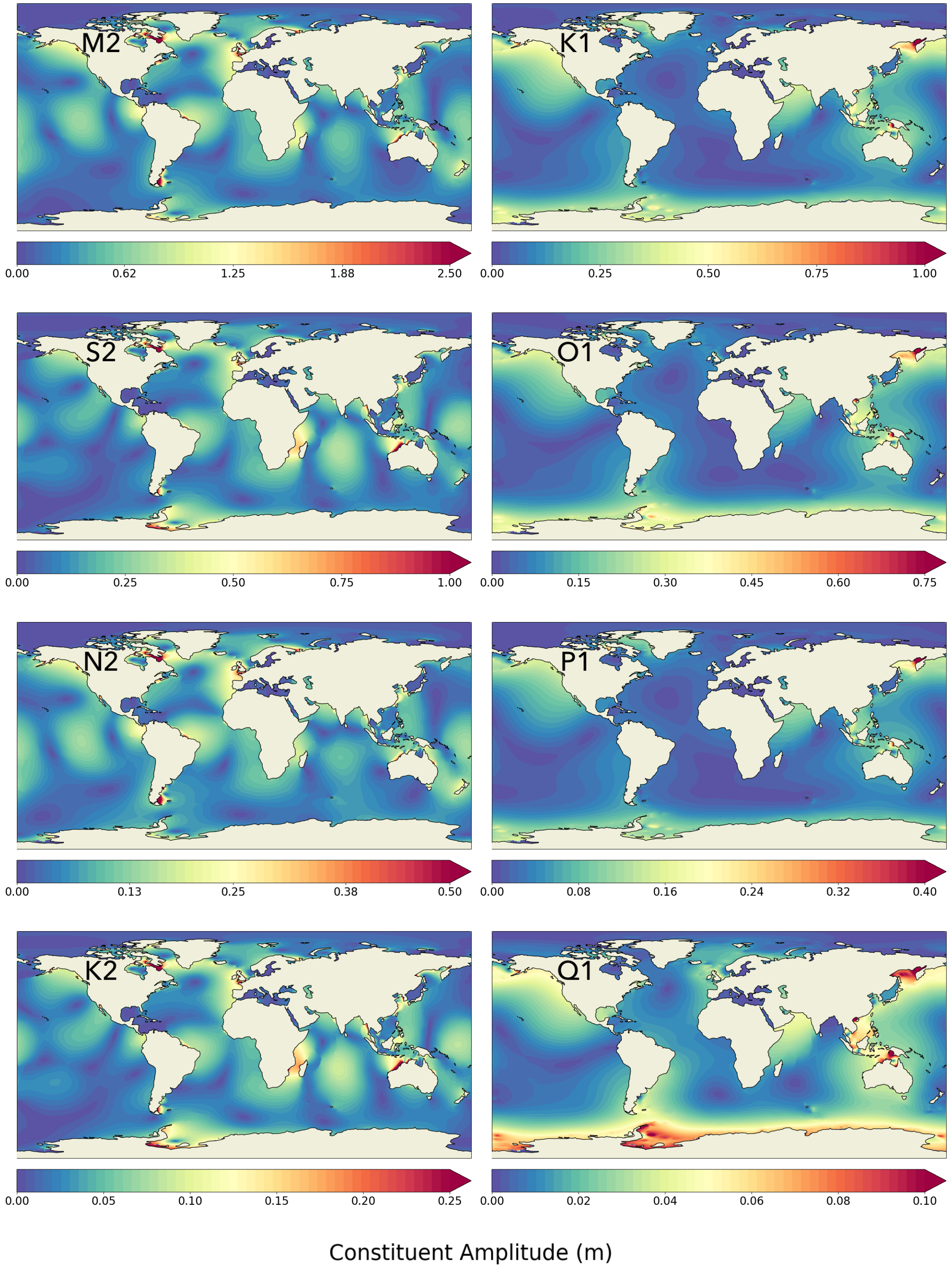

Figure 5.6: The plots show the total amplitudes for all eight constituents included in the tidal runs for the ctrl2015M simulation. Each plot has a unique scale based on the size of the constituent. M_2, S_2, and K_1 generally have the largest amplitudes while Q_1 has the smallest.

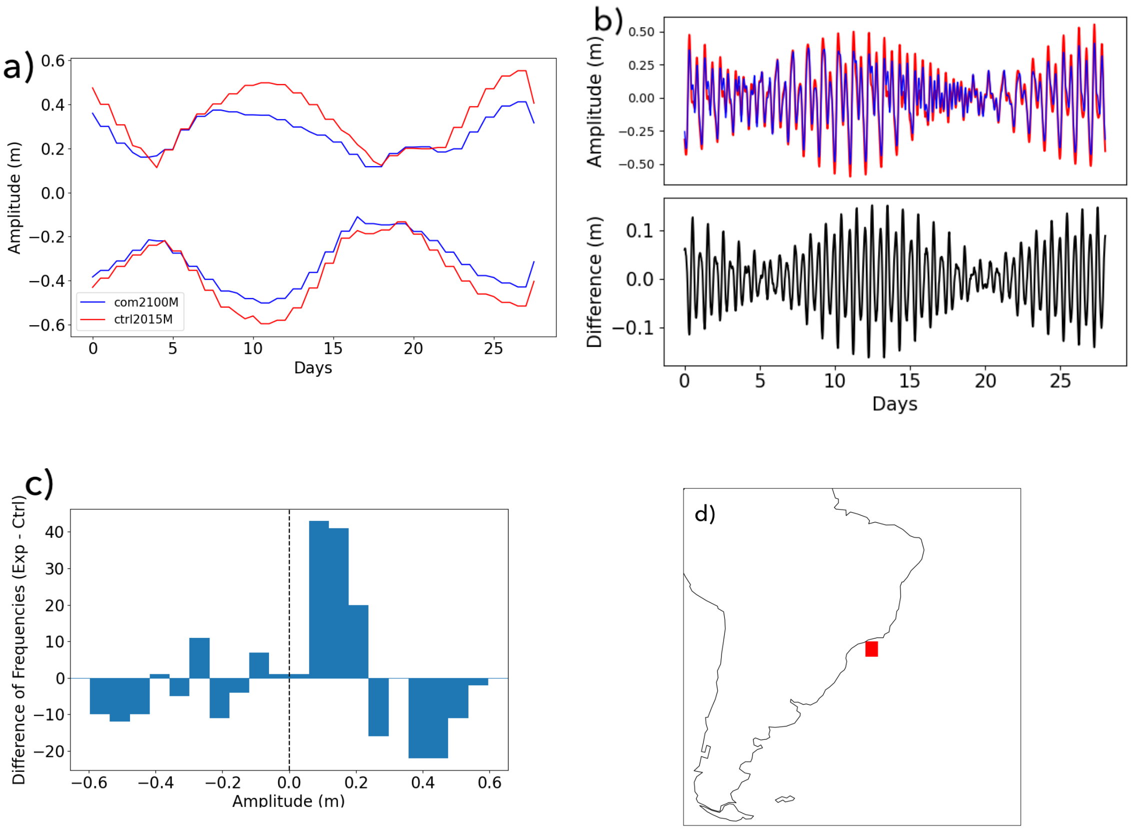

Figure 5.7: Total water level over 28 days for the com2100M run at a given virtual tide gauge location, showing a) 12-hour high-water marks, b) time series of water level at 30-minute intervals, c) histogram of amplitude frequencies over the 28-day period, and d) virtual tide gauge location.

5.4.2 Output at Virtual Tide Gauges

The previous sections detailed changes in individual tidal constituents, but the actual observed water levels are due to superpositions of all constituents. To see how the total water levels are impacted in the experimental future runs, we show time series plots of the model sea level output sampled at the location of several virtual tide gauges. Due to the limited resolution of the model (5 km at the coast), we chose locations that are not directly adjacent to the shoreline but are nearby regions of interest. The time series shows 30 minute intervals of total water level, along with 12-hour high water level spanning 28-days, allowing us to see changes in the spring-neap cycles as well. The histograms show the frequency of amplitude changes,

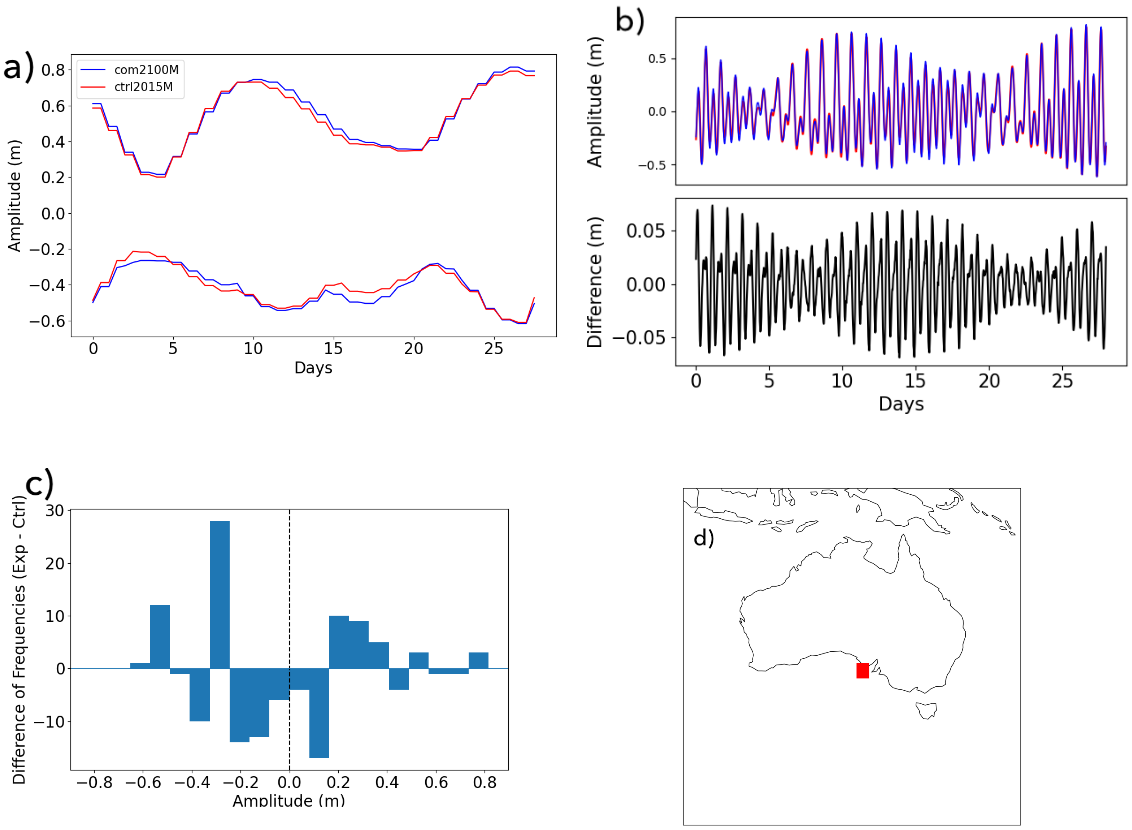

Figure 5.8: Total water level over 28 days for the com2100M run at a given virtual tide gauge location, showing a) 12-hour high-water marks, b) time series of water level at 30-minute intervals, c) histogram of amplitude frequencies over the 28-day period, and d) virtual tide gauge location.

indicating whether high- or low-amplitude tides are becoming more or less frequent, along with the general direction (increasing or decreasing) of the amplitude change.

In Fig. 5.7, the spring tide reaches a magnitude of around 0.5 m in the 2015 control run, while the 2100 case has lower tides closer to 0.3-0.4 cm, representing a difference of about 20-40%. From the change in amplitude histogram, we can see that most of the changes are in the positive range. In Fig. 5.8, the magnitude of the change is much smaller than in the previous gauge location, but there is a slight increase in the high water mark, with a decrease in the frequency of the lowest amplitude changes. Fig. 5.9 shows similar changes to the previous gauge. There are slight increases in the total range of water level, with the 2100 case increasing the max water level and

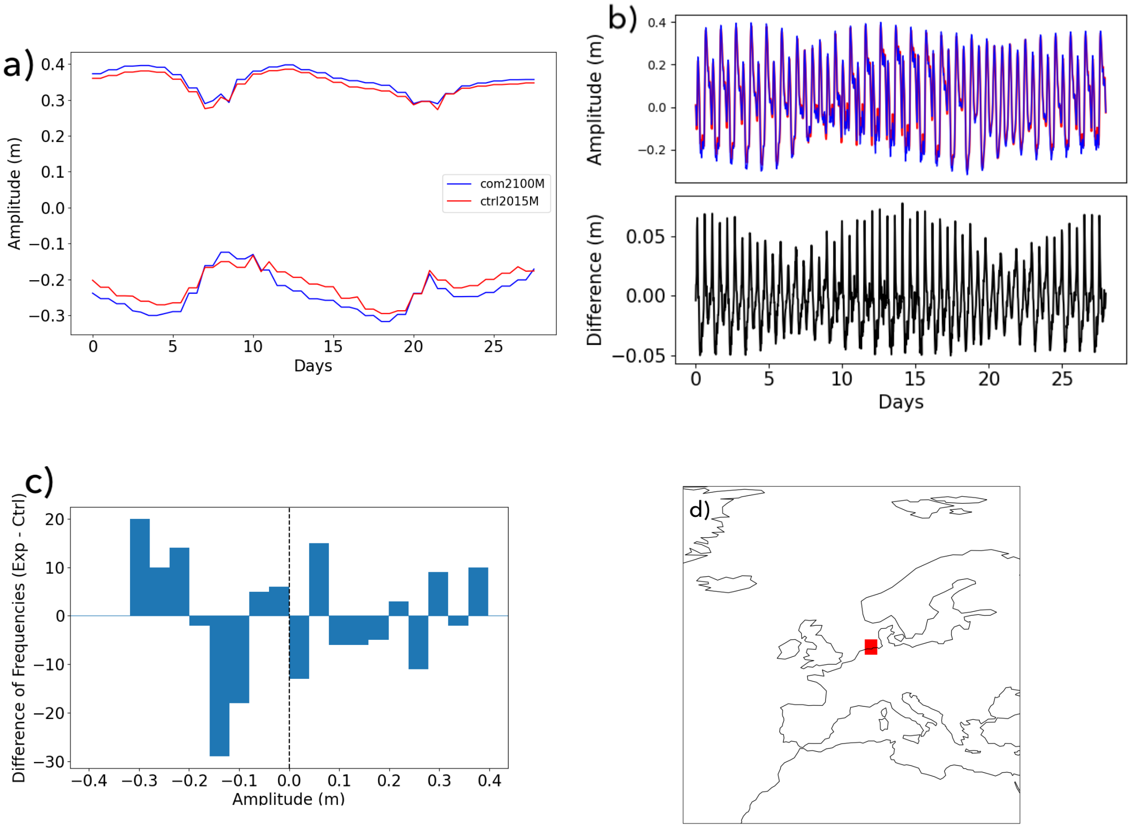

Figure 5.9: Total water level over 28 days for the com2100M run at a given virtual tide gauge location, showing a) 12-hour high-water marks, b) time series of water level at 30-minute intervals, c) histogram of amplitude frequencies over the 28-day period, and d) virtual tide gauge location.

decreasing the low water level as compared to the 2015 control case. Note that these demonstrate how tides could change in future scenarios. At any location in the real ocean, the local geometry, tidal prevention measures, and the amount of SLC and ice-sheet melt could have varying impacts, either increasing or decreasing the tidal ranges.

Table 5.2 shows the root-mean-square (RMS) difference, weighted by cell area, between the future simulation and the 2015 control simulation to quantify the amount between them.

$$RMS = \sqrt{\frac{\sum_i (Amp_i)^2 Area_i}{\sum_i Area_i}}, \tag{5.6}$$

where $Area_i$ is the area and Amp_i is the amplitude at the ith cell. We can see from

Constituent	RMS Difference (cm) Global	RMS Difference (cm) Latitude $> -70^o$
M2	1.41	0.65
S2	0.95	0.38
K1	0.32	0.18
N2	0.29	0.12
K2	0.27	0.11
O1	0.24	0.11
P1	0.12	0.07
Q1	0.10	0.07

Table 5.2: Root-mean-square differences calculated for each constituent based on the difference between the com2100M simulation and the ctrl2015M simulation. The last column limits the analysis to regions outside of the Antarctic, in order to compare global impacts of changes to the ice shelves.

the table that the M_2 and S_2 constituents have the largest impact both globally and north of -70^o latitude. However, the difference outside the Antarctic region is about half that of the global differences.

5.4.3 Changes along Coastlines

We show changes in amplitude (both magnitude and relative percentage) near coastlines and compare all of the simulations performed (Table 3.2). Fig. 5.10 follows the North Australian coast, demonstrating the regional difference in changing tides, with part having typically negative changes in tidal amplitudes and other sections having positive changes. We can also see the importance of the ice shelf cavities in determining tides, as depending on the scenario, tidal changes can have a large positive change (isc2100ae5) or a large negative change (2100ae03). In all cases, we can see that at 2100, where changes to sea level and ice sheets are more significant, the differences in tidal amplitude are greater. Fig. 5.11 shows similar results along the east coast of the United States.

Interestingly, the AE05 (moderate) case of ice cavity changes shows decreasing tidal amplitudes along the entire transect. Positive tidal amplitude changes are only

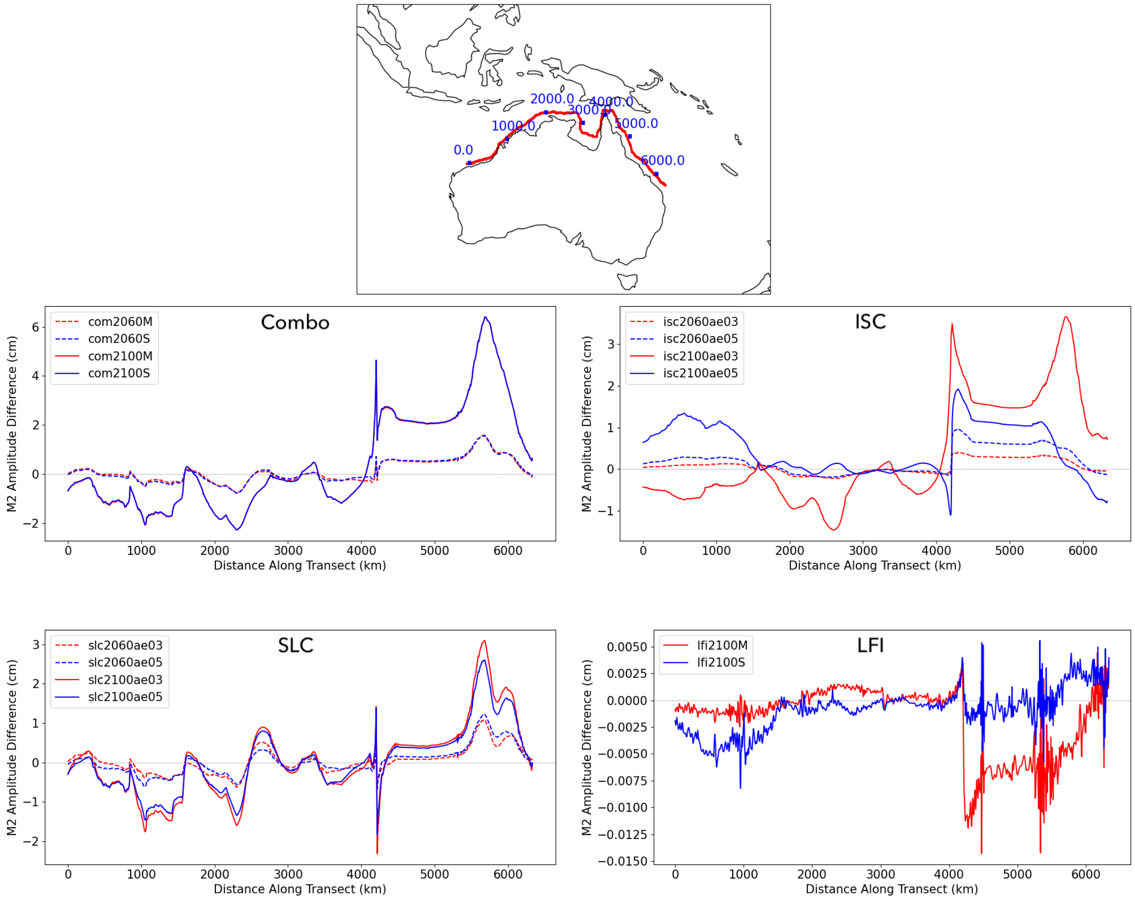

Figure 5.10: Changes in M_2 amplitude along northern Australia. For distances less than 4000 km along the transect, we can see that the direction of change in the amplitude of tides is very sensitive to the ISC geometry. The combined cases show the influence of both the SLC and ISC.

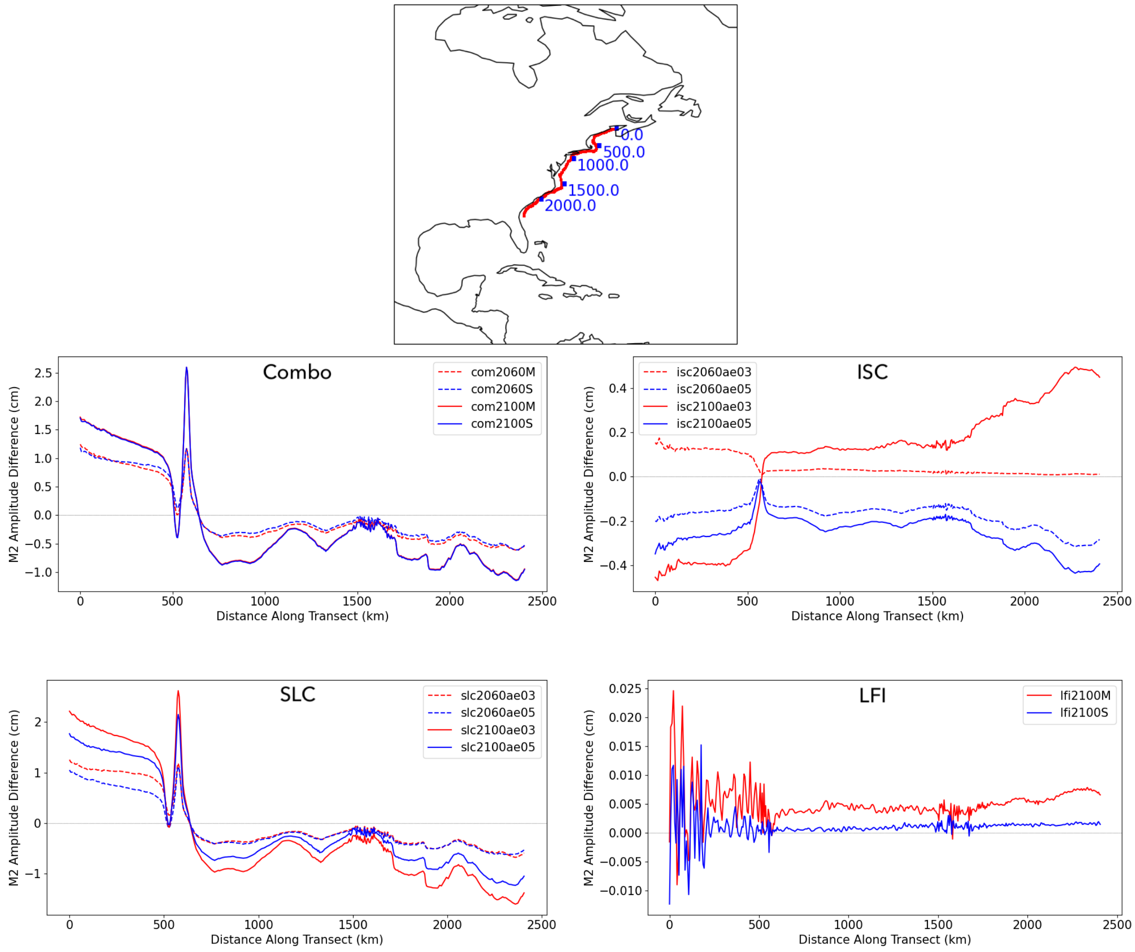

Figure 5.11: Changes in M_2 amplitude along the United States East Coast. The changes in amplitude alternate from positive to negative at around 500 km along the transect. The direction of change in amplitude from ISC can be either positive or negative depending on the case, but the influence from SLC is much larger and dominates in the combined case.

seen in the AE03 (extreme) case. Finally, along the coast of China in Fig. 5.12, we see a similar pattern, but the changes due to cavity geometry are generally always negative and of much smaller magnitude (about 1 cm) than the changes due to sea-level (up to 8 cm). In fact, only in the North Australia transect are the changes from SLC and ISC of about similar magnitude. In the US and China coast transects, the ISC contributes about 25% of the amplitude change. As a result, the combination case tends to follow most closely with the SLC case. These results make sense since

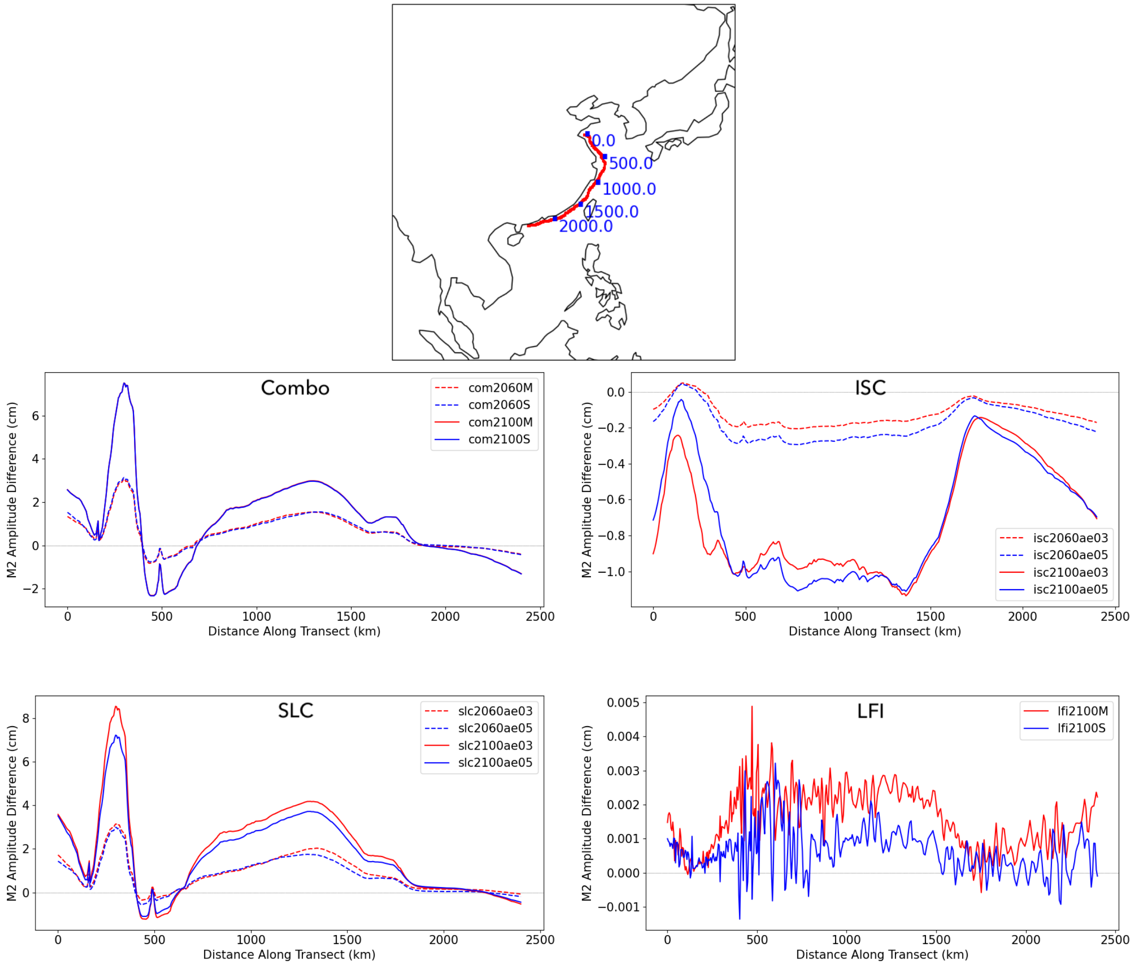

Figure 5.12: Changes in M_2 amplitude along the coast of China. Changes due to SLC are generally positive along the transect, and reach up to 8 cm at around 300 km. The ISC changes are negative, leading to a moderating effect on the combined case which generally follows the SLC, but with lower amplitude changes.

these transects follow near continental coastlines where amplitude changes tend to be dominated by SLC. However, as we can see from the North Australia transect, there is a regional variation to this influence. ISC can have as much influence as SLC, even when approaching coastlines.

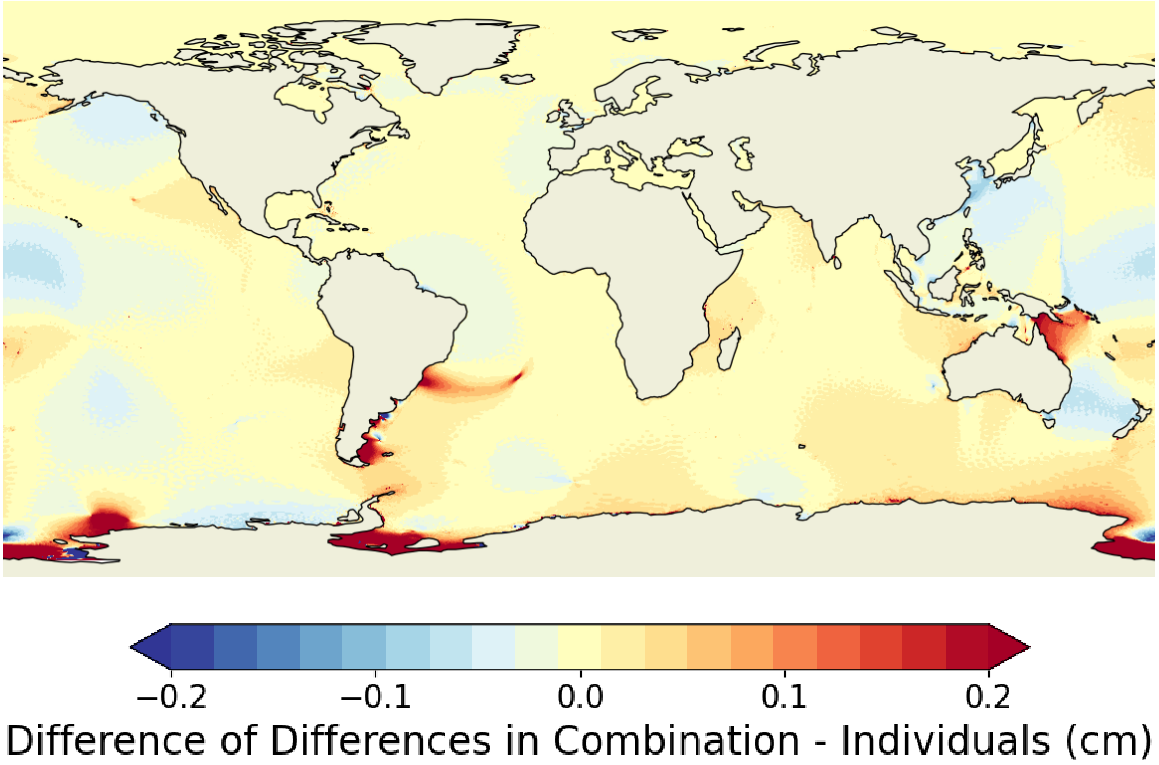

Figure 5.13: Differences between the com2100M run and the sum of the water level changes from the individual contributions.

5.5 Nonlinearity in the Impact on Tidal Change

To understand how nonlinearity impacts how different components affect tides, we first calculated the difference in amplitudes from the combination simulation. Then, we subtracted the difference in amplitudes from the sum of the individual simulations.

$$\Delta A_{nl} = (A_{combo} - A_{ctrl}) - \big((A_{SLC} - A_{ctrl}) + (A_{ISC} - A_{ctrl}) + (A_{LFI} - A_{ctrl})\big) \quad (5.7)$$

The difference in tidal amplitude due to nonlinearity (ΔA_{nl}) is evaluated from the amplitudes for the simulated cases. Figure 5.13 shows the global map of A_{nl} for the M_2 amplitude for March 2100 simulations.

We can see that the difference between the changes due to the individual simulations compared to the combination case is small, generally less than 1 cm globally.

Constituent	RMS Difference (cm) Global	RMS Difference (cm) Latitude $> -70^o$
M2	0.065	0.022
S2	0.040	0.019
K1	0.031	0.006
O1	0.027	0.006
N2	0.022	0.008
K2	0.016	0.007
P1	0.011	0.005
Q1	0.009	0.006

Table 5.3: Root-mean-square differences calculated for each constituent based on the difference between the combined simulation and the sum of the individual component simulations.

Some areas are clearly impacted, such as the Patagonian Shelf and north-east Australia. In the Australian region the magnitude of the nonlinearity reaches up to around 0.2 cm, while the overall changes in tidal amplitudes are around 1.5 to 3 cm (Fig. 5.10). This means the nonlinearity here is roughly 10% of the total change. Table 5.3 shows the RMS differences due to nonlinearity from all constituents included in the simulation. The constituents with the greatest amplitude changes also tend to have the greatest RMS difference for nonlinearity, with M_2 and S_2 at the top. The second table column only calculates the values for latitudes greater than -70^o to exclude the impacts directly under the ice shelf cavities. Doing this decreases the nonlinearity values further, with global RMS differences generally on the order of 10^{-2} to 10^{-3} cm. Outside of a few locations, the nonlinearity directly near coastlines seems to be fairly small. However, several coastal sea-level studies have found that these regions tend to have seen significant nonlinearity for tides and storm surges (*Thomas et al.*, 2019; *Rego and Li*, 2010; *Tang et al.*, 1996; *Marsooli and Lin*, 2018) and tides with sea-level rise (*Bilskie et al.*, 2016). These studies are generally regional with very high resolution (less than 1 km and down as low as 20 m in some cases). The finest resolution of our model is 5 km in this study, which is likely not fine enough to resolve the importance of nonlinearity in coastal regions.

5.6 Conclusions

It is clear that tides are changing and continue to change based on various climatic forcings. The IPCC reports an expected global mean rise in sea-level of 43 cm to 84 cm by 2100 as compared to 1986-2005 levels (*Oppenheimer et al.*, 2019b). Changes in tides near the coast of China reached as high as 8 cm, roughly 10-20% of the sea-level rise estimates. Compounding events of storm surge, sea-level rise, and high-tide could lead to even greater flood risks. Better prediction of regional variations in future tides can help inform policies to mitigate these risks. However, most studies looking at future tides, particularly regionally, account only for changes due to sea-level rise. In this study, we demonstrate that ice-shelf cavity geometry can also have significant impact on tides in both the global ocean and some near-shore regions. While this study looks at how ISC changes influence tides, it does not include interactions of tides on ice shelf cavities which are known to be significant (*Anandakrishnan et al.*, 2003; *Boeira Dias et al.*, 2023; *Fromm et al.*, 2023). Future predictions of both tides and ice-shelf cavities could be improved by allowing both to interact with the other. The calculation of landfast ice interactions could be resolved better by incorporating a sea-ice layer that allows for the ice-ocean stress to be calculated. In addition, follow-on studies could examine future tidal changes in full Earth System Models, which include baroclinic (stratified) ocean model components, rather than tides in the simplified barotropic tide models employed here. In addition, in regional studies, the changes from SLC and cryosphere changes could be calculated and then imposed at the boundaries to improve local tide modeling results.

CHAPTER VI

Conclusions

This work presents contributions to implementing tides within the Department of Energy's ocean model MPAS-Ocean and examines changes in simulated tides with various realistic climatic changes to sea-level rise and the cryosphere. The improved tides are important for predicting potential ocean sea-level changes, particularly regarding flood risks in coastal regions.

After a brief history and introduction to the basic ocean and tide modeling equations, Chapter III shows the initial results of tides within MPAS-Ocean and the improvement from incorporating an inline self-attraction and loading (SAL) calculation. This new calculation requires decomposing the sea-surface height into spherical harmonic components and is, therefore, more computationally costly than the alternative scalar approximation. We show that the improvements from an inline SAL method reduce the error by several centimeters. Using a variable resolution grid and less frequent updates of the SAL term can reduce computational cost without sacrificing tidal accuracy.

We continue in Chapter IV with further improvements to the tides through careful selection of the topographic wave drag implementation. We compare the results of three parameterization schemes – two scalar and one tensor – which are well-tested in other tide models. We find that the RMS tidal error can vary by over a centimeter depending on the scheme implemented, thus illustrating the importance of picking a suitable method for the tidal model. From this work, we further reduced tidal errors in MPAS-Ocean down to 3.4 cm, which is now comparable with other tidal models such as *Schindelegger et al.* (2018).

The model development of the previous two chapters paves the wave for Chapter V, in which we use the barotropic tide modeling capabilities of MPAS-Ocean to examine how tides interact with other components of the earth system. Specifically, this chapter discusses the significance of changes in the cryosphere and sea-level rise on tides based on SSP5-8.5 emission pathways out to the year 2100. While there are regional variations in the impacts, generally, the changes due to sea level are largest in near-shore regions, and the effects of ice-shelf geometry are largest in the open ocean. However, even in these near-shore regions, there are areas where the changes from ice-shelf cavities are comparable to or even larger than those from sea level. These results indicate the importance of accounting for ice-shelf cavity geometry in future tide studies.

The results thus far point to several directions for future work. One is to further examine the role of ice cavity geometry on tides through diagnosing which ice sheets are most responsible for the tidal changes observed in simulations. Further improvements to the mesh could also allow for higher resolution around coastlines, leading to better prediction of regional variation in changes. Another direction for model development is the inclusion of tides within the full baroclinic (multi-layer) version of MPAS-Ocean. A baroclinic treatment would have several benefits, particularly by allowing for a stress term between the ocean and ice layers, thus allowing better modeling of the impacts on tides from landfast ice and sea ice. Unfortunately, it is challenging to implement due to the cost of running a multi-layer model at the spatial resolution needed to also resolve tides in coastal regions. An alternate possibility is to use the current single-layer tide model alongside regional models with updated future tides evaluated separately and then applied to the boundaries of the model. These changes would allow for high-resolution studies of flooding in coastal regions that account for tidal changes due to both sea-level rise and cryosphere changes. The improvements to MPAS-Ocean described in this work help progress our understanding of how climate change might impact tides and coastal communities in the near future.

BIBLIOGRAPHY

Accad, Y., and C. L. Pekeris (1978), Solution of the tidal equations for the M2 and S2 tides in the world oceans from a knowledge of the tidal potential alone, *Philosophical Transactions of the Royal Society of London. Series A, Mathematical and Physical Sciences*, *290*(1368), 235–266.

Anandakrishnan, S., D. Voigt, R. Alley, and M. King (2003), Ice stream d flow speed is strongly modulated by the tide beneath the ross ice shelf, *Geophysical Research Letters*, *30*(7).

Arbic, B. K., and C. Garrett (2010), A coupled oscillator model of shelf and ocean tides, *Continental Shelf Research*, *30*(6), 564–574.

Arbic, B. K., S. T. Garner, R. W. Hallberg, and H. L. Simmons (2004), The accuracy of surface elevations in forward global barotropic and baroclinic tide models, *Deep Sea Research Part II: Topical Studies in Oceanography*, *51*(25-26), 3069–3101.

Arbic, B. K., J. X. Mitrovica, D. R. MacAyeal, and G. A. Milne (2008), On the factors behind large Labrador Sea tides during the last glacial cycle and the potential implications for Heinrich events, *Paleoceanography*, *23*(3).

Arbic, B. K., R. H. Karsten, and C. Garrett (2009), On tidal resonance in the global ocean and the back-effect of coastal tides upon open-ocean tides, *Atmosphere-Ocean*, *47*(4), 239–266.

Arbic, B. K., A. J. Wallcraft, and E. J. Metzger (2010), Concurrent simulation of the eddying general circulation and tides in a global ocean model, *Ocean Modelling*, *32*(3-4), 175–187.

Arbic, B. K., et al. (2018), A Primer on Global Internal Tide and Internal Gravity Wave Continuum Modeling in HYCOM and MITgcm, *New Frontiers in Operational Oceanography*, doi:10.17125/gov2018.ch13.

Arrhenius, S. (1896), Xxxi. on the influence of carbonic acid in the air upon the temperature of the ground, *The London, Edinburgh, and Dublin Philosophical Magazine and Journal of Science*, *41*(251), 237–276.

Årthun, M., I. H. Onarheim, J. Dörr, and T. Eldevik (2021), The seasonal and regional transition to an ice-free arctic, *Geophysical Research Letters*, *48*(1), e2020GL090,825.

Barton, K. N., et al. (2022), Global barotropic tide modeling using inline self-attraction and loading in mpas-ocean, *Journal of Advances in Modeling Earth Systems*, *14*(11), e2022MS003,207.

Beaman, R. (2010), Project 3D-GBR: A high-resolution depth model for the Great Barrier Reef and Coral Sea.

Beaman, R. (2016), High-resolution depth model for the Northern Australia – 100 m.

Bij de Vaate, I., A. Vasulkar, D. Slobbe, and M. Verlaan (2021), The influence of arctic landfast ice on seasonal modulation of the m2 tide, *Journal of Geophysical Research: Oceans*, *126*(5), e2020JC016,630.

Bilskie, M. V., S. Hagen, K. Alizad, S. Medeiros, D. L. Passeri, H. Needham, and A. Cox (2016), Dynamic simulation and numerical analysis of hurricane storm surge under sea level rise with geomorphologic changes along the northern gulf of mexico, *Earth's Future*, *4*(5), 177–193.

Bindoff, N. L., et al. (2019), Changing ocean, marine ecosystems, and dependent communities, *IPCC Special Report on the Ocean and Cryosphere in a Changing Climate*, pp. 477–587.

Bjerknes, V. (1904), Das problem der wettervorhersage, betrachtet vom standpunkte der mechanik und der physik, *Meteor. Z.*, *21*, 1–7.

Blakely, C. P., et al. (2022), Dissipation and Bathymetric Sensitivities in an Unstructured Mesh Global Tidal Model, *Journal of Geophysical Research: Oceans*, p. e2021JC018178.

Boeira Dias, F., S. R. Rintoul, O. Richter, B. K. Galton-Fenzi, J. D. Zika, V. Pellichero, and P. Uotila (2023), Sensitivity of simulated water mass transformation on the antarctic shelf to tides, topography and model resolution, *Frontiers in Marine Science*, *10*, 1027,704.

Brus, S. R., et al. (2023), Scalable self attraction and loading calculations for unstructured ocean tide models, *Ocean Modelling*, *182*, 102,160.

Bryan, K. (1969a), A numerical method for the study of the circulation of the world ocean, *Journal of Computational Physics*, *4*(3), 347–376.

Bryan, K. (1969b), A numerical method for the study of the circulation of the world ocean, *Journal of computational physics*, *4*(3), 347–376.

Buijsman, M. C., B. K. Arbic, J. Green, R. W. Helber, J. G. Richman, J. F. Shriver, P. Timko, and A. Wallcraft (2015), Optimizing internal wave drag in a forward barotropic model with semidiurnal tides, *Ocean Modelling*, *85*, 42–55.

Buijsman, M. C., J. K. Ansong, B. K. Arbic, J. G. Richman, J. F. Shriver, P. G. Timko, A. J. Wallcraft, C. B. Whalen, and Z. Zhao (2016), Impact of parameterized internal wave drag on the semidiurnal energy balance in a global ocean circulation model, *Journal of Physical Oceanography*, *46*(5), 1399–1419.

Buijsman, M. C., et al. (2020), On the interplay between horizontal resolution and wave drag and their effect on tidal baroclinic mode waves in realistic global ocean simulations, *Ocean Modelling*, *152*, 101,656.

Canadian Hydrographic Service (2018), Canadian Hydrographic Service Non-Navigational (NONNA) Bathymetric Data [Dataset].

Charney, J. G. (1948), On the scale of atmospheric motions, in *The Atmosphere—A Challenge: The Science of Jule Gregory Charney*, pp. 251–265, Springer.

Cinner, J. E., et al. (2022), Potential impacts of climate change on agriculture and fisheries production in 72 tropical coastal communities, *Nature communications*, *13*(1), 3530.

Codiga, D. L. (2011), Unified tidal analysis and prediction using the utide matlab functions, *Tech. rep.*, Graduate School of Oceanography, University of Rhode Island, Narragansett, RI.

Cummins, P. F., and L.-Y. Oey (1997), Simulation of barotropic and baroclinic tides off northern British Columbia, *Journal of Physical Oceanography*, *27*(5), 762–781.

De Dominicis, M., J. Wolf, S. Jevrejeva, P. Zheng, and Z. Hu (2020), Future interactions between sea level rise, tides, and storm surges in the world's largest urban area, *Geophysical Research Letters*, *47*(4), e2020GL087,002.

Dinniman, M. S., X. S. Asay-Davis, B. K. Galton-Fenzi, P. R. Holland, A. Jenkins, and R. Timmermann (2016), Modeling ice shelf/ocean interaction in Antarctica: A review, *Oceanography*, *29*(4), 144–153.

Durran, D. R. (1993), Is the coriolis force really responsible for the inertial oscillation?, *Bulletin of the American Meteorological Society*, *74*(11), 2179–2184.

Dushaw, B. D., G. D. Egbert, P. F. Worcester, B. D. Cornuelle, B. M. Howe, and K. Metzger (1997), A TOPEX/POSEIDON global tidal model (TPXO.2) and barotropic tidal currents determined from long-range acoustic transmissions, *Progress in Oceanography*, *40*(1-4), 337–367.

Dziewonski, A. M., and D. L. Anderson (1981), Preliminary reference earth model, *Physics of the earth and planetary interiors*, *25*(4), 297–356.

Egbert, G. D., and S. Y. Erofeeva (2002), Efficient inverse modeling of barotropic ocean tides, *Journal of Atmospheric and Oceanic Technology*, *19*(2), 183–204.

Egbert, G. D., and R. D. Ray (2000), Significant dissipation of tidal energy in the deep ocean inferred from satellite altimeter data, *Nature*, *405*(6788), 775–778.

Egbert, G. D., and R. D. Ray (2003), Semi-diurnal and diurnal tidal dissipation from TOPEX/Poseidon altimetry, *Geophysical Research Letters*, *30*(17).

Egbert, G. D., R. D. Ray, and B. G. Bills (2004), Numerical modeling of the global semidiurnal tide in the present day and in the last glacial maximum, *Journal of Geophysical Research: Oceans*, *109*(C3).

Engwirda, D. (2017), JIGSAW-GEO (1.0): Locally orthogonal staggered unstructured grid generation for general circulation modelling on the sphere, *Geoscientific Model Development*, *10*(6), 2117–2140.

Flick, R. E., J. F. Murray, and L. C. Ewing (2003), Trends in United States tidal datum statistics and tide range, *Journal of Waterway, Port, Coastal, and Ocean Engineering*, *129*(4), 155–164.

Foote, E. (1856), Circumstances affecting the heat of the sun's rays, *Am. J. Sci. Arts*, *22*(66), 383–384.

Fourier, J. (1827), Mémoire sur les températures du globe terrestre et des espaces planétaires, *Mémoires de l'Académie Royale des Sciences de l'Institut de France*, *7*, 570–604.

Fraser, A., and R. Massom (2020), Circum-antarctic landfast sea ice extent, 2000-2018, ver. 2.2, doi:10.26179/5d267d1ceb60c.

Fromm, T., V. Schlindwein, V. Helm, and V. Fofonova (2023), Observing tidal effects on the dynamics of the ekström ice shelf with focus on quarterdiurnal and terdiurnal periods, *Journal of Glaciology*, pp. 1–11.

GEBCO Compilation Group (2021), GEBCO 2021 Grid, doi:10.5285/c6612cbe-50b3-0cff-e053-6c86abc09f8f.

Goelzer, H., et al. (2020), The future sea-level contribution of the greenland ice sheet: a multi-model ensemble study of ismip6, *The Cryosphere*, *14*(9), 3071–3096.

Golaz, J.-C., et al. (2019), The DOE E3SM coupled model version 1: Overview and evaluation at standard resolution, *Journal of Advances in Modeling Earth Systems*, *11*(7), 2089–2129.

Golledge, N. R., E. D. Keller, N. Gomez, K. A. Naughten, J. Bernales, L. D. Trusel, and T. L. Edwards (2019), Global environmental consequences of twenty-first-century ice-sheet melt, *Nature*, *566*(7742), 65–72.

Gordeev, R., B. Kagan, and E. Polyakov (1977), The effects of loading and self-attraction on global ocean tides: the model and the results of a numerical experiment, *Journal of Physical Oceanography*, *7*(2), 161–170.

Green, J. M., and J. Nycander (2013a), A comparison of tidal conversion parameterizations for tidal models, *Journal of Physical Oceanography*, *43*(1), 104–119.

Green, J. M., and J. Nycander (2013b), A comparison of tidal conversion parameterizations for tidal models, *Journal of Physical Oceanography*, *43*(1), 104–119.

Griffies, S. M., C. Böning, F. O. Bryan, E. P. Chassignet, R. Gerdes, H. Hasumi, A. Hirst, A.-M. Treguier, and D. Webb (2000), Developments in ocean climate modelling, *Ocean Modelling*, *2*(3-4), 123–192.

Guerreiro, S. B., R. J. Dawson, C. Kilsby, E. Lewis, and A. Ford (2018), Future heatwaves, droughts and floods in 571 european cities, *Environmental Research Letters*, *13*(3), 034,009.

Haigh, I. D., et al. (2020), The tides they are a-Changin': A comprehensive review of past and future nonastronomical changes in tides, their driving mechanisms, and future implications, *Reviews of Geophysics*, *58*(1), e2018RG000,636.

Hall, G. F., D. F. Hill, B. P. Horton, S. E. Engelhart, and W. Peltier (2013), A high-resolution study of tides in the delaware bay: Past conditions and future scenarios, *Geophysical Research Letters*, *40*(2), 338–342.

Han, H. K., N. Gomez, and J. X. W. Wan (2022), Capturing the interactions between ice sheets, sea level and the solid earth on a range of timescales: a new "time window" algorithm, *Geoscientific Model Development*, *15*(3), 1355–1373.

Hayden, A.-M., S.-B. Wilmes, N. Gomez, J. Green, L. Pan, H. Han, and N. Golledge (2020), Multi-century impacts of ice sheet retreat on sea level and ocean tides in hudson bay, *Journal of Geophysical Research: Oceans*, *125*(11), e2019JC015,104.

Hendershott, M. (1972), The effects of solid earth deformation on global ocean tides, *Geophysical Journal International*, *29*(4), 389–402.

Hibler, W., A. Roberts, P. Heil, A. Y. Proshutinsky, H. Simmons, and J. Lovick (2006), Modeling m2 tidal variability in arctic sea-ice drift and deformation, *Annals of Glaciology*, *44*, 418–428.

Hoffman, M. J., et al. (2018), Mpas-albany land ice (mali): a variable-resolution ice sheet model for earth system modeling using voronoi grids, *Geoscientific Model Development*, *11*(9), 3747–3780.

Holloway, G., and A. Proshutinsky (2007), Role of tides in Arctic ocean/ice climate, *Journal of Geophysical Research: Oceans*, *112*(C4).

Huss, M., and R. Hock (2015), A new model for global glacier change and sea-level rise, *Frontiers in Earth Science*, *3*, 54.

Idier, D., F. Paris, G. Le Cozannet, F. Boulahya, and F. Dumas (2017), Sea-level rise impacts on the tides of the european shelf, *Continental Shelf Research*, *137*, 56–71.

ISMIP (2022), Ismip6 projections 2300 antarctica, `https://theghub.org/groups/ismip6/wiki/ISMIP6-Projections2300-Antarctica`, accessed: 2023-09-19.

Jackson, L. P., and S. Jevrejeva (2016), A probabilistic approach to 21st century regional sea-level projections using rcp and high-end scenarios, *Global and Planetary Change*, *146*, 179–189.

Jahfer, S., P. Vinayachandran, and R. S. Nanjundiah (2017), Long-term impact of Amazon river runoff on northern hemispheric climate, *Scientific Reports*, *7*(1), 1–9.

Jahn, A., J. E. Kay, M. M. Holland, and D. M. Hall (2016), How predictable is the timing of a summer ice-free arctic?, *Geophysical Research Letters*, *43*(17), 9113–9120.

Jay, D. A. (2009), Evolution of tidal amplitudes in the eastern Pacific Ocean, *Geophysical Research Letters*, *36*(4).

Jayne, S. R., and L. C. St. Laurent (2001), Parameterizing tidal dissipation over rough topography, *Geophysical Research Letters*, *28*(5), 811–814.

Kang, S., M. Foreman, W. Crawford, and J. Cherniawsky (2000), Numerical modeling of internal tide generation along the Hawaiian Ridge, *Journal of Physical Oceanography*, *30*(5), 1083–1098.

Kendall, R. A., J. X. Mitrovica, and G. A. Milne (2005), On post-glacial sea level–ii. numerical formulation and comparative results on spherically symmetric models, *Geophysical Journal International*, *161*(3), 679–706.

Konig Beatty, C. S. (2012), Arctic landfast sea ice 1953-1998, version 1, doi:10.7265/N5ZW1HV4.

Kuang, C., H. Liang, X. Mao, B. Karney, J. Gu, H. Huang, W. Chen, and H. Song (2017), Influence of potential future sea-level rise on tides in the china sea, *Journal of Coastal Research*, *33*(1), 105–117.

Le Provost, C., M. Genco, F. H. Lyard, P. Vincent, and P. Canceil (1994), Spectroscopy of the world ocean tides from a finite element hydrodynamic model, *Journal of Geophysical Research: Oceans*, *99*(C12), 24,777–24,797.

Lee, H., et al. (2024), Climate change 2023 synthesis report summary for policymakers, *CLIMATE CHANGE 2023 Synthesis Report: Summary for Policymakers*.

Luneva, M. V., Y. Aksenov, J. D. Harle, and J. T. Holt (2015), The effects of tides on the water mass mixing and sea ice in the Arctic Ocean, *Journal of Geophysical Research: Oceans*, *120*(10), 6669–6699.

Luz Clara, M., C. G. Simionato, E. D'Onofrio, and D. Moreira (2015), Future sea level rise and changes on tides in the patagonian continental shelf, *Journal of Coastal Research*, *31*(3), 519–535.

Lyard, F. H., F. Lefevre, T. Letellier, and O. Francis (2006), Modelling the global ocean tides: modern insights from FES2004, *Ocean dynamics*, *56*(5), 394–415.

Lyard, F. H., D. J. Allain, M. Cancet, L. Carrère, and N. Picot (2021), FES2014 global ocean tide atlas: design and performance, *Ocean Science*, *17*(3), 615–649.

Manabe, S., and K. Bryan (1969), Climate calculations with a combined ocean-atmosphere model, *J. atmos. Sci*, *26*(4), 786–789.

Manabe, S., and R. T. Wetherald (1967), Thermal equilibrium of the atmosphere with a given distribution of relative humidity, *Journal of Atmospheric Sciences*, *24*(3), 241 – 259, doi:https://doi.org/10.1175/1520-0469(1967)024⟨0241:TEOTAW⟩2.0.CO;2.

Marsooli, R., and N. Lin (2018), Numerical modeling of historical storm tides and waves and their interactions along the us east and gulf coasts, *Journal of Geophysical Research: Oceans*, *123*(5), 3844–3874.

Masson-Delmotte, V., et al. (2021), Ipcc, 2021: Summary for policymakers. in: Climate change 2021: The physical science basis. contribution of working group i to the sixth assessment report of the intergovernmental panel on climate change.

Mawdsley, R. J., I. D. Haigh, and N. C. Wells (2015), Global secular changes in different tidal high water, low water and range levels, *Earth's Future*, *3*(2), 66–81.

Merrifield, M. A., P. E. Holloway, and T. S. Johnston (2001), The generation of internal tides at the Hawaiian Ridge, *Geophysical Research Letters*, *28*(4), 559–562.

Morlighem, M. (2020), MEaSUREs BedMachine Antarctica, Version 2 [Dataset].

Morlighem, M., et al. (2020), Deep glacial troughs and stabilizing ridges unveiled beneath the margins of the antarctic ice sheet, *Nature Geoscience*, *13*(2), 132–137.

Müller, M., B. K. Arbic, and J. Mitrovica (2011), Secular trends in ocean tides: Observations and model results, *Journal of Geophysical Research: Oceans*, *116*(C5).

Müller, M., J. Cherniawsky, M. Foreman, and J.-S. von Storch (2012), Global M2 internal tide and its seasonal variability from high resolution ocean circulation and tide modeling, *Geophysical Research Letters*, *39*(19).

Munk, W. H. (1966), Abyssal recipes, in *Deep Sea Research and Oceanographic Abstracts*, vol. 13, pp. 707–730, Elsevier.

Munk, W. H., and C. Wunsch (1998), Abyssal recipes II: Energetics of tidal and wind mixing, *Deep Sea Research Part I: Oceanographic Research Papers*, *45*(12), 1977–2010.

Murty, T. (1985), Modification of hydrographic characteristics, tides, and normial modes by ice cover, *Marine Geodesy*, *9*(4), 451–468.

Nebeker, F. (1995), *Calculating the weather: Meteorology in the 20th century*, Elsevier.

Nycander, J. (2005a), Generation of internal waves in the deep ocean by tides, *Journal of Geophysical Research: Oceans*, *110*(C10).

Nycander, J. (2005b), Generation of internal waves in the deep ocean by tides, *Journal of Geophysical Research: Oceans*, *110*(C10).

Oppenheimer, M., et al. (2019a), Sea level rise and implications for low lying islands, coasts and communities, *IPCC Special Report on the Ocean and Cryosphere in a Changing Climate*.

Oppenheimer, M., et al. (2019b), Sea level rise and implications for low lying islands, coasts and communities.

Ortiz, J. D., and R. Jackson (2022), Understanding eunice foote's 1856 experiments: heat absorption by atmospheric gases, *Notes and Records*, *76*(1), 67–84.

Orton, P., N. Georgas, A. Blumberg, and J. Pullen (2012), Detailed modeling of recent severe storm tides in estuaries of the New York City region, *Journal of Geophysical Research: Oceans*, *117*(C9).

Overland, J. E., and M. Wang (2013), When will the summer arctic be nearly sea ice free?, *Geophysical Research Letters*, *40*(10), 2097–2101.

Padman, L., M. R. Siegfried, and H. A. Fricker (2018), Ocean tide influences on the Antarctic and Greenland ice sheets, *Reviews of Geophysics*, *56*(1), 142–184.

Pal, N., K. N. Barton, M. R. Petersen, S. R. Brus, D. Engwirda, B. K. Arbic, A. F. Roberts, J. J. Westerink, and D. Wirasaet (2023), Barotropic tides in mpas-ocean (e3sm v2): impact of ice shelf cavities, *Geoscientific Model Development*, *16*(4), 1297–1314.

Parke, M. E., and M. C. Hendershott (1980), M2, S2, K1 models of the global ocean tide on an elastic earth, *Marine Geodesy*, *3*(1-4), 379–408.

Pekeris, C. L., and Y. Accad (1969), Solution of Laplace's equations for the M 2 tide in the world oceans, *Philosophical Transactions of the Royal Society of London. Series A, Mathematical and Physical Sciences*, *265*(1165), 413–436.

Pelling, H. E., J. M. Green, and S. L. Ward (2013), Modelling tides and sea-level rise: To flood or not to flood, *Ocean Modelling*, *63*, 21–29.

Petersen, M. R., et al. (2019), An evaluation of the ocean and sea ice climate of E3SM using MPAS and interannual CORE-II forcing, *Journal of Advances in Modeling Earth Systems*, *11*(5), 1438–1458.

Pickering, M. D., N. Wells, K. Horsburgh, and J. Green (2012), The impact of future sea-level rise on the european shelf tides, *Continental Shelf Research*, *35*, 1–15.

Pringle, W. J. (2019), Global Tide Gauge Database [Dataset].

Pringle, W. J., D. Wirasaet, A. Suhardjo, J. Meixner, J. J. Westerink, A. B. Kennedy, and S. Nong (2018a), Finite-element barotropic model for the Indian and Western Pacific Oceans: Tidal model-data comparisons and sensitivities, *Ocean Modelling*, *129*, 13–38.

Pringle, W. J., D. Wirasaet, A. Suhardjo, J. Meixner, J. J. Westerink, A. B. Kennedy, and S. Nong (2018b), Finite-element barotropic model for the indian and western pacific oceans: Tidal model-data comparisons and sensitivities, *Ocean Modelling*, *129*, 13–38.

Pringle, W. J., D. Wirasaet, and J. J. Westerink (2018c), Modifications to internal tide conversion parameterizations and implementation into barotropic ocean models.

Pringle, W. J., D. Wirasaet, K. J. Roberts, and J. J. Westerink (2021a), Global storm tide modeling with adcirc v55: unstructured mesh design and performance, *Geoscientific Model Development*, *14*(2), 1125–1145.

Pringle, W. J., D. Wirasaet, K. J. Roberts, and J. J. Westerink (2021b), Global storm tide modeling with adcirc v55: unstructured mesh design and performance, *Geoscientific Model Development*, *14*(2), 1125–1145.

Pugh, D., and P. Woodworth (2014), *Sea-level science: understanding tides, surges, tsunamis and mean sea-level changes*, Cambridge University Press.

Raftery, A. E., A. Zimmer, D. M. Frierson, R. Startz, and P. Liu (2017), Less than 2 c warming by 2100 unlikely, *Nature climate change*, *7*(9), 637–641.

Ray, R. D. (1993), Global ocean tide models on the eve of TOPEX/POSEIDON, *IEEE Transactions on Geoscience and Remote Sensing*, *31*(2), 355–364.

Ray, R. D. (1998), Ocean self-attraction and loading in numerical tidal models, *Marine Geodesy*, *21*(3), 181–192.

Ray, R. D. (2006), Secular changes of the M2 tide in the Gulf of Maine, *Continental Shelf Research*, *26*(3), 422–427.

Rego, J. L., and C. Li (2010), Nonlinear terms in storm surge predictions: Effect of tide and shelf geometry with case study from hurricane rita, *Journal of Geophysical Research: Oceans*, *115*(C6).

Richardson, L. F. (1922), *Weather prediction by numerical process*, University Press.

Rietbroek, R., S.-E. Brunnabend, J. Kusche, and J. Schröter (2012), Resolving sea level contributions by identifying fingerprints in time-variable gravity and altimetry, *Journal of Geodynamics*, *59*, 72–81.

Ringler, T., L. Ju, and M. Gunzburger (2008), A multiresolution method for climate system modeling: Application of spherical centroidal voronoi tessellations, *Ocean Dynamics*, *58*, 475–498.

Ringler, T., M. Petersen, R. L. Higdon, D. Jacobsen, P. W. Jones, and M. Maltrud (2013), A multi-resolution approach to global ocean modeling, *Ocean Modelling*, *69*, 211–232.

Ringler, T. D., J. Thuburn, J. B. Klemp, and W. C. Skamarock (2010), A unified approach to energy conservation and potential vorticity dynamics for arbitrarily-structured c-grids, *Journal of Computational Physics*, *229*(9), 3065–3090.

Rocha, C. B., T. K. Chereskin, S. T. Gille, and D. Menemenlis (2016), Mesoscale to submesoscale wavenumber spectra in Drake Passage, *Journal of Physical Oceanography*, *46*(2), 601–620.

Ruault, V., J. Jouanno, F. Durand, J. Chanut, and R. Benshila (2020), Role of the tide on the structure of the Amazon plume: a numerical modeling approach, *Journal of Geophysical Research: Oceans*, *125*(2), e2019JC015,495.

Schaeffer, N. (2013), Efficient spherical harmonic transforms aimed at pseudospectral numerical simulations, *Geochemistry, Geophysics, Geosystems*, *14*(3), 751–758.

Schindelegger, M., J. Green, S.-B. Wilmes, and I. D. Haigh (2018), Can we model the effect of observed sea level rise on tides?, *Journal of Geophysical Research: Oceans*, *123*(7), 4593–4609.

Schwiderski, E. W. (1979), Global Ocean Tides. Part II. The Semidiurnal Principal Lunar Tide (M2), Atlas of Tidal Charts and Maps., *Tech. rep.*, Naval Surface Weapons Center, Dahlgren, VA.

Seroussi, H., et al. (2020), Ismip6 antarctica: a multi-model ensemble of the antarctic ice sheet evolution over the 21st century, *The Cryosphere*, *14*(9), 3033–3070.

Shihora, L., R. Sulzbach, H. Dobslaw, and M. Thomas (2022), Self-attraction and loading feedback on ocean dynamics in both shallow water equations and primitive equations, *Ocean Modelling*, *169*, 101,914.

Shum, C., et al. (1997), Accuracy assessment of recent ocean tide models, *Journal of Geophysical Research: Oceans*, *102*(C11), 25,173–25,194.

Simmons, H. L., R. W. Hallberg, and B. K. Arbic (2004), Internal wave generation in a global baroclinic tide model, *Deep Sea Research Part II: Topical Studies in Oceanography*, *51*(25-26), 3043–3068.

Smagorinsky, J., S. Manabe, and J. L. Holloway (1965), Numerical results from a nine-level general circulation model of the atmosphere, *Monthly weather review*, *93*(12), 727–768.

Spicer, P., K. Huguenard, L. Ross, and L. N. Rickard (2019), High-Frequency Tide-Surge-River Interaction in Estuaries: Causes and Implications for Coastal Flooding, *Journal of Geophysical Research: Oceans*, *124*(12), 9517–9530.

Stammer, D., et al. (2014), Accuracy assessment of global barotropic ocean tide models, *Reviews of Geophysics*, *52*(3), 243–282.

Stepanov, V. N., and C. W. Hughes (2004), Parameterization of ocean self-attraction and loading in numerical models of the ocean circulation, *Journal of Geophysical Research: Oceans*, *109*(C3).

Tang, Y. M., B. Sanderson, G. Holland, and R. Grimshaw (1996), A numerical study of storm surges and tides, with application to the north queensland coast, *Journal of Physical Oceanography*, *26*(12), 2700–2711.

Thomas, A., et al. (2019), Influence of storm timing and forward speed on tides and storm surge during hurricane matthew, *Ocean Modelling*, *137*, 1–19.

Thompson, P. R., M. J. Widlansky, B. D. Hamlington, M. A. Merrifield, J. J. Marra, G. T. Mitchum, and W. Sweet (2021), Rapid increases and extreme months in projections of united states high-tide flooding, *Nature Climate Change*, *11*(7), 584–590.

Tozer, B., D. T. Sandwell, W. H. F. Smith, C. Olson, J. R. Beale, and P. Wessel (2019), Global Bathymetry and Topography at 15 Arc Sec: SRTM15+, *Earth and Space Science*, *6*(10), 1847–1864, doi:https://doi.org/10.1029/2019EA000658.

Tyndall, J. (1861), Xxiii. on the absorption and radiation of heat by gases and vapours, and on the physical connexion of radiation, absorption, and conduction.—the bakerian lecture, *The London, Edinburgh, and Dublin Philosophical Magazine and Journal of Science*, *22*(146), 169–194.

Vallis, G. K. (2017), *Atmospheric and oceanic fluid dynamics*, Cambridge University Press.

Van der Walt, S., J. L. Schönberger, J. Nunez-Iglesias, F. Boulogne, J. D. Warner, N. Yager, E. Gouillart, and T. Yu (2014), Scikit-image: Image processing in Python, *PeerJ*, *2*, e453.

Vinogradova, N. T., R. M. Ponte, K. J. Quinn, M. E. Tamisiea, J.-M. Campin, and J. L. Davis (2015), Dynamic adjustment of the ocean circulation to self-attraction and loading effects, *Journal of Physical Oceanography*, *45*(3), 678–689.

Volkov, D. L., K. Zhang, W. E. Johns, J. K. Willis, W. Hobbs, M. Goes, H. Zhang, and D. Menemenlis (2023), Atlantic meridional overturning circulation increases flood risk along the united states southeast coast, *Nature Communications*, *14*(1), 5095.

Von Kármán, T. (1931), *Mechanical similitude and turbulence*, 611, National Advisory Committee for Aeronautics.

Wang, H., L. Xiang, L. Jia, L. Jiang, Z. Wang, B. Hu, and P. Gao (2012), Load Love numbers and Green's functions for elastic Earth models PREM, iasp91, ak135, and modified models with refined crustal structure from Crust 2.0, *Computers & Geosciences*, *49*, 190–199.

Wang, M., and J. E. Overland (2012), A sea ice free summer arctic within 30 years: An update from cmip5 models, *Geophysical Research Letters*, *39*(18).

Waterhouse, A. F., et al. (2014), Global patterns of diapycnal mixing from measurements of the turbulent dissipation rate, *Journal of Physical Oceanography*, *44*(7), 1854–1872.

Williams, M. J., A. Jenkins, and J. Determann (1985), Physical controls on ocean circulation beneath ice shelves revealed by numerical models, *Ocean, Ice, and Atmosphere: Interactions at the Antarctic Continental Margin*, *75*, 285–299.

Wilmes, S.-B., J. M. Green, N. Gomez, T. P. Rippeth, and H. Lau (2017), Global tidal impacts of large-scale ice sheet collapses, *Journal of Geophysical Research: Oceans*, *122*(11), 8354–8370.

Wilmes, S.-B., A. Schmittner, and J. Green (2019), Glacial ice sheet extent effects on modeled tidal mixing and the global overturning circulation, *Paleoceanography and Paleoclimatology*, *34*(8), 1437–1454.

Zaron, E. D., and G. D. Egbert (2006), Estimating open-ocean barotropic tidal dissipation: The hawaiian ridge, *Journal of Physical Oceanography*, *36*(6), 1019–1035.